Complex terrain: from ruggedness index (RIX), towards physical parameterization

Department of Wind Energy Master Report

Haakon Jahr Sletsjøe

DTU Wind Energy-M-0359

July 2020

DTU Wind Energy
Department of Wind Energy

Author: Haakon Jahr Sletsjøe

Title: Complex terrain: from ruggedness index (RIX), towards physical parameterization

DTU Wind Energy-M-035959
July 2020

Project period:
November 2019 – July 2020

ECTS: 45

Education: Master of Science

Supervisor:
Mark C. Kelly
DTU Wind Energy

Simon Watson
TU Delft

Remarks:
This report is submitted as partial fulfillment of the requirements for graduation in the above education at the Technical University of Denmark.

DTU Wind Energy is a department of the Technical University of Denmark with a unique integration of research, education, innovation and public/private sector consulting in the field of wind energy. Our activities develop new opportunities and technology for the global and Danish exploitation of wind energy. Research focuses on key technical-scientific fields, which are central

Summary

This thesis investigates terrain ruggedness characterization based on low-order terrain statistics. The statistics in question are the root-mean-square height and slope where the slopes are calculated both directly using the power spectral density and indirectly via a finite difference scheme. These statistics are, in contrast to the ruggedness index, shown to be close to independent of the input map resolution making them more suitable for future use due to the increasingly available high quality maps. Furthermore, these metrics can be bridged to the ruggedness index through strong correlations, thereby making implementation much more simple. The low-order statistics provide a strong, future-proof alternative to the current terrain ruggedness index and early investigations have in this report have shown promise in the development of sector-wise correlations. Such correlations could yield directional correction factors as opposed to the current omnidirectional ΔRIX correction factor.

Acknowledgements

First of all, I would like to thank my supervisor Mark Kelly for providing the initial idea for this project as well as giving me inspiration to make it my own. I also want to thank him for his guidance, knowledge, and patience without which I would have lost countless hours in understanding and applying the theory in this project. I would also like to thank my second supervisor Simon Watson for his support and guidance throughout this project. A big thank you also goes out to Neil Davis for his guidance in the use and conversion of maps.

Thank you to the European Wind Energy Master program for creating such a wonderful platform to meet and work together with some of the brightest new minds in wind energy and I am thankful for being invited to take part in this program.

I also want to thank all the classmates, colleagues, and friends I have met during my time in Denmark and the Netherlands. Thank you for making these past two years such an incredible experience.

Contents

List of Figures

List of Symbols

Abbreviations

ABL	Atmospheric Boundary Layer
AEP	Annual Energy Production
AGL	Above Ground Level
CFD	Computational Fluid Dynamics
DEM	Digital Elevation Map
DFT	Discrete Fourier Transform
FFT	Fast Fourier Transform
IBL	Internal Boundary Layer
IEC	International Electrotechnical Commission
LES	Large Eddy Simulation
NVE	Norwegian Water Resources and Energy Directorate
PCC	Pearson's Correlation Coefficient
PDF	Probability Density Function
PSD	Power Spectral Density
RANS	Reynolds Averaged Navier-Stokes
RIX	Ruggedness Index
RMS	Digital Surface Map
RMS	Root-Mean-Square
WAsP	Wind Atlas Analysis and Application Program
WECS	Wind Energy Conversion System

Greek symbols

α	Slope of regression line	$[-]$
χ	Potential	$[-]$
κ	von Kármán constant	$[-]$
μ	Stability parameter	$[-]$
ϕ	azimuth angle	$[^\circ]$
ψ	Stability function	$[-]$
σ	Standard deviation	$[-]$
θ_c	Critical slope	$[-]$

Latin symbols

ΔS	Fractional Speed-up	$[-]$
Δx	Resolution	$[-]$
A	Stability parameter	$[-]$
B	Stability parameter	$[-]$

C	Constant	$[-]$
c_p	Heat capacity	$[\mathrm{J/K}]$
D	Equilibrium distance	$[\mathrm{m}]$
E	Error	$[\%]$
f	Coriolis parameter	$[\mathrm{m/s}]$
G	Geostrophic wind	$[\mathrm{m/s}]$
g	gravitational acceleration	$[\mathrm{m/s^2}]$
H	Surface heat flux	$[\mathrm{W/m^2}]$
h	height, spectrum	$[\mathrm{m}, \mathrm{m^3}]$
J	Bessel function	$[-]$
k	Wavenumber	$[\mathrm{m^{-1}}]$
k	Wavevector	$[\mathrm{m^{-1}}]$
L	Obukhov length	$[\mathrm{m}]$
N	Number of radial lines	$[-]$
P	Porosity	$[-]$
p	Power law exponent	$[-]$
R	Radius, Pearson's Correlation Coefficient	$[-, \mathrm{m}]$
r	Radius	$[\mathrm{m}]$
R^2	Coefficient of determination	$[-]$
r_s	Spearman's ρ	$[-]$
S	Spectra	$[\mathrm{m^3}]$
T	Temperature	$[\mathrm{K}]$
U	Wind Speed	$[\mathrm{m/s}]$
u_*	Friction velocity	$[\mathrm{m/s}]$
W	Weighting model	$[-]$
w	Vertical velocity	$[\mathrm{m/s}]$
z	Elevation, Roughness length	$[\mathrm{m}]$
z_0	Roughness length	$[\mathrm{m}]$

CHAPTER 1
Introduction

Wind resource assessments of potential sites have with great success been using linearized flow models. These flow models are capable of making accurate predictions of the local wind climate assuming the site in question is within operational limits. However, as the onshore wind industry matures, new developments are at an increasing rate located in regions considered outside the operational envelope of these linearized models. In recognition of this the orographic performance indicator ruggedness index (RIX) was developed. A Reynolds averaged Navier-Stokes (RANS) model was also develop especially for site assessments in an attempt to yield more physically correct results when assessing very rugged terrain. However, due to the financial and computational costs associated with RANS there is motivation to further develop the characterization of rugged terrain and the resulting correction factors. Though successful, RIX lacks a strong physical foundation and in-house attempts to expand upon the method by creating a directional, or sector-wise, metric have proven unsuccessful. Instead an alternative terrain ruggedness metric is investigated using low-order statistics derived from the terrain. With this in mind the following research objective is formulated:

The research objective is to investigate a terrain complexity characterization based on low-order statistics by establishing a relation between them and RIX as well as investigate the potential for these statistics to be used as a directional terrain complexity metric.

To successfully fulfill the research objective, the project is divided into the following milestones. First, an extensive literature review is carried out to cover the topics and theory relevant to the atmospheric boundary layer and the importance of topographical effects as well as the existing method to account for rugged terrain. Then, in Chapter 2 the data used and the methodology are covered and briefly validated. Next, Chapter 3 covers the map resolution comparison, the RIX correlation investigation using low-order terrain statistics, and the investigation into a potential directional (sector-wise) correlation to the speed-up factor. Finally, Chapter 4 the project is concluded by summarizing the important findings and pointing out certain shortcomings as well as making recommendations for further research.

1.1 Atmospheric Boundary Layer

The interaction of bodies in a moving fluid results in a boundary layer on the surface of the body. This phenomenon has been extensively studied in the field of boundary layer meteorology, accumulating a wealth of knowledge on the topic. A large portion of this knowledge is focused on the atmospheric boundary layer (ABL). The ABL,

visualized in Figure 1.1, is the boundary layer directly above the planets surface and is characterized as a continually turbulent region bounded by a instantaneous top which works as the interface between the turbulent layer within and the non-turbulent layer above (Wyngaard, 2010). The depth of the layer extends roughly 100 meters on clear nights and can extend up to 2 kilometers on warm days. The ABL is further divided into an outer layer and a surface layer, the latter of which accounts for the bottom 10% of the ABL. In wind power meteorology, wind speeds below the cut-out speed of wind turbines are generally ignored such that the primary target of analysis are the scenarios where the ABL extends roughly one kilometer.

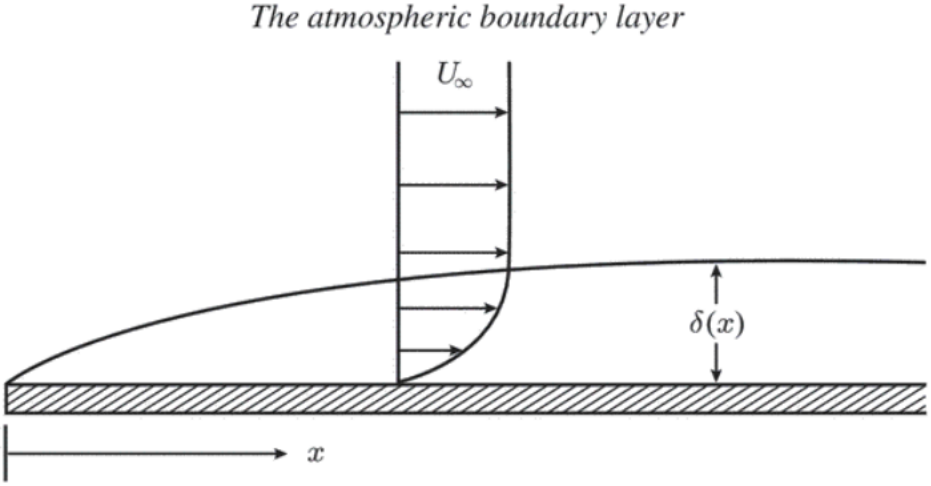

Figure 1.1: A laminar boundary layer on a flat plate in a uniform flow. The boundary layer thickness δ(x) is defined as the height at which the streamwise velocity reaches a specified fraction of the free-stream velocity U_∞ (Wyngaard, 2010).

From a regional perspective, the most important ABL properties to account for in the numerical models used in wind energy are those of land-surface interactions. These include roughness, moisture content, vegetation, and albedo (Garratt, 1994). The focus of this report will be the properties relating to the terrain variation.

Heterogeneity in the surface properties tend to give rise to large irregularities in the ABL structure. Such irregularities tend to form internal boundary layers which are normally confined to the lower portions of the boundary layer. In unorganized irregularities due to roughness or vegetation at length scales less than 10 km there is little to no organized mesoscale response in the ABL as shown in the type 'A' surface cover in Figure 1.2. Organized terrain irregularities at length scales above 10 km, defined as type 'B' surface cover, tend to yield an organized mesoscale response throughout the ABL.

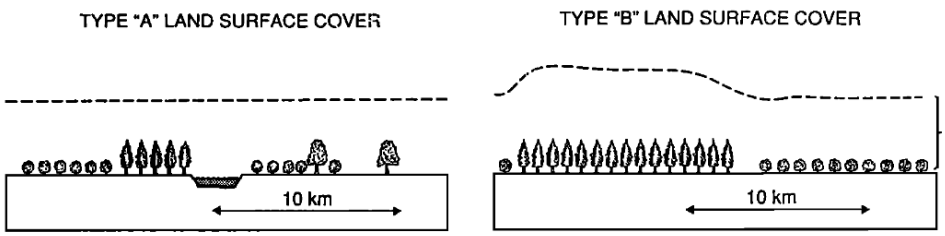

Figure 1.2: Classification of land surfaces (Shuttleworth, 1991). Type A contains disorganized terrain structures at length scales up to 10 km. Type B contains organized terrain structures at scales greater than 10 km.

Surface heterogeneity when considered on the smallest scales mainly affects the surface layer. However, it is within this layer that wind turbines reside and is therefore of great interest for wind resource modelling. In addition to heterogeneity caused by roughness and vegetation, elevation changes such as in hilly or mountainous terrain also produce significant heterogeneity. In such conditions the large changes induced in the pressure field produce a complex response in the boundary layer flow.

1.1.1 Wind Profile and Shear

The undisturbed wind field over flat terrain of low uniform roughness has been extensively studied both experimentally and theoretically and is extensively detailed in Garratt (1992) , Garratt (1994) and Wyngaard (2010) .

The measured wind profile as a function of height is commonly described by the power law approximation or the logarithmic wind profile with stability correction. The power law, given by Equation (1.1), uses the wind speeds $U(z_1)$ and $U(z_2)$ at heights z_1 and z_2 with a power law exponent p that is typically given as 0.14.

$$\frac{U\left(z_1\right)}{U\left(z_2\right)} = \left(\frac{z_1}{z_2}\right)^p \tag{1.1}$$

The exponent p however, does vary with height, roughness, and stability and as a result the viability of vertical extrapolation using the power law approximation is limited.

The logarithmic wind profile is considered a cornerstone of meteorology and for the range of heights of interest in wind power meteorology it is proven in literature by e.g. Tennekes (1973) to be a valid approximation. An improvement to the original equation uses a stability correction function ψ as shown in Equation (1.2)

$$U(z) = \frac{u_*}{\kappa}\left(\ln\frac{z}{z_0} - \psi\right) \tag{1.2}$$

where u_* is the friction velocity, κ is the von Kármán constant, and z_0 the roughness length. The stability function ψ provides a correction for the gradient of the wind profile that occurs in non-neutral conditions due to the increased vertical mixing. Several forms of the stability function have been proposed by e.g. Holtslag et al. (2014) for stable and unstable conditions. An approximation of the effects of stability on the wind profile

shown in Figure 1.3. Stable conditions tends towards a steeper slope whereas unstable conditions have a diminished slope. This occurs due to the increased turbulent mixing between layers in more unstable conditions.

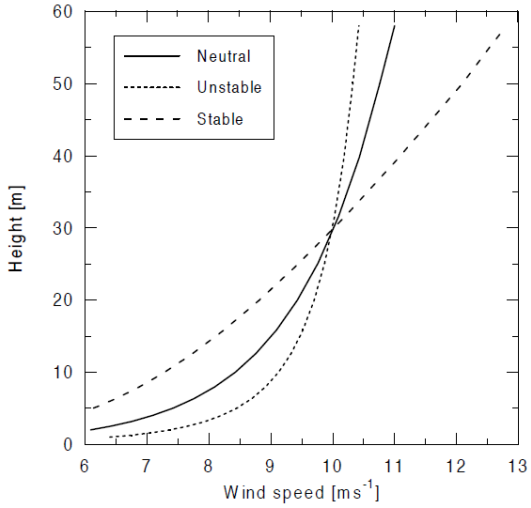

Figure 1.3: Wind profiles for neutral, unstable and stable conditions obtained from Equation (1.2). The mean gradient varies greatly depending on the stability conditions (Lundtang Petersen et al., 1997).

The wind in the ABL is driven by large-scale pressure differences. A method of representing this pressure-driven wind is using a representative wind speed, the geostrophic wind G. Assuming simplified conditions, such as an undisturbed flow over a vast flat terrain of uniform roughness, the geostrophic wind can be calculated from the pressure field. The geostrophic drag law can then be used to determine the wind speed near the surface:

$$G = \frac{u_*}{\kappa}\sqrt{\left[\ln\left(\frac{u_*}{f z_0}\right) - A\right]^2 + B^2} \tag{1.3}$$

where f is the Coriolis parameter, and A & B are nondimensional of stability parameters. They are A = 1.8 & B = 4.5 for neutral conditions. The logarithmic wind profile and the geostrophic drag law used in conjuction is known as the double vertical extrapolation method and is commonly used in the European Wind Atlas method which will be discussed later.

As previously stated, terrain heterogeneity such as elevation changes result in large scale pressure changes in the pressure field which in turn affect the boundary layer flow. For sloping terrain this leads to the acceleration of the flow in certain subsections of the boundary layer. The predicted wind profile given by the logarithmic wind profile will therefore have significant deviations from the real-world wind profile in more complex terrain.

1.1.2 Topography

The wind in the ABL is highly influenced by the surface characteristics, also known as the surface topography. The interplay between the topography and wind occurs over a range of length scales which, for modelling purposes are normally discretized (Lundtang Petersen et al., 1997). Wind power meteorology is primarily focused on the flow relevant to wind turbines and therefore the altitudes of interest are in the range of roughly 40 to 300 meters. Troen and Petersen (1989) approached the analysis of topography by first systematically defining the different aspects or characteristics of the topography into obstacles, terrain roughness, and orography.

An obstacle is defined as an object, such as a building or wind turbine, close enough such that the wind is strongly influenced by the presence of the obstacle by reducing the wind speed considerably. The obstacle height must be comparable and within a certain radius of the point-of-interest and is further described in the standards given by IEC 61400-12-1:2017.

The terrain roughness is the collective effect of the terrain surface and roughness elements, leading to an overall retardation of the wind near the ground. Obstacles can be considered roughness elements given they are too far and much lower in height to be considered as obstacles. Vegetation or houses are examples of roughness elements.

Orography relates to the geographical elements, such as mountains, whose scale is much greater than the point-of-interest. Such terrain features exert an orographic effect on the wind leading to flow acceleration near the summit or crests and deceleration at base or in valleys.

The division of topography into the three main categories above are able to describe any situation in relation to wind power meteorology and has been adopted into the IEC standards. This paper will mainly focus on roughness and orography and how they relate to the terrain 'complexity'.

1.1.2.1 Roughness

The surface roughness of a region is determined by the size and distribution of the roughness elements. It is normally equated to a single parameter, the roughness length z_0, defined as the height above the lower boundary of the logarithmic wind profile where the wind speed is zero. The roughness length is used by both the logarithmic wind profile and geostrophic drag law defined in Equations (1.2) and (1.3).

Vegetation, urban development, and soil all contribute to the roughness and as such the roughness length is not constant. Additionally, with densely organized distributions as shown in Figure 1.2 it may also useful to define a second roughness parameter d_0, which accounts for the height above the lower boundary of the profile above the land surface (Alfieri et al., 2019). This parameter can be especially useful when looking at vegetation or dense urban development. However, these parameters neglect the impact of numerous factors such as spacing, geometry, and frontal area. In sparse or open canopies the values of z_0 and d_0 are both influenced by the distribution and density of the vegetation (Raupach, 1992, 1994; Shaw & Pereira, 1982; Verhoef et al., 1997). Ignoring

their effects was shown by Zeng and Wang (2007) to produce errors up to 50% when estimating the roughness parameters. Maurer et al. (2015) determined that large errors in the roughness parameters result in significant errors when modelling momentum, heat, and moisture fluxes.

The effect of wind direction is also a considerable factor to account for when estimating the roughness parameters. A study by Alfieri et al. (2019) found that particularly z_0 may be strongly influenced by the directionality of the wind over vineyards. Vineyards are generally characterized by trellised vines of 1-2.5 m height separated in rows with roughly 3 m spacing. Due to this design it is possible that factors other than vine height have a large influence on the surface roughness. This is in agreement with previous research done by Hicks (1973) which suggests that increasing vine density increases surface roughness.

1.1.2.2 Orography

Orography refers to the study or description of topographical relief of mountains, but also includes features with significant height variations and is commonly referenced to sea level. Regional orography is readily used by flow models such as the IBZ-model in the Wind Atlas Analysis and Application Program (WAsP) where the orography is imported directly from vector maps.

In Lundtang Petersen et al. (1997) the orography is commonly classified as: flat, hilly, or mountainous, see Figure 1.4. Both flat and hilly terrain, where hilly is defined

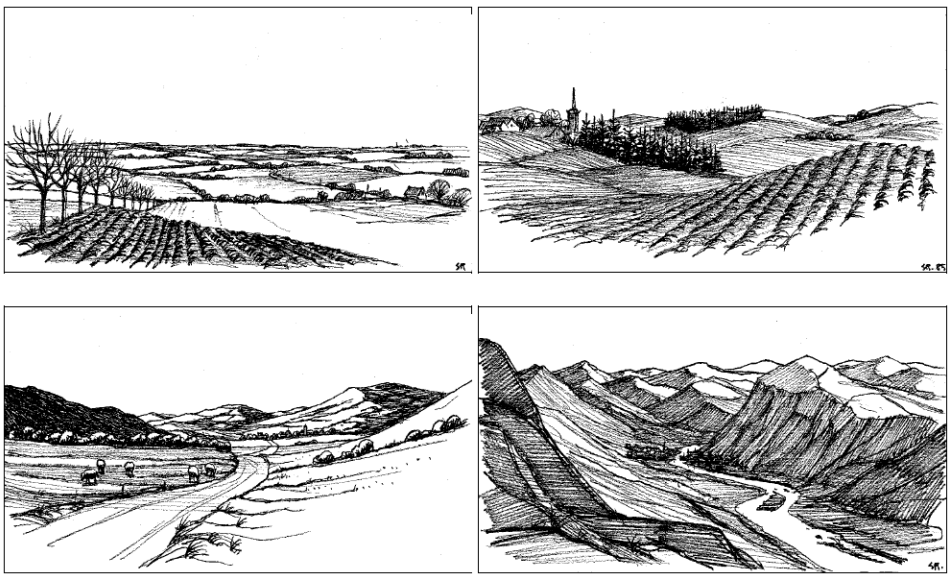

Figure 1.4: Landscape types: flat (upper left), hilly (upper right), complex (lower left), and mountainous (lower right) (Lundtang Petersen et al., 1997). *S. Rasmussen del.*

as having slopes less than 0.3 and horizontal dimensions to be a few kilometers, can be assumed to be mostly consisting of attached flow and therefore have negligible orographic effects. Both types of terrain lay within the operational envelope of linearized flow models

such as the IBZ-model (Bowen & Mortensen, 1996). Significant efforts by e.g. Walmsley et al. (1990) was put into validating the flow from the linearized models in flat and hilly terrain.

With increasing scale of the terrain features comes increasing horizontal dimensions as well as added terrain 'complexity'. The terrain is defined as mountainous when a significant fraction of the slopes near the point-of-interest exceed 0.3 resulting in flow separation. And as previously stated increased complexity due to elevation changes result in large scale pressure changes in the wind field which affect the entire boundary layer. In complex terrain conditions the double extrapolation of the vertical wind profile becomes inaccurate and in general linearized models do not model the flow adequately. For such situations numerical models should be utilized instead.

Regions where the terrain can be assumed to exert a significant orographic effect on the flow are often referred to as 'complex terrain'. Though there is no set standard for the parameterization of the terrain complexity there is a orographic performance metric that is frequently used known as the ruggedness index (RIX). It is defined as the fractional extent of the surrounding terrain that exceeds the critical slope (0.3) (Bowen & Mortensen, 1996; Bowen & Mortensen, 2004). RIX will be elaborated upon later in this report.

Previously it was discussed how due to the design of vineyards there would naturally be a large variation in the roughness parameters as a function of the wind direction. Areas of hilly terrain and in particularly mountainous terrain can also have a significant tendency towards being directional bias when looking at the terrain ruggedness. And for the purposes of wind energy, where there is often a prevailing wind direction it is natural that the terrain complexity along this direction should have a stronger weight in the estimations.

Terrain such as this can e.g. be found in the mountainous terrains of Norway. The fjords and valleys in Norway were geologically shaped by giant glacial tongues in areas with a gently sloping valley floor (Aarseth et al., 2014). The resulting orography left behind from these ancient glaciers are, in the scales relevant to wind energy, highly directional. Therefore, it is likely that the terrain ruggedness metrics would be similarly affected by the wind direction as found in the case of the vineyards.

An example of this type of terrain is shown in Figure 1.5 which shows an area in Aust-Agder and lies within one of the 13 areas pointed out by Norwegian Water Resources and Energy Directorate (NVE) as most suitable for wind energy development in the report by Jakobsen et al. (2019) . The region clearly shows how the valleys flowing a predominantly North-South direction.

Systematic investigations of the effects of roughness and orography have largely been confined to separate examinations. A recent attempt at consolidating the two was done by Liu et al. (2019) using large eddy simulations (LES) on the combined effect of roughness and orography on the flow around simplified hills, varying the roughness, slope, and shape of the hill.

For the mean streamwise flow it was found that the effect of the roughness on the flow grew weaker as the slope increased as well as if the hill became more 2-D.

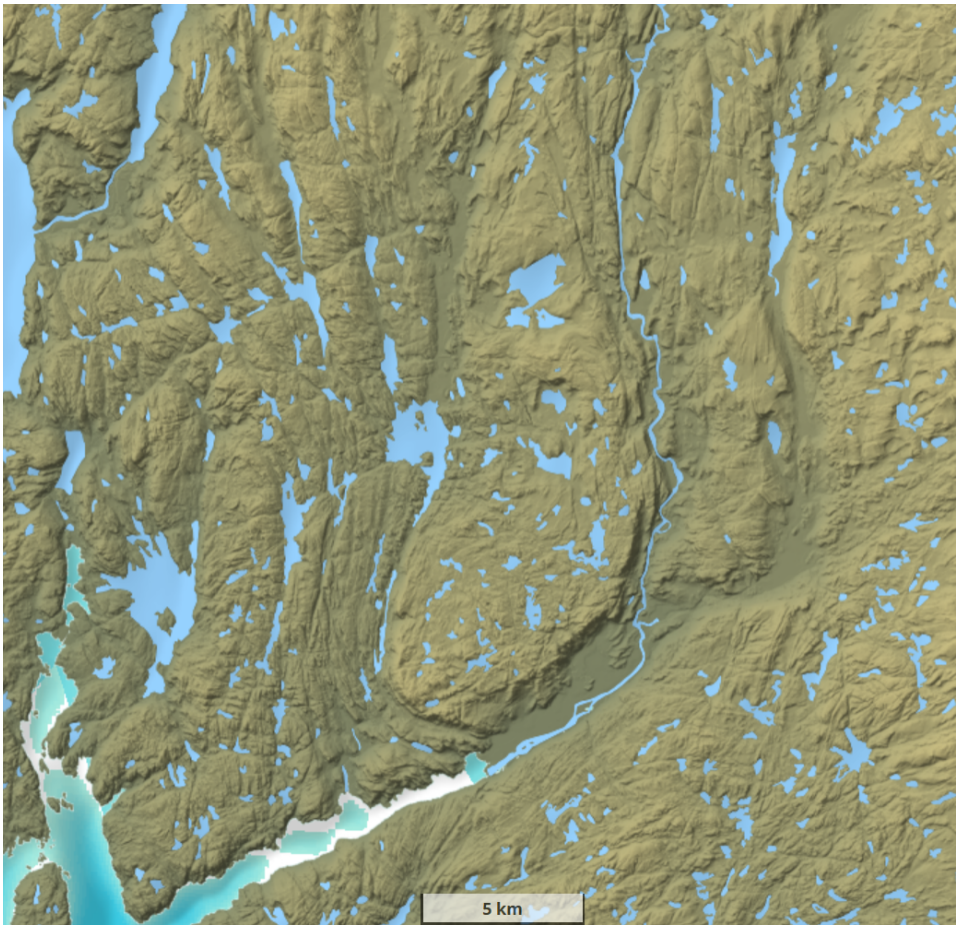

Figure 1.5: Terrain map of Vest-Agder, Norway centered at roughly 58°21'47.197"N, 6°52'44.084"E. Reprinted from ©Kartverket.

A common method of assessing the impact of the topography on the wind is through the (fractional) speed-up ΔS, given by

$$\Delta S = \frac{U\left(x, z'\right) - U_0\left(z'\right)}{U_0\left(z'\right)} \tag{1.4}$$

where $U(x, z')$ is the streamwise velocity at z' and $U_0(z')$ is the reference streamwise velocity at the same height ignoring the effects of the topography. Liu et al. (2019) performed simulations at reference heights of $z' = 10$ m and 50 m and an excerpt of the results are shown in Figure 1.6.

From the plots it is clear that ground roughness significantly increases the speed-up at z'= 10 m compared to over smooth hills. Though at 50 m altitude it appears the speed-up is largely unaffected by the roughness. However, ground roughness appears to increase the deceleration on the down slope side for all tested hill heights, which may be due to the increased drag and turbulent mixing. Considering the altitudes relevant for modern wind turbines it is clear that the effect of orography is the dominant factor and that local roughness is beyond a certain elevation negligible as pointed out in Troen

and Petersen (1989) . Though it must be noted that the local roughness used in Liu et al. (2019) is not representative of real-world effective roughness' and the resulting form drag.
At increasing hill heights the maximum speed-up also increases as previously found by Troen and Petersen (1989) . And while the hill shape appears to not impact the positive maxima, the negative area does increase. A positive speed-up at the hill crest can be viewed as beneficial for wind turbines due to more available momentum, and oppositely detrimental in the down slope region due to reduced available momentum.
Overall, the large effect of topography is indicative of the importance of accurate terrain characterization with regards to wind resource estimation, wind farm design, loads, and operational conditions.

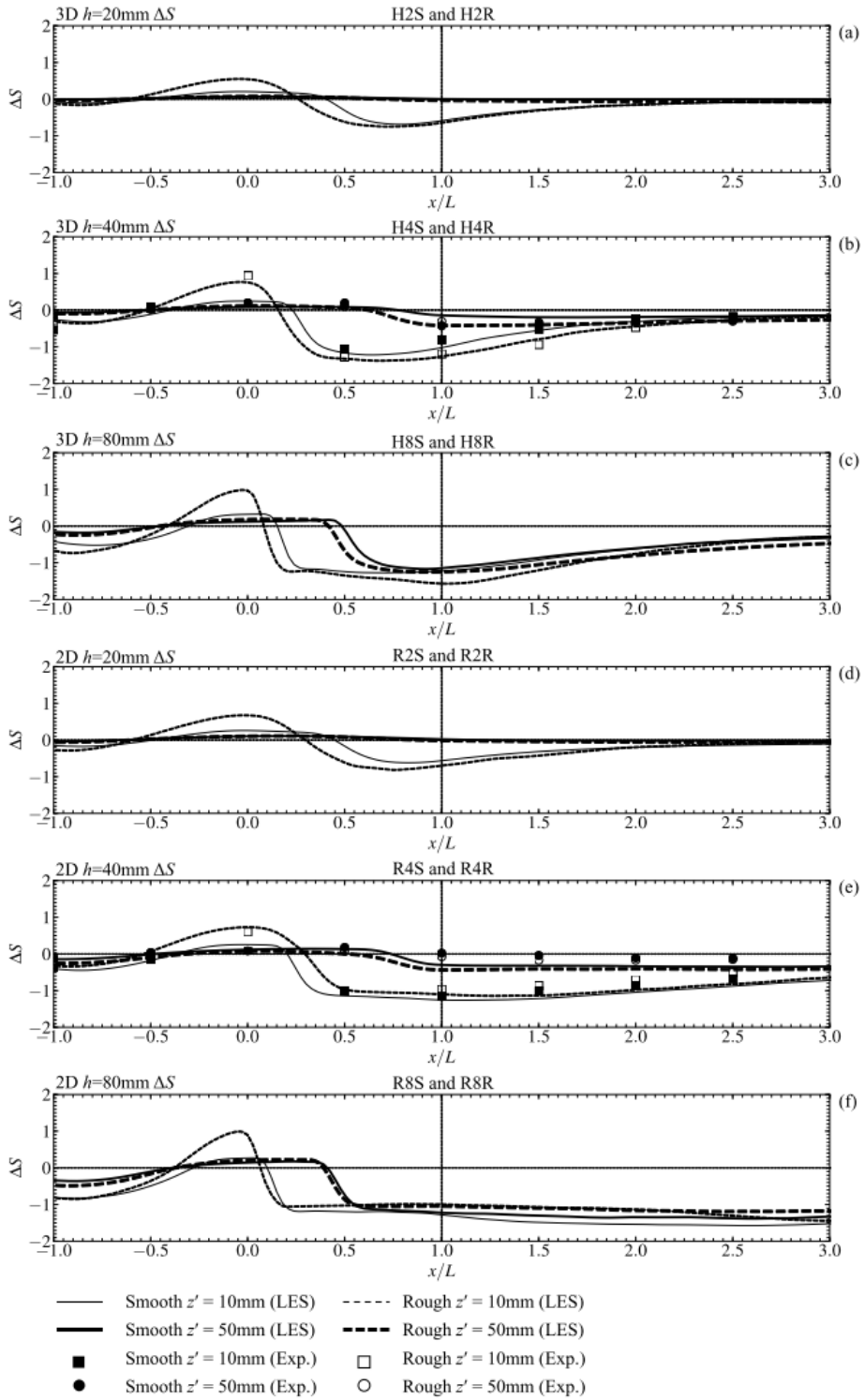

Figure 1.6: Fractional speed-up ΔS at z'= 10 mm and 50 mm, (a) 3D hills with h = 20 mm, (b) 3D hills with h = 40 mm, (c) 3D hills with h = 80 mm, (d) 2D hills with h = 20 mm, (e) 2D hills with h = 40 mm, and (f) 2D hills with h = 80 mm (Liu et al., 2019).

1.2 The WAsP Method

Wind for the purposes of wind power meteorology is a local phenomenon. And it is therefore highly influenced by the surrounding orography, roughness', and obstacles. Due to the large cost and significant time investment associated with wind measurements it has been necessary to develop models to interpolate between measurements as well as to be able to predict the wind climate at specific sites.

WAsP is an integrated computer micro-scale model used to predict local wind climates. The model utilizes the Wind Atlas concept which is built upon using set models to correct the wind measurement data by transforming their frequency distributions. WAsP is capable of making accurate predictions given that the reference and predictions sites are (Bowen & Mortensen, 2004):

a) subject to the same weather conditions

b) neutral stability conditions

c) local terrain is within operational envelope (ensure attached flows), and

d) high quality reference data.

Surface-layer Similarity Law

The altitudes of interest to modern wind energy range from 40 to 300 m and are within the atmospheric boundary layer. By ignoring the conditions with the lowest wind speed this layer can typically be assumed to extend up to a maximum of 1 km where the surface layer accounts for the lowest 10%, i.e. 100 m.

Section 1.1.1 discussed the use of the logarithmic wind profile, given by Equation (1.5), which is able to adequately describe the wind profile above a flat and homogeneous surface.

$$U(z) = \frac{u_*}{\kappa}\left(\ln\frac{z}{z_0}\right) \tag{1.5}$$

Deviations from this profile occur because the roughness is just one relevant parameter that influences the profile. The introduction of stability functions are discussed with Equation (1.2) and help correct the profile according to the stability. The form used by WAsP is given by: Equation (1.6):

$$u(z) = \frac{u_*}{\kappa}\left[\ln\frac{z}{z_0} - \psi(\frac{z}{L})\right] \tag{1.6}$$

where ψ is an empirical function and is described in Businger (1973) and Dyer (1974) . L is the Obukhov length and is defined as:

$$L = \frac{T_0}{\kappa g}\frac{c_p u_*^3}{H_0} \tag{1.7}$$

where T_0 is the surface temperature, H_0 is the surface heat flux, c_p is the heat capacity of air, and g is the acceleration due to gravity.

1.2.0.1 The Orographic Model

As mentioned the WAsP method uses several submodels to perform the corrections. However, only the orographic model will be detailed in this report. For a complete description the reader is directed to Troen and Petersen (1989) and Kelly and Troen (2016) .

The orographic model is a correction tool to account for orographic effects. The model is constructed to correct for 'hilly' terrain and is the reason terrain outside the normal operational envelope of WAsP can still be assessed. The model first calculates the potential flow perturbation due to the terrain corresponding to a unit wind vector in the undisturbed wind direction. This is given by:

$$\vec{u} = \nabla\chi, \tag{1.8}$$

where χ is the potential and $\vec{u}$ is the 3-D velocity perturbations.

Assuming a vanishing potential at a defined outer model radius R a general solution to the potential flow problem in polar coordinates is expressed as

$$\chi_j = K_{nj} J_n \left(c_j^n \frac{r}{R}\right) \exp\left(in\phi\right) \exp\left(-c_j^n \frac{z}{R}\right), \tag{1.9}$$

where

$$\begin{aligned} K_{nj} &: \text{arbitrary coefficients} \\ J_n &: n^{th} \text{ order of Bessel function} \\ r &: \text{radius} \\ \phi &: \text{azimuth angle} \\ z &: \text{height} \\ c_j^n &: i^{th} \text{ zero of } J_n \end{aligned}$$

The coefficients K_{nj} are determined from surface kinematic boundary conditions:

$$w_0 = \frac{\partial}{\partial z}\chi\bigg|_{z=0} = \vec{u}_0 \cdot \nabla h(r,\phi) \tag{1.10}$$

where w_0 is the vertical velocity, $\vec{u_o}$ is the basic state velocity vector, and h is the terrain height. The Bessel functions form an orthogonal set of radial function for each n. Similarly, the azimuthal component $\exp\left(in\phi\right)$ form an orthogonal Fourier series. The coefficients are then calculated independently by projection of the right-hand side of Equation (1.10) onto the sets of functions; the mathematical process is further described in Oberhettinger (2014) .

Polar coordinates are used over the more traditional Cartesian coordinate system due to certain advantages. By defining the point-of-interest as the model center it is simpler to concentrate the resolution there as well as limit the perturbation calculations to this point. Solving for the center (r = 0) gives the solution

$$\nabla\chi_j = \frac{1}{2}(1,i) K_{1j} \frac{c_j^1}{R} \exp\left(-c_j^1 \frac{z}{R}\right). \tag{1.11}$$

The solution to the potential flow perturbation is therefore obtained as a sum of terms obtained through Equation (1.11) from the set of coefficients K_{nj}. Each term also has a specific horizontal length scale $L_j = R/c_j^1$ that describes the depth to which the perturbation extends.

The next step is to modify the potential flow solution to include the effects of surface friction. The current solution neglects turbulent momentum transfer, however, this is not valid near the surface. The inclusion of the effects of the turbulent transfer is limited to a layer of depth l_j where the value of l_j is calculated according to Jensen et al. (1984) :

$$l_j = 0.3 \cdot z_j \left(\frac{L_j}{z_j} \right)^{0.67} \tag{1.12}$$

where z_j is the roughness length. For homogeneous conditions $z_j = z_0$.

The turbulent transfer forces a balance between the stress and wind shear at heights much lower than l_j which results in a logarithmic profile. However, at heights comparable to l_j the flow perturbations reach a maximum and is not accurately predicted by the potential flow solution. The profile at this height is corrected in each term by adding a perturbation at the given height of magnitude Δu_j

$$\frac{\Delta \vec{u}_j(z)}{|u_0(z)|} = \frac{|u_0 (L_j)^2}{\left| u_0 \left(z_j' \right) \right|^2} \nabla_{x_j}, \tag{1.13}$$

where z_j' is $z_j' = \max(z, l_j)$.

The calculations that have been described up till now are done on a grid such as the one shown in Figure 1.7. The point-of-interest is defined as the center and has the highest grid resolution. The grid size increases radially by a factor of 1.06. The required information from the grid is the height of the terrain at each grid point, but this is more conveniently done in the form of contour lines.

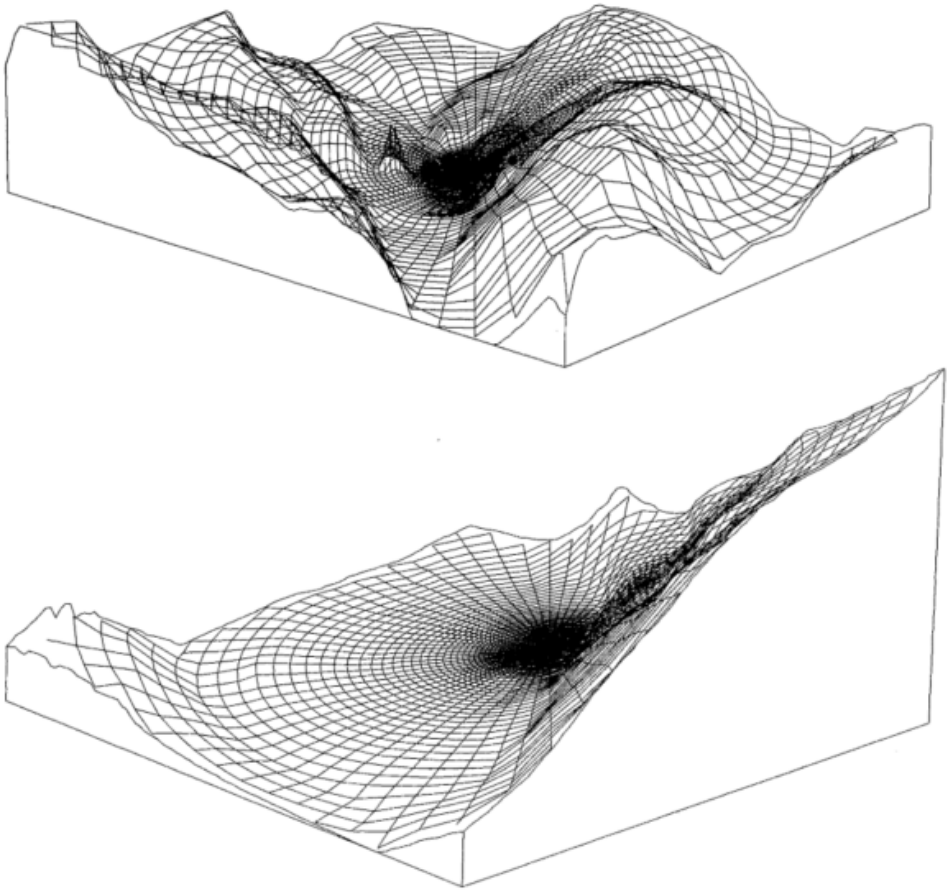

Figure 1.7: A portion of the Great Glenn Valley is shown with polar zooming grid centered at the meteorological station Fort Augustus. The bottom figure is a zoomed in section (2 km length) of the top figure (12 km length). The vertical scale is exaggerated by a factor of 5 (Troen & Petersen, 1989).

1.2.1 Wind Atlas Analysis Model

WAsP is comprised of two main models; the analysis model and the application model. The analysis model is built from the aforementioned submodels. Using measured wind data, local terrain roughness, obstacles, and orographic data, the local wind conditions are described in the form of averaged Weibull parameters. Figure 1.8 shows a flowchart of how the analysis model functions.

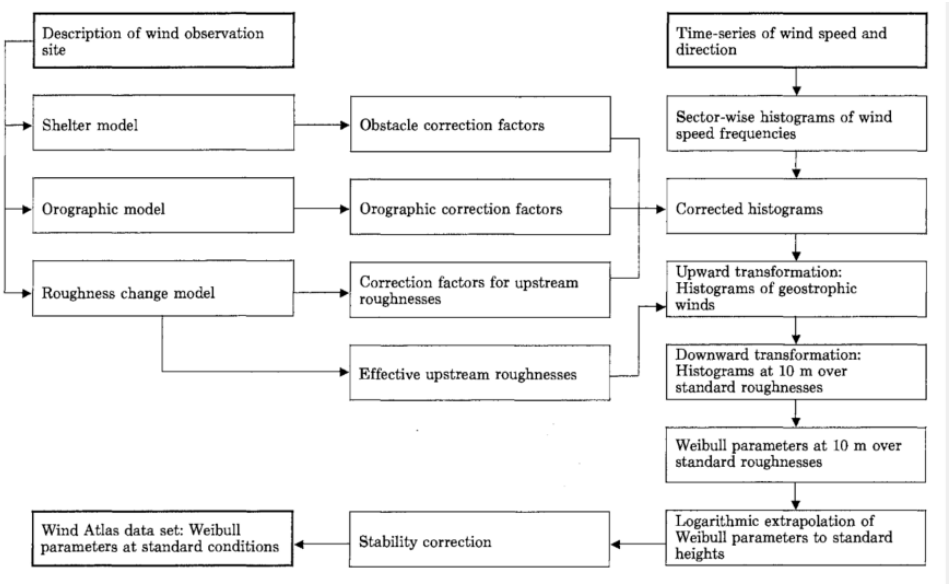

Figure 1.8: Flowchart of the Wind Atlas analysis model (Troen & Petersen, 1989).

Summarized, the procedure takes input data in the form of the frequency of occurrence of the wind speed in histograms of 1 m/s bins for each of the azimuthal sectors. The correction factors calculated by the above-mentioned submodels are also determined for each azimuthal sector. For each sector the correction factors are applied to the binned wind speed histograms. Using the effective upstream roughness with the corrected histograms the geostrophic drag law is used to determine the histograms for the geostrophic winds which in turn can be invoked by the logarithmic wind profile to determine the histograms at 10 m using standard roughness'. At the standard level of 10 m the frequency of occurrence is extracted in the form of the Weibull parameters. Extrapolating the Weibull parameters to other standard heights is done using the logarithmic wind profile with stability correction given in Equation (1.6). Finally, the stability correction model, omitted in this paper, corrects for the 'contamination' of the mean and standard deviation values due to the effects of stability at different standard heights; resulting in the Weibull parameters are standardized conditions.

1.2.2 Wind Atlas Application Model

The application model is designed to be as close to an inverse model to the analysis model and is schematically shown in Figure 1.9. It uses the Weibull parameters at standard conditions as well as a description of the wind energy conversion system (WECS) as input instead of wind measurement data. In practice this model serves as a siting tool for Wind Atlas users.

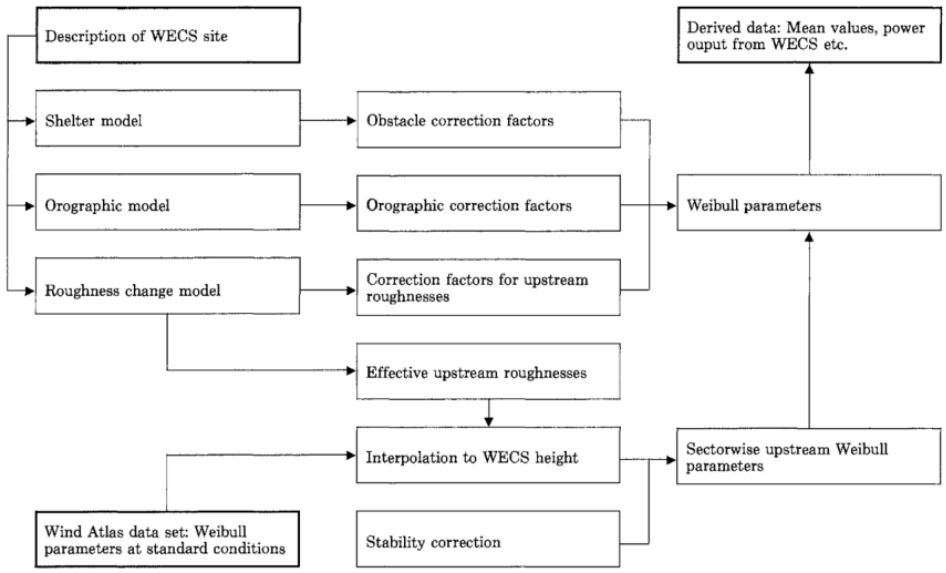

Figure 1.9: Flowchart of the Wind Atlas application model (Troen & Petersen, 1989).

1.2.3 Performance Indicators

WAsP is capable of making accurate predictions within its operational envelope. Beyond this there can be large prediction errors who's magnitude is dependent on the degree to which the operational envelope is exceeded. Two performance indicators, or metrics, are used by WAsP as a method to assess whether a site is suitable for the WAsP method.

Cross Correlation

The cross-correlation is used as a metric for the suitability for the prediction methods used in WAsP. The cross-correlation is taken between the reference and prediction sites to determine whether they are subject to the same weather regime. The metric only provides a limited picture of the suitability of the method as there is no apparent relationship between the magnitude of the prediction errors and the cross-correlation (Bowen & Mortensen, 1996). Additionally, the cross-correlation is not capable of discerning the sign of the prediction error. Therefore, a high cross-correlation value alone is not enough to indicate the suitability of WAsP.

Orographic Indicator

Large prediction errors are often assumed to be due to the inherent limits of the stability and orographic models used in WAsP. The orographic indicator provides a metric to which the terrain at a site exceeds the operational envelope of the orographic model described in Section 1.2.0.1.

Considering only the effects of orography the prediction error is shown in Bowen and Mortensen (2004) to be:

$$U_{P_e} = U_{P_m} + (E_2 - E_1)\,, \tag{1.14}$$

where U_{Pe} is the estimated speed at the prediction site, U_{Pm} is the measured speed at the reference site, and E_2 & E_1 are their associated errors respectively. These errors come from the speed-up correction for orographic effects, e.g. predicting the wind at a rugged site using a flat reference site. The magnitude of the errors are related to the degree in which the specific site exceeds the operational limits and the sign of the overall error can be either positive or negative and signifies over over- or under-prediction.

The practical orographic indicator used is ΔRIX, which uses the local RIX values of the prediction and reference sites. For a given site the RIX value is defined as the fractional extent to which the surrounding terrain exceeds a critical slope of $\theta_c = 0.3$. For reference WAsP's operational envelope in terms of RIX is $\backsim 0\%$ (Mortensen et al., 2006).

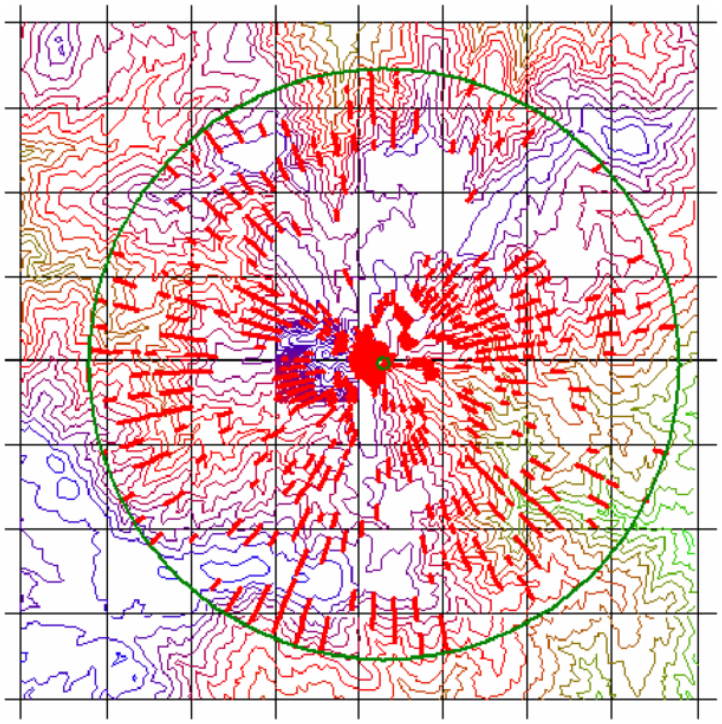

Figure 1.10: The terrain centered about a met. station site as seen in the WAsP Map Editor. Terrain steeper than a certain critical angle, θ_c, is indicated by the thick red (radial) lines (Mortensen et al., 2006).

The RIX value is determined by a number of radial lines of radius R originating at the desired site. Each radii is divided into segments defined by the crossing of the of the radial line with the contour lines. These line segments, shown in Figure 1.10, represent the slopes greater than the critical slope θ_c. The RIX number is thus calculated as the sum of the line segments divided by the total sum of the radial lines. A sites RIX value is therefore dependent on the calculation radius R, critical slope value θ_c, and the number

of radial lines N. The parameters have the following default value, but can be altered:

$$R = 3.5\text{km}$$
$$\theta_c = 0.3$$
$$N = 72.$$

The radius of 3.5 km was originally set by Bowen and Mortensen (1996) and Bowen and Mortensen (2004) for convenience, though it has since been found that the area within this radius most strongly influences the prediction results. The critical slope value comes from the assumption that the lower bound of flow separation occurs at a fixed value. The value itself is a conservative estimate based the analysis of Wood (1995) . Using the coefficient of determination R^2 Mortensen et al. (2006) varied the radius and critical slope values. A local maxima was found using R = 3.5 km and $\theta_c = 0.45$, however, the differences were only a few percent. An exact choice of these parameters may not be critical to the accuracy of the model predictions.

The orographic indicator ΔRIX takes the difference between the RIX value at the prediction site and the reference site:

$$\Delta RIX = RIX_{pred} - RIX_{ref} \tag{1.15}$$

A zero value for ΔRIX means that the two sites are equally rugged. A positive value ($\Delta\text{RIX} > 0$) indicates that the prediction is overestimated and similarly a negative value ($\Delta\text{RIX} < 0$) indicates an underestimation of the prediction.

Field validation of the orographic performance indicator was performed by Mortensen et al. (2008) using measurement data from complex terrain in northern Portugal spanning 3½ years. The terrain in question involves five sites located in a mountainous region with a RIX index between 10 and 33%. The validation used the site data and performed 25 cross-predictions including self-predictions at each site. Figure 1.11 plots the logarithm of the ratio between the predicted and measured wind speeds against ΔRIX. The relation appears to be linear. Assuming this linear behavior allows for the derivation of the following expression:

$$U_{\text{m}} = \frac{U_{\text{p}}}{\exp(\alpha \Delta\text{RIX})} \tag{1.16}$$

where α is the slope of the regression line. This equation provides a method to use ΔRIX as a correction to the predicted wind speed U_p to recover the 'measured' wind speed at the same height.

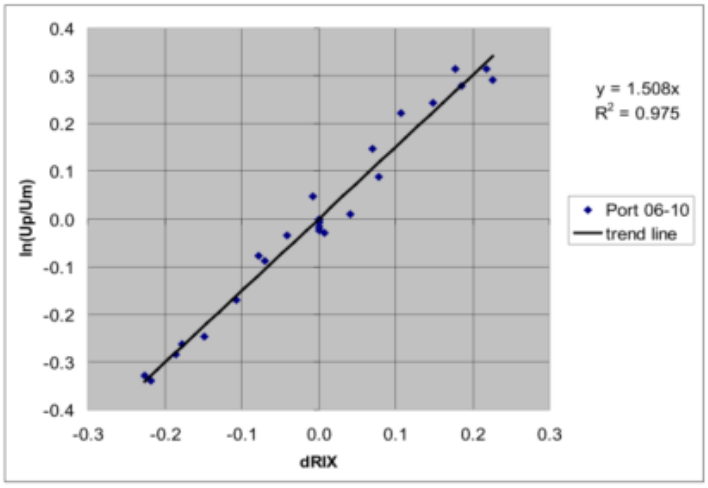

Figure 1.11: WAsP wind speed prediction error vs. ΔRIX (given as a fraction) Mortensen et al. (2008) .

A similar procedure is also applicable to the power production. Applied to a 23-MW wind farm located in terrain with RIX values between 4 and 14%. Without the use of the correction factor WAsP overestimated the power production by 13%. With the correction factor this overestimation was reduced to 3%, i.e. a 70% improvement in the annual energy production (AEP).

The introduction of the orographic performance indicator and the ΔRIX correction factor addresses the reality that WAsP was being increasingly used for terrain exceeding the operational envelope of the model. However, it is required that the slope of the regression line α is obtainable and valid for surrounding sites of similar terrain.

Further validation of the ΔRIX correction factor comes from the development of WAsP-CFD. The purpose of WAsP-CFD is to provide a more physically correct method of prediction the average wind speeds in locations of very complex terrain. Verification of WAsP-CFD is done by Cavar et al. (2016) where the Ellipsys3D RANS solver is compared to OpenFoam v.1.7.1 and OpenFoam v.2.2.1 which offered the same wall-modelling approach. It was found that the results were very similar using v.1.7.1 and almost identical using v.2.2.1. Comparisons between the IBZ model, with and without ΔRIX, and the RANS solver were made by Troen et al. (2014) . The specifics regarding the location details were covered by Non-Disclosure-Agreements, however the terrain was considered complex. It was found that the results from the IBZ model with ΔRIX and the 'Ellipsys' RANS solver (Cavar et al., 2016) were in close agreement and supports the skill of ΔRIX as a correction factor.

1.3 Surface Characterization

The field of material science has seen many studies on the micro-scale structure of a surface. The roughness at these scales is indicative of many functional material properties, such as friction, adhesion, and thermal/electrical conductivity. As a result there are

several standards describing measurement techniques and surface characteristics such as ASME B46. Recently, methods involving the power spectral density (PSD), such the Persson's scaling theory for contact (Dapp et al., 2014), have become increasingly utilized though only the method involving the PSD will be considered.

1.3.1 Surface Characterization using Spectral Analysis

The PSD is the Fourier transform of the auto-correlation function of the signal and describes the distribution of power in terms of the frequency components of the signal. I.e. a surface is decomposed into the frequency contributions that make up the micro-scale structure of the surface. The use of the PSD provides statistical information about the topography which can be used to determine, e.g. the aforementioned functional material properties. Several models, as mentioned by Jacobs et al. (2017) , have been created to determined such surface properties from three scalar parameters that are most easily calculated from the PSD, namely: the root-mean-square (RMS) height h_{rms}, the RMS slope h'_{rms}, and the RMS curvature h''_{rms}. In the work by Flack and Schultz (2010) they found that the first parameter, h_{rms}, as well as the skewness of the surface height probability held the strongest correlation to the hydrodynamic roughness length. And though the scale of the features being investigated in this report is far larger than that of the hydrodynamic roughness length, it does indicate that there is value in investigating the same metrics to determine terrain ruggedness.

1.3.1.1 PSD

The practical determination of the PSD has been shown by Jacobs et al. (2017) to be inconsistent. There are several methods of calculating the PSD from measured data which use different units and lead to different numerical results. The previously described calculations can be applied in different ways to either 1-D or 2-D signals.

Line-scans provide a 1-D signal of the surface, giving a symmetric PSD C^{1D} as a function of the wavevector q shown in Figure 1.12(b). The units are m^3 and m^{-1} for C^{1D} and q respectively such that the area under the curve, equal to h^2_{rms} has the units of m^2. Due to symmetry about zero C^{1D} is often plotted in only the region $q > 0$ and denoted as C^{1D+}. This must be considered when calculating h^2_{rms} such that the area under the curve is multiplied by 2:

$$h^2_{\mathrm{rms}} = \frac{1}{\pi}\int_0^\infty C^{\mathrm{1D+}}\left(q_x\right)\mathrm{d}q_x \tag{1.17}$$

Surface-scans provide a 2-D signal, or a topographical map. The 2-D PSD, denoted as C^{2D}, is visualized by a surface as shown in Figure 1.12(e). The units of the PSD is in this case m^4 whilst the two wavevector directions are m^{-1} such that the volume under the surface has the units of m^2.

$$h^2_{rms} = \frac{1}{4\pi^2}\int_{-\infty}^\infty\int_{-\infty}^\infty C^{2D}\left(q_x, q_y\right)\mathrm{d}q_x\mathrm{d}q_y \tag{1.18}$$

As with the 1-D signal, vertical cross-sections of C^{2D} that pass through the origin $q_x = q_y = 0$ are symmetric. However, the surface is not necessarily radially symmetric. It should be noted that the above equations assume the mean of the signal is zero.

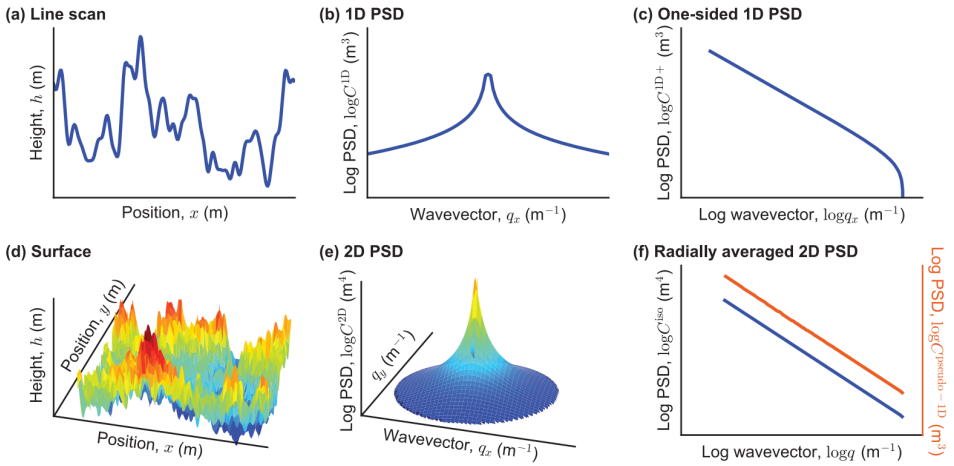

Figure 1.12: Examples of various plots generally referred to as 'PSD'. A 1-D line scan $h(x)$ (a) can be presented by (b) a 1-D PSD $C^{1D}(qx)$. However it is more commonly represented by (c) a one-sided 1-D PSD $C^{1D+}(q_x)$. A 2-D topographic scan $h(x, y)$ (d) can be presented by (e) a 2-D $C^{2D}(q_x, q_y)$, a surface in reciprocal space q_x, q_y. Radially symmetric surfaces (isotropic) typically only show the radial average C^{iso} as seen in (f) Jacobs et al. (2017) .

Calculating the PSD

Assuming the height signal is known by the continuous function $h(x)$ over a line L_x; the forward and inverse Fourier transforms are given as:

$$\tilde{h}_{q_w} = \int_{L_x} h(x) e^{-iq_x x} dx \tag{1.19}$$

$$h(x) = \frac{1}{L_x} \sum_{q_x} \tilde{h}_{q_x} \mathrm{e}^{\mathrm{i}q_x x} \tag{1.20}$$

Real surfaces, however, can not be described as a continuous signal of heights $h(x)$. Measurements can only be done on discrete locations with finite resolutions over finite regions. Typically, measurements are obtained on a grid with N_x grid points and a 'resolution' defined as $l_x = N_x/L_x$, Equations (1.19) and (1.20) become the discrete Fourier transforms (DFT):

$$\tilde{h}_{q_x} = l_x \sum_{x} h_x \mathrm{e}^{-iq_x x} \tag{1.21}$$

$$h_x = \frac{1}{L_x} \sum_{q_x} \tilde{h}_{q_x} \mathrm{e}^{\mathrm{i}q_x x}. \tag{1.22}$$

For the discrete Fourier transforms (DTF) the integral occurs over the entire length and the summation runs in steps of $\Delta q_x = 2\pi/L_x$ from $q_x = 0 - 2\pi(N_x - 1)/L_x$. The 1-D PSD is thus given by:

$$C_{q_x}^{1\mathrm{D}} = L_x^{-1} \left| \tilde{h}_{q_x} \right|^2 \tag{1.23}$$

This formulation of the 1-D PSD is compatible with the standards set by SEMI MF1811. The DFT is most commonly obtained using the fast Fourier transform (FFT). The methodology behind this algorithm can be found in Van Loan (1992) and Welch (1967) .

Calculating the RMS Parameters

A true calculation of the three scalar parameters requires information about the surface topography at all scales. Though since measurements are finite the calculated parameters are only approximations.

Typically, single surface characteristics have been shown to be dominated by one of the three calculated parameters. E.g. contact stiffness is largely dependent upon the RMS height, whilst true contact area depends on RMS slope and curvature (Persson et al., 2004; Pohrt & Popov, 2012). In this report only the first two parameters will be considered.

The derivation to the final form of the RMS parameters for a 2-D case can be found in Jacobs et al. (2017) . The following equations have been reduced to be used with 1-D signals:

$$h_{rms}^2 = \frac{1}{R} \sum_k C_k^{1D} \tag{1.24}$$

$$h_{rms}'^2 = \frac{1}{R} \sum_k k^2 C_k^{1D} \tag{1.25}$$

where R is the radius and k is the wavenumber.

1.3.2 Application to Ruggedness Characterization

The RMS parameters are on micro-scale structures used to derive characteristics like roughness. Applied to terrain they might be able to provide information about the terrain ruggedness/complexity. An initial attempt to categorise site ruggedness using the standard deviation σ_z of the grid-point heights was done by Mortensen et al. (1993) . Further exploration of this index was pursued by Bowen and Mortensen (2004) . Their analysis looked at an area of 1 km^2 around each site as the larger area of 8 km^2 normally used for WAsP was less capable. Contour heights were converted to spot heights on a 10 m orthogonal grid for which σ_z was calculated. WAsP predictions were carried out at the standard 10 m altitude. The analysis performed by Bowen and Mortensen (2004) found a weak relationship between the prediction error and index indicating sign and magnitude of the orographic prediction error.

However, there are certain limitations of the previous attempts. First, the area of investigation was taken as a square area around the site. And σ_z was calculated

omnidirectionally for the area. But, wind is directional. And therefore, the effects of roughness and orography should be considered to be directional. Calculating the RMS height as a function of the direction, or sector, may offer an improvement to the metric. Secondly, for RIX it was found that a radius of 3.5 km offered the best results. It is then conceivable that a larger area than 1 km^2 is necessary to obtain a reasonable value of σ_z. Thirdly, for a given wind direction it is the upstream roughness and orography that is of interest when looking at the wind. Therefore, a change in the shape of the calculation area may offer better results. Finally, it may be useful to look at the RMS slope when characterizing the terrain ruggedness.

CHAPTER 2
Methodology

This chapter will describe the routines used for data acquisition. The data acquisition is split into three main parts: (i) the map creation, (ii) the RIX calculator, and (iii) the PSD calculation. The required input parameters for the main routines will also be given along with the description of the working process. The main scripts used are found in Appendix C.

2.1 Overview

Digital elevation maps (DEM) of the aforementioned regions in Norway were downloaded in 50, 10, and 1 meter resolutions from Kartverket. Due to file size limitations and the large areas requested, the maps were delivered in pieces that needed to be sewn together to create one large coherent map. Each map piece had an associated .tfw, or world file, that described the geographic location of that piece. The puzzle counter routine shown in Figure 2.1 uses these locations to determine a reference file (top-left) to be used in the map creation. Using the reference file and its coordinates the individual map files (GEOTIFF) are pieced together to create one large map. Area-of-interest for each map are given by coordinates that are fed to both the RIX and Spectra routines to return the RIX values and sector wide power spectrums for each area-of-interest.

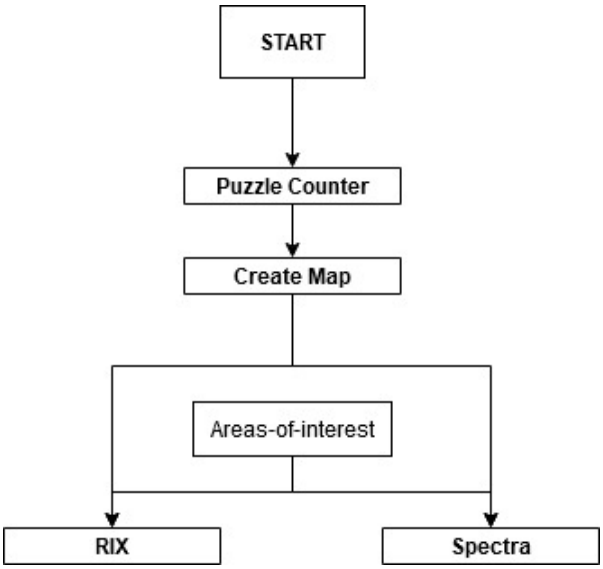

Figure 2.1: Overview of data acquisition method.

2.1.1 Create Map Routine

A diagram of the create map routine is shown in Figure 2.2 and requires the following inputs:

Input	Description
Map files	Sets the path to the regions map files.
Coordinate array	An array of each map files reference coordinates (top-left).
Reference	A dictionary of the reference map file name and coordinates.
file_dict_tif	A dictionary of all the map file names and coordinates.

Table 2.1: Table of inputs for the create map routine.

The create map routine takes in above mentioned inputs and first pre-allocates memory for the combined map. Each map file is opened individually in a loop and placed into the pre-allocated array based on its referencing coordinates and the combined maps true reference coordinates. Each map file is also inspected for its upper and lower bounds in the X & Y axis to set the extent of the combined map. Finally any missing data points, or NaN values, are corrected to zero.

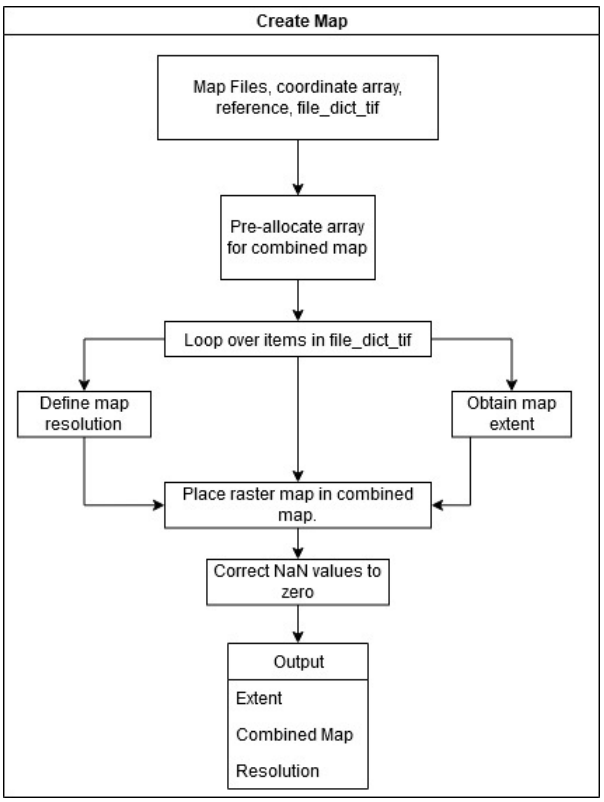

Figure 2.2: Diagram of the create map routine.

2.1.2 RIX Routine

A diagram of the RIX calculation routine is shown in Figure 2.4 and requires the following inputs:

Input	Description
Areas-of-interest	X & Y coordinates of areas/sites to calculate RIX.
Combined map	The combined map array.
Reference	A dictionary of the reference map file name and coordinates.
FD_scheme	Indicate which finite difference scheme to use.
# of radial lines	The number of radial lines to use for RIX (default: 72).
Radius	Length of the radial lines (default: 3500 m).
Critical slope	The critical slope described in the RIX method (default: 0.3).

Table 2.2: Table of inputs for the RIX routine.

Using the inputs above the RIX routine first calculates the location indices of the site and angle between the radial lines. Looping over each angle the radial line, which describes the indices on the array, is calculated in polar coordinates with a length of $\frac{R}{resolution}$ and angle of the line. The line itself uses geometric progression as given by:

$$a_n = ar^{n-1} \tag{2.1}$$

with the end point fixed to be $\frac{R}{resolution}$. By converting the radial line to Cartesian coordinates these indices, now in X & Y, are used to determine the elevation signal. A bilinear interpolation sub-routine is used to calculate the values between the points of the array. The bilinear interpolation sub-routine is constructed according to Figure 2.3 and Equation (2.2).

$$\begin{aligned} P &= \frac{(x_2 - x)(y_2 - y)}{(x_2 - x_1)(y_2 - y_1)} Q_{11} + \frac{(x - x_1)(y_2 - y)}{(x_2 - x_1)(y_2 - y_1)} \\ &= Q_{21} + \frac{(x_2 - x)(y - y_1)}{(x_2 - x_1)(y_2 - y_1)} Q_{12} + \frac{(x - x_1)(y - y_1)}{(x_2 - x_1)(y_2 - y_1)} Q_{22} \end{aligned} \tag{2.2}$$

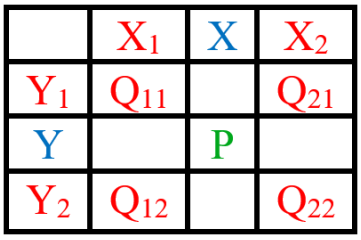

Figure 2.3: Description of the points used in bilinear interpolation.

Slopes are calculated using a finite difference sub-routine and the total percentage of slopes greater than the critical slope is calculated for all radial lines then averaged to give the total RIX number.

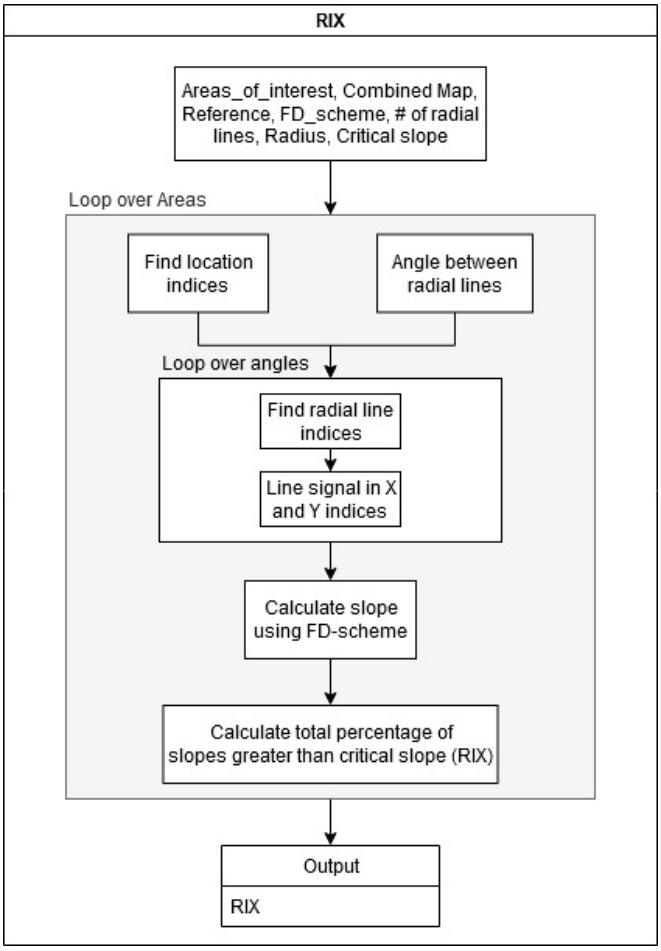

Figure 2.4: Diagram of RIX routine.

2.1.3 Spectra Routine

A diagram of the PSD calculation routine is shown in Figure 2.5. The routine calculates a 1-D spectrum which can readily derived from the equations given in Section 1.3.1.1 and requires the following inputs:

Input	**Description**
Areas-of-interest	X & Y coordinates of areas/sites to calculate RIX.
Combined map	The combined map array.
Reference	A dictionary of the reference map file name and coordinates.
# of sectors	Number of sectors in 360 degrees (default: 12).
Radius	Length of the radial lines.

Table 2.3: Table of inputs for the Spectra routine.

Similarly to the RIX routine the location indices of the specific site is calculated. The radial area around the site is divided into 12 sectors as per convention. Looping over the sectors with a predefined number of lines per sector (default: 10) the radial line index is calculated in polar coordinates using the length $\frac{R}{resolution}$ and angle of the line. The line itself uses linear progression unlike the RIX routine. The radial line indices are then converted to Cartesian coordinates which in turn are used to get the elevation signal. The aforementioned bilinear interpolation sub-routine is also used to interpolate for points in the combined map. The lines in each sector are averaged in the azimuthal direction to get a mean sector wide line signal. Finally, the PSD is computed by taking the FFT of the signal with the mean subtracted out as described in Section 1.3.1.1. This is equivalent to the Welch method (Welch, 1967) with a boxcar window.

The terrain-slope spectra is computed in a similar fashion where the slopes of the elevation signal are calculated using the finite difference sub-routine.

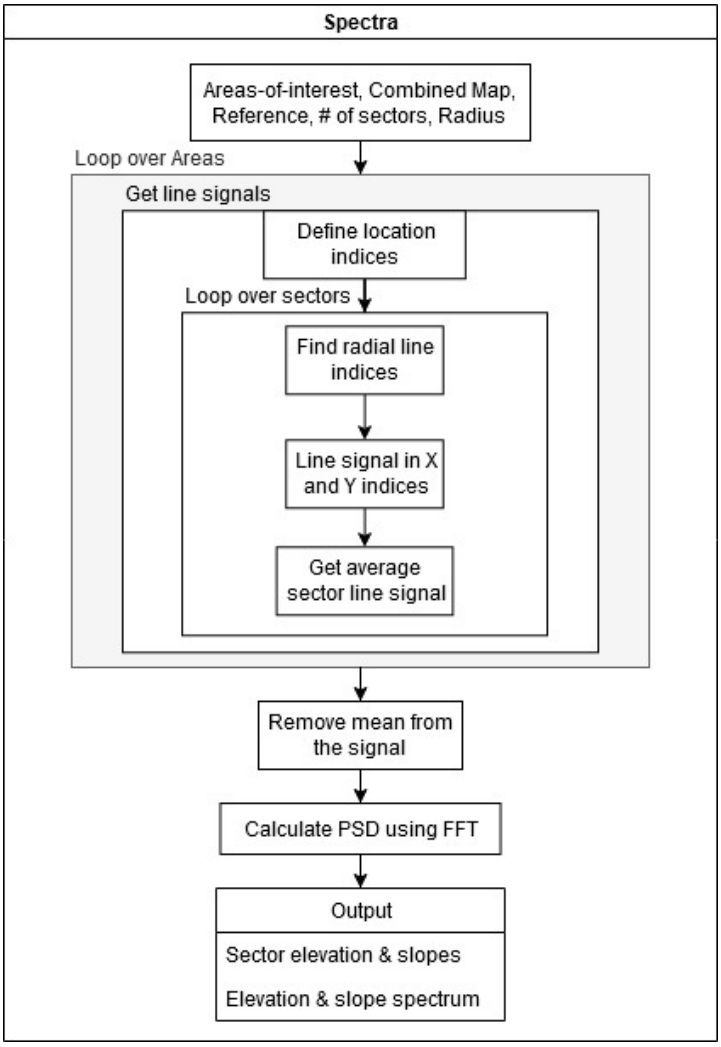

Figure 2.5: Diagram of Spectra routine.

2.2 Verification

This section will go over the comparison/verification of the data acquisition routines described above. Note naming convention of areas is adopted from the naming convention used in Jakobsen et al. (2019) .

2.2.1 RIX Comparison

A comparative study between the RIX routine and the RIX calculated by WAsP was performed for sites in Finnmark, Norway shown in Figure 2.6. The comparison was done using WAsP's default values for RIX which are listed in Section 1.2.3.

The RIX routine was implemented according to the description given in Section 1.2.3. However, prior to the comparison it must be noted that even though the RIX calculator is methodically correct, certain differences will arise due to the differences in input format and sub-routines. This report uses raster maps in GeoTIFF format whilst WAsP uses vector maps. To use the same maps in WAsP the GeoTIFF maps were converted to the supported .map format using GDAL's contour command to build vector contour lines from the raster data.

Among the differences between raster and vector maps is that raster maps have a set resolution throughout whilst the resolution in vector contour maps is dependent on the contour spacing. A consequence of this is that areas of smaller contour spacing have a higher artificial resolution and vice versa. Additionally, the radial lines in used by WAsP have a geometric radial step and functions as a method to increase the weighting given to nearby terrain. This has been incorporated into the RIX routine by using geometric progression as described in Section 2.1.2.

Through inspection of WAsP's source code it was found that the slope is calculated using mainly first-order forward differencing and cubic spline schemes. The data collection from the self-made routines will be done using only first-order forward differencing and first-order backward differencing for the last point.

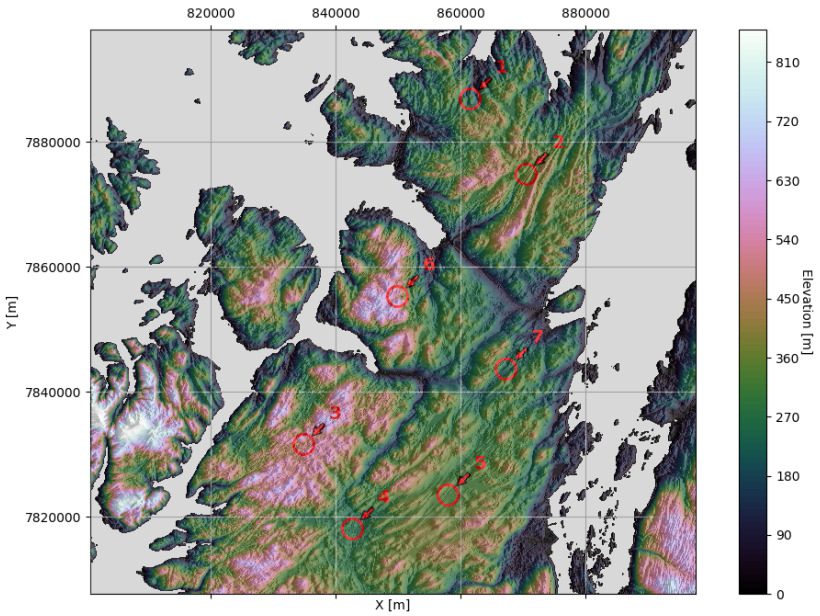

Figure 2.6: Sites for RIX comparison at Area 44. Map projection: WGS 84 / UTM zone 33N.

		WAsP		RIX Routine	
Site	X & Y	50 m	10 m	50 m	10 m
1	861,445 7,887,003	3.2	5.3	5.4	4.4
2	870,471 7874895	0.5	1.6	0.4	0.9
3	834,758 7,831,595	2.7	5.1	4.7	5.0
4	842,586 7,818,136	0.0	0.0	0.0	0.0
5	857,969 7,823,625	0.0	0.0	0.0	0.0
6	849,825 7,855,310	3.6	4.2	9.7	9.5
7	867,227 7,843,745	0.1	1.3	0.3	1.4

Table 2.4: RIX values at 50 m and 10 m resolution. Both RIX routine and WAsP values calculated using radius of 3.5 km, 72 radial lines, and $\theta_c = 0.3$.

The results in Table 2.4 show the RIX values given by WAsP and the self-made RIX routine using 50 and 10 m resolution maps at the locations shown in Figure 2.6. It is clear that the two different methods produce different RIX values in both map resolutions.

Generally it appears that WAsP is sensitive to the map resolution and calculates larger RIX values for finer maps. Only the 10 m maps appear to cohere with each other, albeit only slightly. Though there is deviation, it appears that the RIX routine calculates a more consistent RIX value though this will be elaborated upon in Section 3.1.2. For ease of use this report will continue to use the the self-made RIX routine as a tool of comparison to the low-order statistics. However, further effort should be made towards acquiring a sizeable sample of WAsP produced RIX values in the areas-of-interest to ensure that any relations or conclusions hold true.

2.2.2 PSD Verification

Verification of the PSD of the elevation and slope signals can be done by using the definition of the PSD. As previously described in Section 1.3.1.1 using Equation (1.24), the variance, or first RMS parameter, of a signal can be obtained by calculating the area under the curve of the PSD. As per convention only the positive portion of the PSD is included and should yield half the variance of the input signal. Therefore, it is possible to verify the results of the PSD by showing that the variance calculated from the summation of the spectra is half the variance of the elevation/slope signal. A constant factor of $(2\pi)^2$ is multiplied to the variance calculated via the PSD.

The results in Table 2.5 are a sample of this 'sanity check' and are obtained from site 1 of the same area as presented in Section 2.2.1 four different sectors. It is clear that the variance obtained from the one-sided PSD is half of the variance calculated from the elevation signal indicating that the PSD is correct.

	50m		**10m**	
Sector	σ_h^2	σ^2	σ_h^2	σ^2
1	1688.1	3376.2	2220.6	4441.3
2	1880.4	3761.2	2105.7	4211.5
3	784.6	1569.8	1493.9	2987.9
4	437.1	874.3	585.6	1171.3

Table 2.5: Comparison of the variance σ_h^2 calculated from the PSD of the elevation signal and the variance σ^2 calculated directly from the elevation signal. A sector is defined as a 30° wedge. Sector 1 is centered about 0° in Cartesian coordinates moving counterclockwise.

CHAPTER 3
Data Analysis

Using the methodology described in the previous section data is obtained for the areas and sites described in Appendix A. The analysis is performed at each site in three resolutions: 50, 10, and 1 m. The PSD of the terrain-slopes is obtained in this report using two methods. The first method, denoted as $\sigma_{dh/dx}$, involves following Equation (1.25) where the PSD is multiplied by the wavenumber squared. The second method, denoted as $\sigma_{\Delta h/\Delta x}$, involves calculating the slopes of the elevation signal using a finite difference scheme as described in Section 2.1.3. These two methods are expected to yield differing results due to the truncation error of finite difference scheme which will result in loss of variance at higher wavenumbers.

Due to sections of missing data in either the 10 or 1 m resolution maps, the affected sites are excluded from the analysis. Additionally, there are sites with incoherent elevation data across map resolutions which are also excluded. The specific sites affected by this are further specified in Appendix A.

3.1 Map Resolution Comparison

Digital map data has typically been available as vector contour maps for a variety of reasons, among them being less computationally expensive to store and use. With the advent measurement campaigns making high resolution digital maps in raster format available for research, as well as increasing computational capacity, it is important to determine to which degree finer maps can be used to reduce the uncertainty associated with land-surface interactions. and improve the results of e.g. WAsP. This section will focus on the effect of the three different map resolutions by looking at the probability density function (PDF) of the slopes, referred to as $\Delta h/\Delta x$, to gain an understanding of how the grid data differs. Additionally, the effect the resolution has on RIX, σ_h, $\sigma_{dh/dx}$, and $\sigma_{\Delta h/\Delta x}$ is investigated.

3.1.1 Slope Distribution

Figures 3.1 to 3.4 show the site averaged PDF's for all sites in the area, excluding the sites in the 1 m PDF due to missing data as described in Appendix A. The plots show a clear similarity in that the distribution of slopes across resolutions are in coherence. The less packed Figure 3.1 gives a clearer picture of how the shape of the distribution changes depending on the resolution and indicates that the finer maps have a more smoothed bell-shaped curve. The similarity of the slope distributions across the resolutions indicates

that the resulting RIX, σ_h, $\sigma_{dh/dx}$, and $\sigma_{\Delta h/\Delta x}$ values should on average not deviate greatly.

Comparing the areas themselves it is possible to see variations in the kurtosis of the curves. This is especially noticeable comparing Figure 3.4. Differences in the kurtosis are attributed to the leading geological process that shaped the terrain. At the scales relevant to this analysis the local geological processes may differ substantially. It should also be noted that individual sites display a positive/negative skewness. This can be written off as a product of the location of the site itself and over a wide range evens out to a median value.

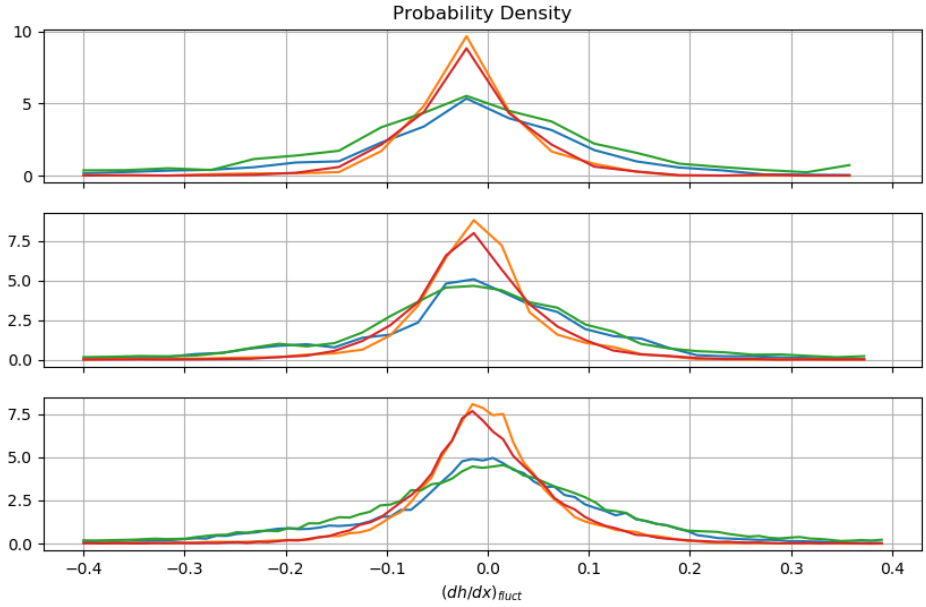

Figure 3.1: Area 44 PDF's at 54 at 50, 10, and 1 m map resolution as seen from the top.

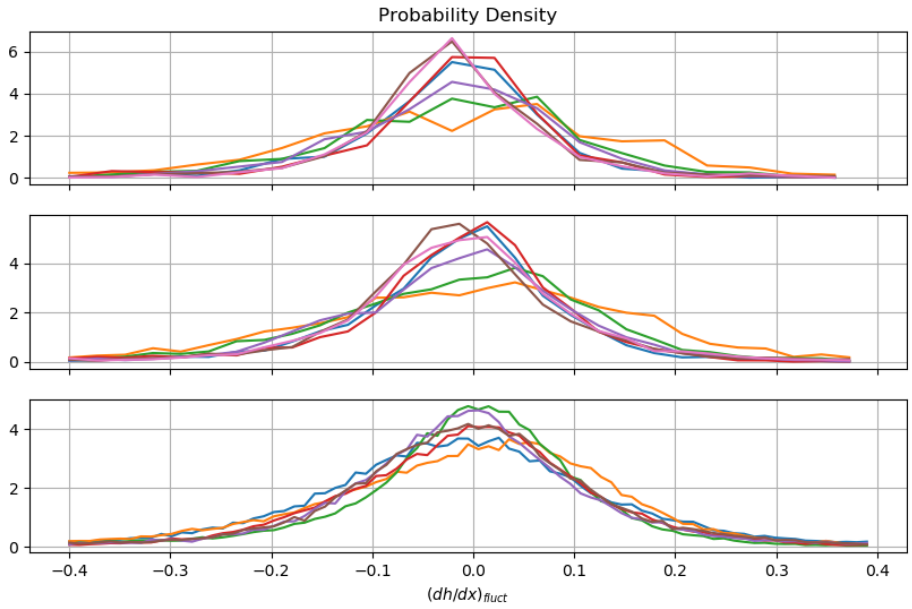

Figure 3.2: Area 53 PDF's at 54 at 50, 10, and 1 m map resolution as seen from the top.

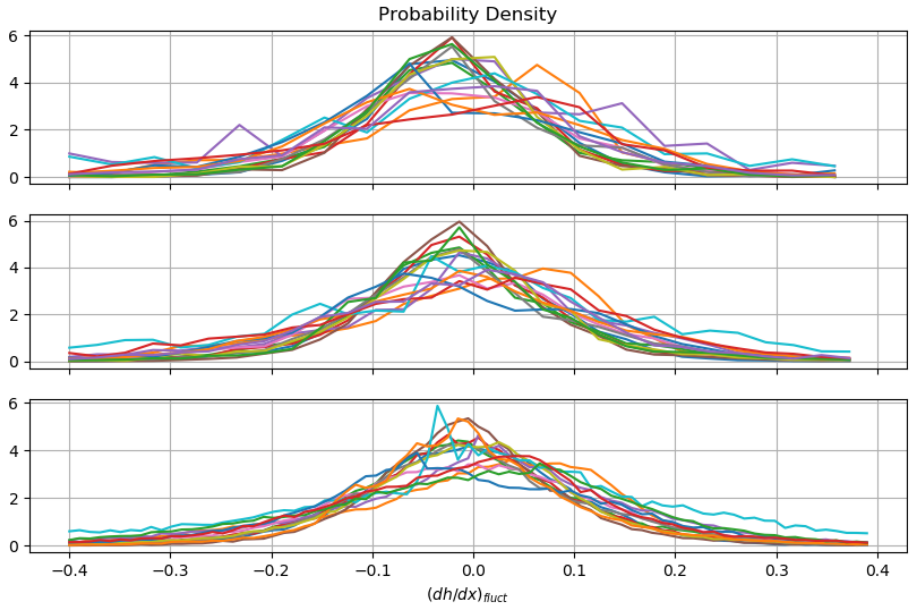

Figure 3.3: Area 54 PDF's at 54 at 50, 10, and 1 m map resolution as seen from the top.

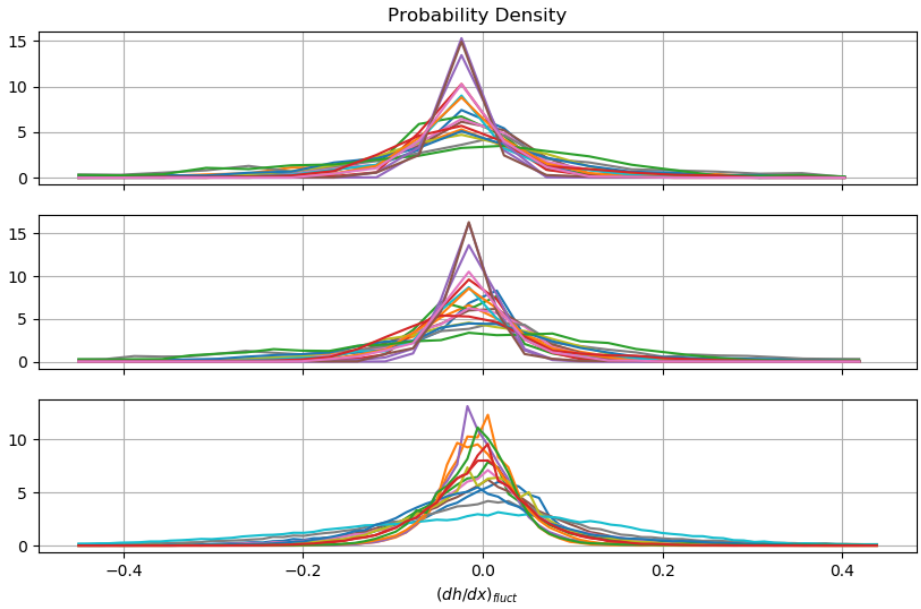

Figure 3.4: Area 56 PDF's at 54 at 50, 10, and 1 m map resolution as seen from the top.

3.1.2 Effect of map resolution on RIX Calculation

Figure 3.5 shows difference between the calculated RIX values over the three resolutions. The data used has been filtered to exclude missing and inconsistent elevation data across the resolutions as defined in Appendix A. The differences in the calculated RIX values between the 50 and 10 m maps show that there is a concentration of values around 0 to 5 though a large portion of the sites deviate even further resulting in a mean difference of 3.4 and a standard deviation of 5.2. The finer resolution map further exacerbates the spread giving a mean difference of 7.8 and a standard deviation of 6.6.

	Mean	**Std**
50 & 10 m	3.4	5.2
10 & 1 m	7.8	6.6

Table 3.1: Mean and standard deviation of computed RIX differences with differences calculated as 10m - 50m and 1m - 10m.

In both scatter plots it is clear that using finer resolution maps result in larger RIX values. Looking back at Table 2.4, though the sample size is limited, this was also true when using WAsP where going from 50 m to 10 m map resolution resulted in greater RIX value. It is also important to note that the increase in calculated RIX value is not consistent throughout and therefore can not be taken into account. Though a larger sample size of WAsP produced RIX values is required, it may be reasonable to assume that the method behind RIX is quite sensitive to the map resolution, and with finer maps becoming increasingly available in more areas it may become important to specify the operational limits of the metric to ensure proper use.

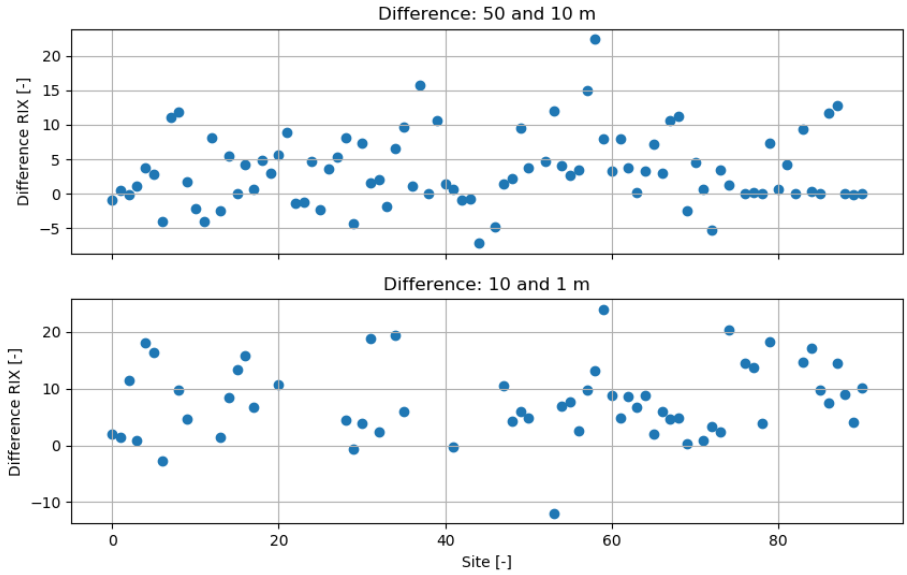

Figure 3.5: Difference in calculated RIX values computed as 10m - 50m and 1m - 10m. The x-axis is defined as the cumulative site number in chronological order.

3.1.3 Effect of map resolution on PSD

The data presented in this section is filtered in the same manner as in Section 3.1.2. The σ values used in this section are, for ease, averaged over all sectors to give a site-averaged value. The differences in the PSD across resolutions, shown in Figures 3.6 to 3.8, contrast the RIX values and are very much concentrated around zero with a handful of values acting as outliers. From these scatter plots it appears that there is very little change in all the σ values when moving from a 50 to 10 m resolution map. This is enforced by their respective mean and standard deviation values given in Table 3.2 which are all close to zero. This remains true going from 10 to 1 m resolution maps for σ_h and $\sigma_{\Delta h/\Delta x}$. Figure 3.7 on the other hand displays a noticeably greater scatter and is reflected by a mean difference an order of magnitude larger than seen in $\sigma_{\Delta h/\Delta x}$. The bigger spread compared to the values calculated using finite differencing show that there is more variance and the increase going to the 1 m resolution map is expected if information is preserved. It is at higher wavenumbers that the loss suffered when using finite differencing is most apparent which explains the tight spread in the lower plot of Figure 3.8.

The consistency across map resolutions for the spectrum derived parameters shows that, in contrast to the RIX values, the RMS parameters are less sensitive to the resolution of the input map. This characteristic could give some added flexibility to the to the user when performing site assessments. Indeed it also gives rise to the argument that the added value from using very fine maps may not necessarily be beneficial when considering the added computational cost.

		Mean	**Std**
50 & 10 m	σ_h	0.40	3.16
	$\sigma_{dh/dx}$	0.55	0.29
	$\sigma_{\Delta h/\Delta x}$	0.01	0.01
10 & 1 m	σ_h	-0.03	1.24
	$\sigma_{dh/dx}$	1.99	1.12
	$\sigma_{\Delta h/\Delta x}$	0.04	0.1

Table 3.2: Mean and standard deviation of the computed differences across σ_h, $\sigma_{dh/dx}$, and $\sigma_{\Delta h/\Delta x}$. The differences are calculated as 10m - 50m and 1m - 10m.

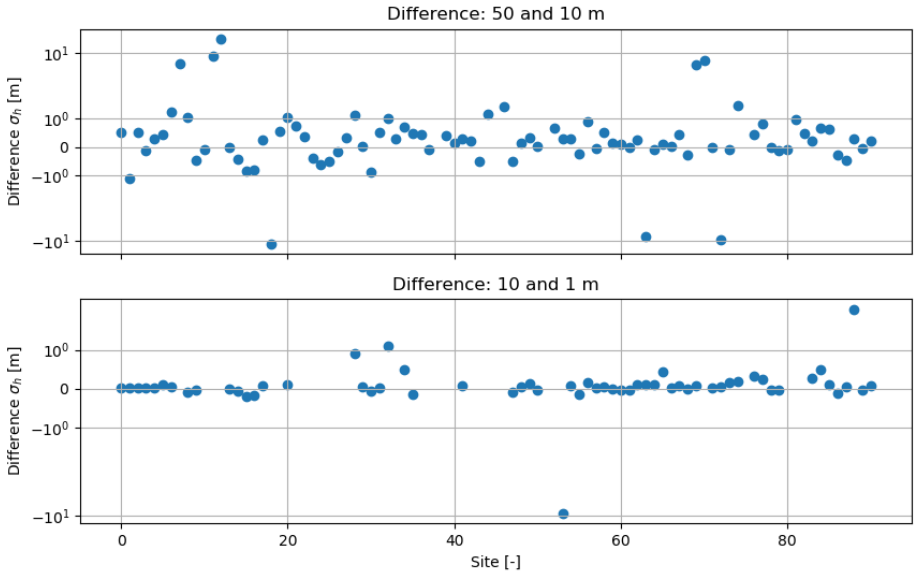

Figure 3.6: Difference in calculated σ_h values with differences computed as 10m - 50m and 1m - 10m. The x-axis is defined as the cumulative site number in chronological order. Y-axis is plotted in symmetric linear-log scaling.

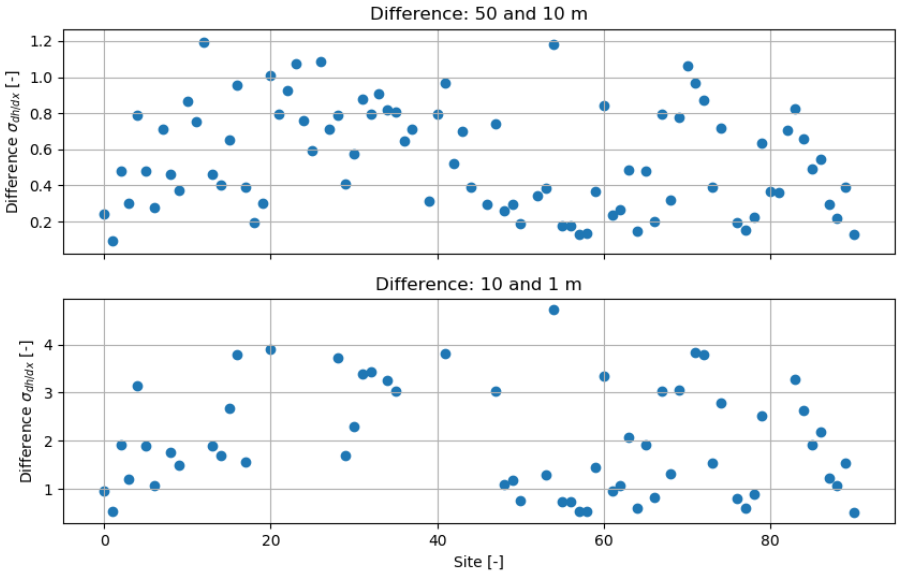

Figure 3.7: Difference in calculated $\sigma_{dh/dx}$ values with differences computed as 10m - 50m and 1m - 10m. The x-axis is defined as the cumulative site number in chronological order.

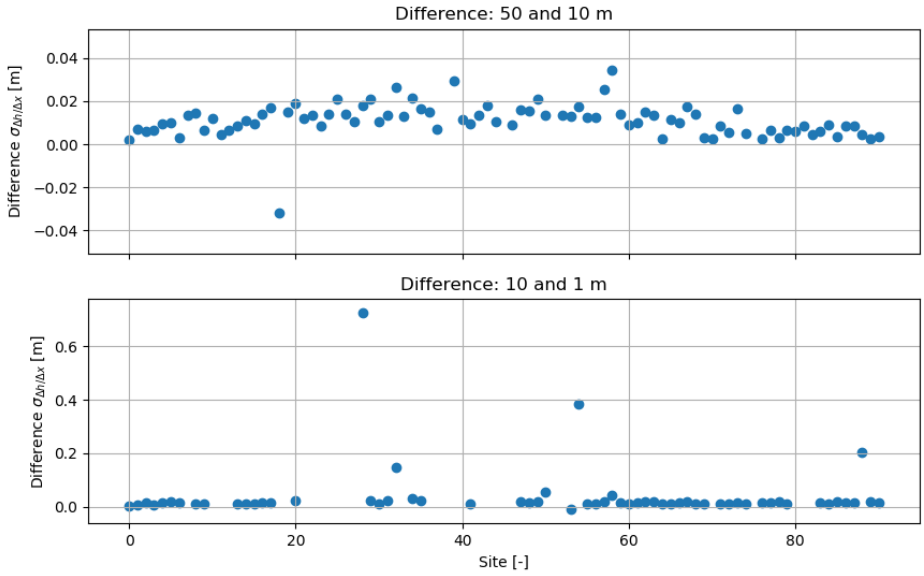

Figure 3.8: Difference in calculated $\sigma_{\Delta h/\Delta x}$ values with differences computed as 10m - 50m and 1m - 10m. The x-axis is defined as the cumulative site number in chronological order.

The terrain spectra from two sectors of Area 44, site 1 are plotted in Figures 3.9 and 3.10. The area and site were arbitrarily chosen and the two sectors correspond to directly West and North. The difference in the extents of the spectra for each resolution is a function of their resolution as shown by Equation (3.1) which describes the maximum resolvable wavenumber k_N according to the Nyquist-Shannon sampling theorem:

$$k_N = \frac{1}{2\Delta x} \tag{3.1}$$

where Δx is the map resolution. From both figures we see that the different spectra are indeed very similar as previously indicated. The largest difference was between the 50 & 10 m data and from the spectra we see that the 50 m plot deviates from the other two. The 10 & 1 m plots are almost identical for both sectors up until roughly $k = 0.02m^{-1}$, where the 10 m plot diverges slightly. From the spectra it is evident that the information gained from using the 1 m map is mostly limited to high values of k which have little effect on σ_h.

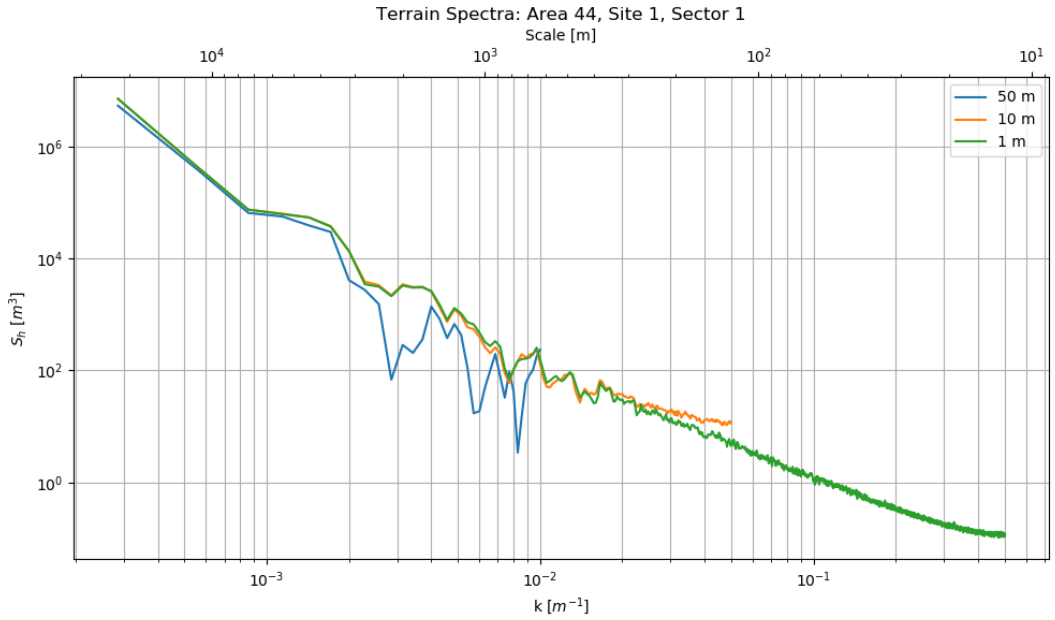

Figure 3.9: Terrain spectra of Area 44, Site 1, Sector 1 for all resolutions. Sector corresponds to 0° in Cartesian coordinates.

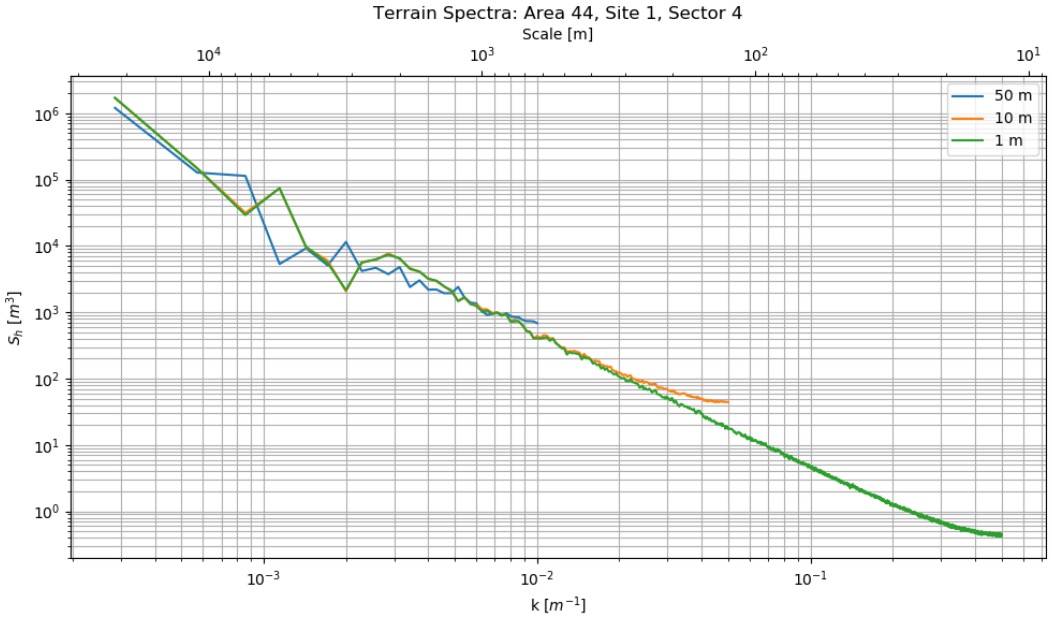

Figure 3.10: Terrain spectra of Area 44, Site 1, Sector 4 for all resolutions. Sector corresponds to 90° in Cartesian coordinates.

The terrain-slope spectra of the same sites are plotted below for both $k^2 S_h$ and $S_{\Delta h/\Delta x}$. Again the largest difference appears when going from 50 to 10 m resolution after which the 10 m PSD follows the 1 m PSD up until $k = 0.02m^{-1}$ where the two diverge. Most of the difference between the 10 & 1 m spectra is again at high wavenumbers which, as previously stated, have little effect on $\sigma_{\Delta h/\Delta x}$. More interesting is the difference between the PSD of $k^2 S_h$ and $S_{\Delta h/\Delta x}$. Comparing Figures 3.11 and 3.13 show that both the magnitudes of the y-axis as well as the spectral slopes differ greatly from each other. The difference between the magnitudes relates back to the truncation error associated with finite difference schemes resulting in a loss of variance. This loss is visualized by the two figures in that the variance can be calculated as the area under the curve of a spectrum which means that the variance of calculated from the finite difference will be less than that of the variance calculated from $k^2 S_h$. Similarly, the loss of variance becomes more prominent at higher wavenumbers where the small oscillations of the terrain are in essence smoothed out as shown by the negative slope of Figure 3.13. The flatter slope of Figure 3.11 indicates that the small scale oscillations of the terrain are still present in the data, and simple arithmetic can be used to show that the spectral slope of $k^2 S_h$ should be roughly equal to two plus the spectral slope of S_h due to the multiplication of k^2.

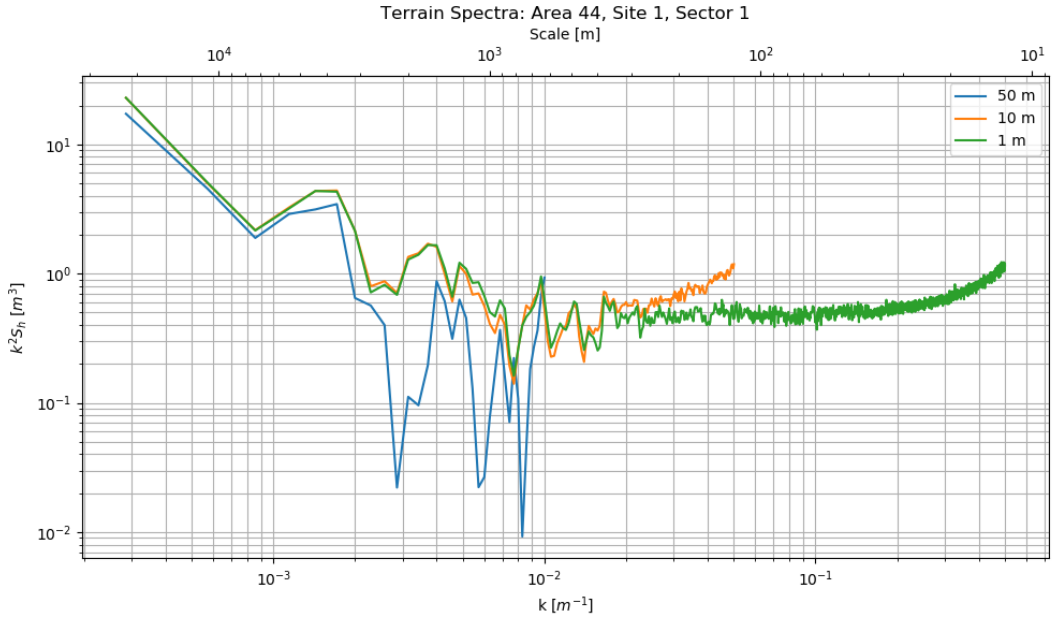

Figure 3.11: Terrain-slope spectra k^2S_h of Area 44, Site 1, Sector 1 for all resolutions. Sector corresponds to 0° in Cartesian coordinates.

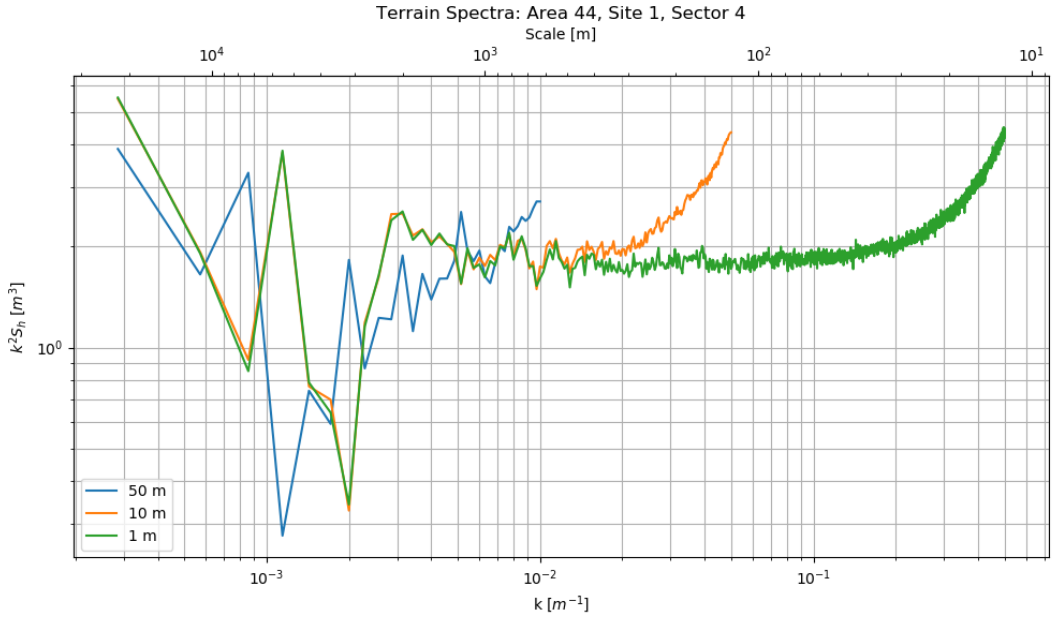

Figure 3.12: Terrain-slope spectra k^2S_h of Area 44, Site 1, Sector 4 in all resolutions. Sector corresponds to 90° in Cartesian coordinates.

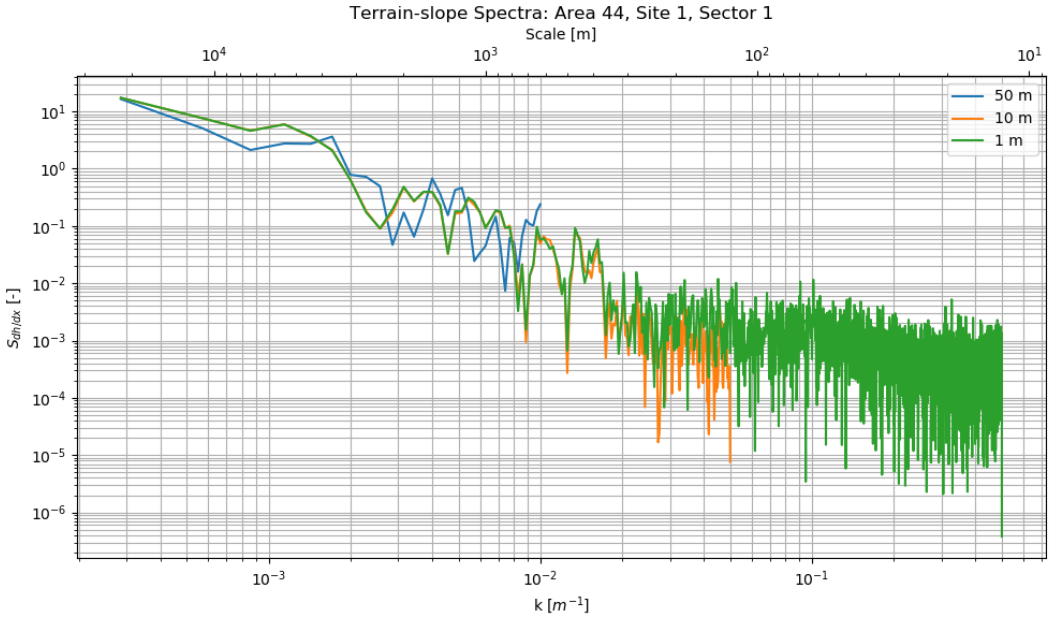

Figure 3.13: Terrain-slope spectra $S_{\Delta h/\Delta x}$ of Area 44, Site 1, Sector 1 in all resolutions. Sector corresponds to 0° in Cartesian coordinates.

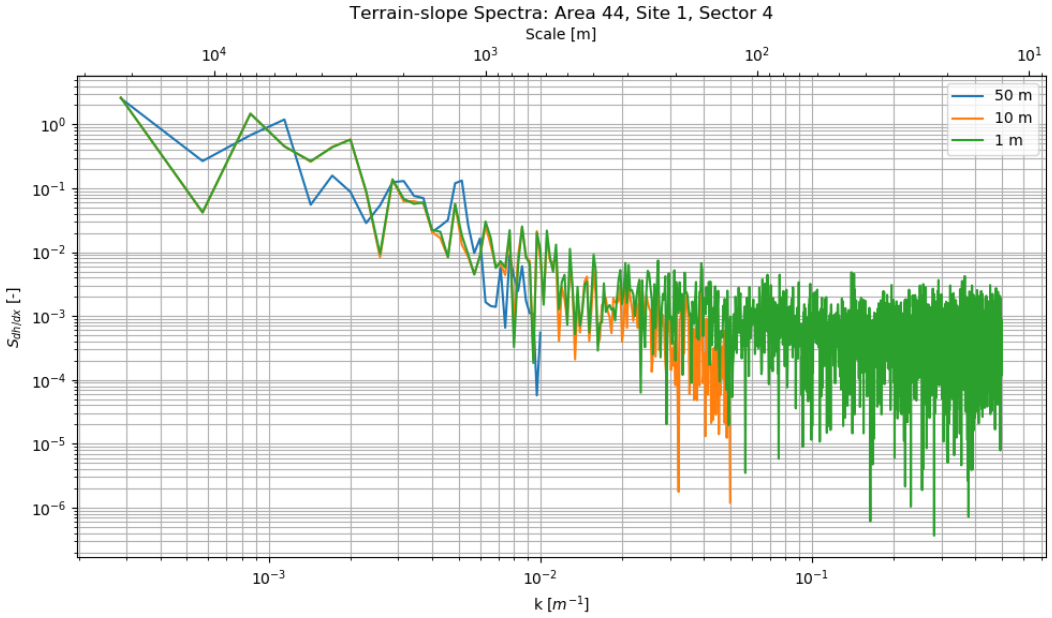

Figure 3.14: Terrain-slope spectra $S_{\Delta h/\Delta x}$ of Area 44, Site 1, Sector 4 in all resolutions. Sector corresponds to 90° in Cartesian coordinates.

3.1.4 Map Resolution Choice

Considering the effect of the input map resolution on the calculation of RIX, there may be a need to specify requirements to the input map to ensure that the ΔRIX correction factor is consistent. For the purposes of this report the 50 and 1 m maps will not be used to calculate any RIX values. The reason for also excluding the 50 m maps from being used is based on Section 2.2.1 which showed more coherence between the 10 m values calculated from WAsP and the the RIX routine.

Based on the calculated differences and spectra of the three resolutions it appears that there is value gained from 50 m to 10 m map resolution. The value gained from going to a 1 m map is, however, a bit more complicated. Considering the terrain spectra there is only a slight difference between the values calculated in Table 3.2 which is further backed up when looking at the PSD itself. The terrain-slope spectra must however, be considered by itself in this regard. Whilst the picture is the same for $S_{\Delta h/\Delta x}$ where there appears to be only a small difference, this is not true for $k^2 S_h$.

3.2 Relating Low-order Statistics to RIX

The success of RIX & ΔRIX in estimating and correcting for terrain ruggedness effects led to its wide implementation by the wind energy industry. Bridging the potentially more robust statistics derived from the spectra of the terrain can prove valuable by helping circumvent RIX's sensitivity to the map resolution allowing for a more consistent use of the ΔRIX correction factor. To achieve this the following section will attempt to define a relation to σ_h, $\sigma_{dh/dx}$, and $\sigma_{\Delta h/\Delta x}$.

To consolidate the low-order statistics with the omnidirectional RIX all the sectors will be averaged together to provide a site-averaged value. All statistics in this section are calculated using 10 m resolution map data.

Comparing σ_h to RIX in Figure 3.15 shows that quite a lot of scatter but that there is still some form of correlation, albeit not a strong one. Due to the large scatter it is difficult to determine the form of the relation. However, it will be assumed that the underlying relationship between the two variables is linear. Under this assumption the correlation coefficient R between σ_h and RIX is calculated using Pearson's correlation coefficient (PCC) which is defined as:

$$R_{X,Y} = \frac{\mathrm{cov}(X,Y)}{\sigma_X \sigma_Y} \tag{3.2}$$

The value of R is calculated to be 0.61 indicating a moderate positive linear relationship.

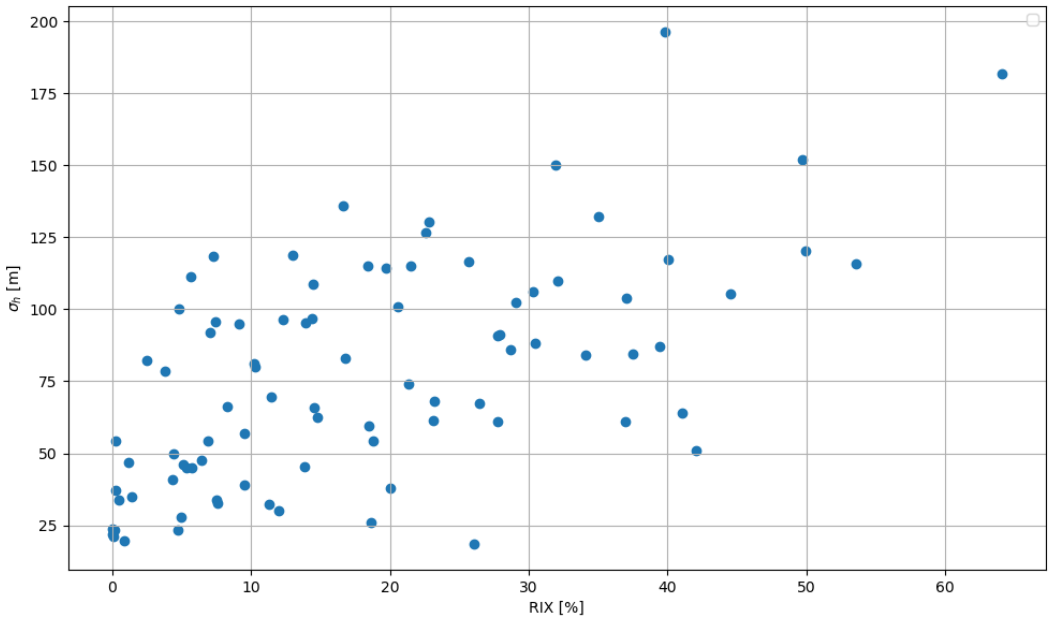

Figure 3.15: Site-averaged σ_h vs. RIX with filtered data set.

Calculating the line of best fit results in the equation $y = 1.6x + 47.93$. Additionally, a crude relation formulated by Kelly (2016) , can be used to relate RIX as a percentage to σ_h for a range of complex-to-moderate terrain types:

$$RIX \approx a_R \ln\left(1 + \frac{\sigma_h}{\Delta Z_{ref}}\right) \tag{3.3}$$

where the constant a_R ~30 and ΔZ_{ref} ~100 m. Plotting the two functions results in two distinctly different curves that intersect the scattered data. By simple visual inspection it appears that either curve can be said to give a reasonable mean value, though due to the large spread of the data points any mean value would not be adequately representative. Changing to a logarithmic plot shows the strength of the RIX relation above. Figure 3.17 clearly shows that Equation (3.3) is stronger representation of the mean for the majority of the sites with RIX values above 4% compared to the linear relation.

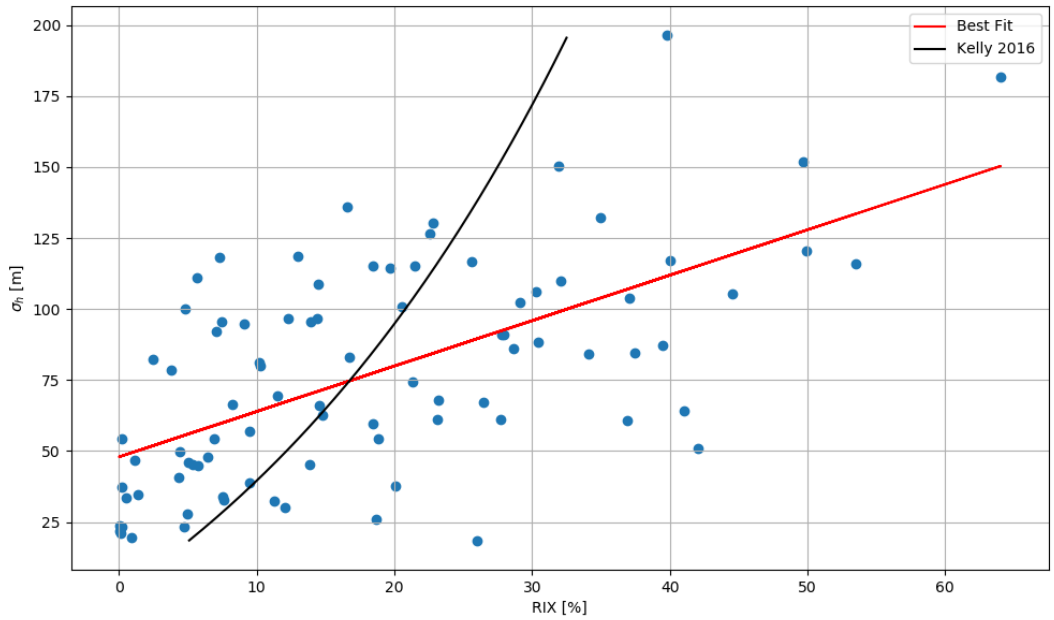

Figure 3.16: Site-averaged σ_h vs. RIX with filtered data set. Also plotted is the line of best fit $y = 1.6x + 47.93$ and RIX relation formulated in Equation (3.3).

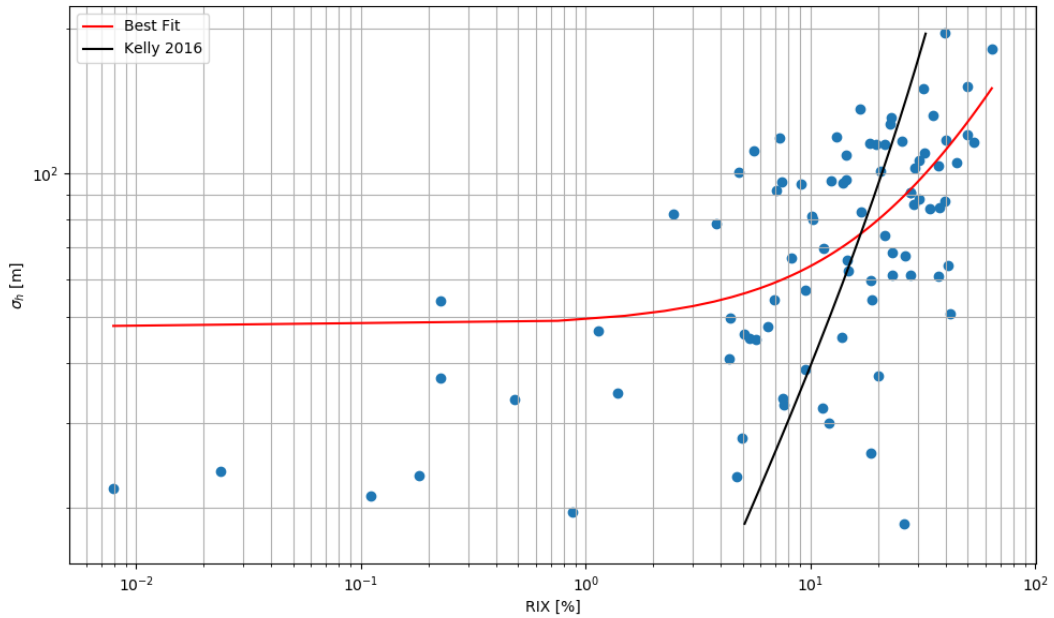

Figure 3.17: Site-averaged σ_h vs. RIX with filtered data set in logarithmic scale. Also plotted is the line of best fit $y = 1.6x + 47.93$ and RIX relation formulated in Equation (3.3).

As with the relation above, Figure 3.18 also has a large scatter with some form of

positive relationship using the same logic. Calculating the PCC results in a correlation coefficient R = 0.41, meaning that there is a weak positive linear relationship.

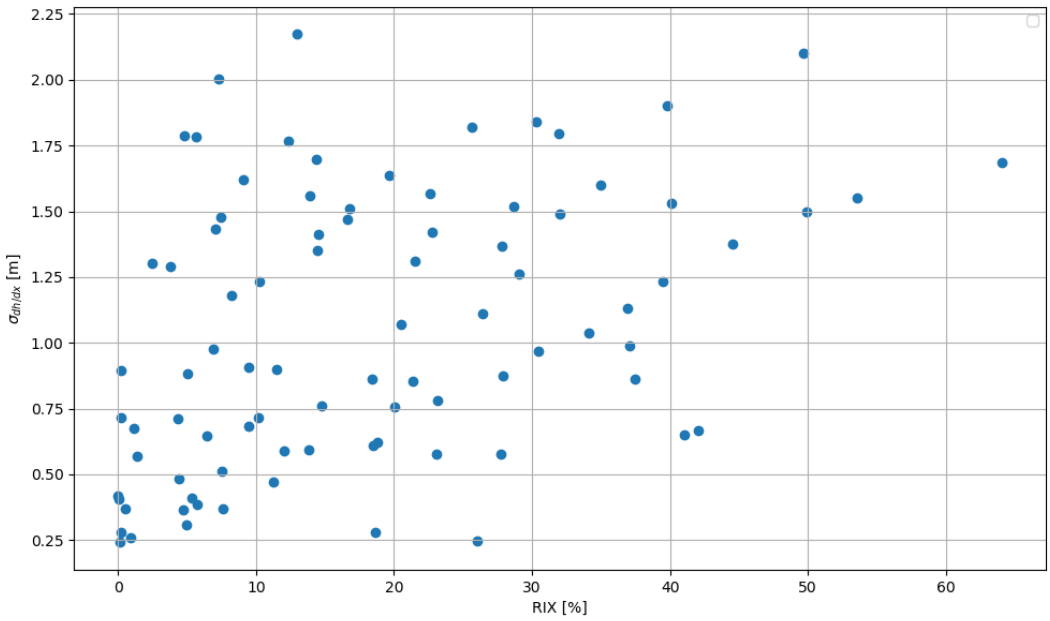

Figure 3.18: Site-averaged $\sigma_{dh/dx}$ vs. RIX with filtered data set.

Adjusting the plot to a logarithmic scale in expectedly resembles Figure 3.17. Adjusting the RIX relation formulated by Kelly (2016) to fit the data points gives the following expression:

$$RIX \approx a_R \ln\left(1 + \sigma_{dh/dx}\right) \tag{3.4}$$

The adjusted RIX relation upon visual inspection appears to have a similar performance in providing an estimate for the mean value for RIX values above 4%.

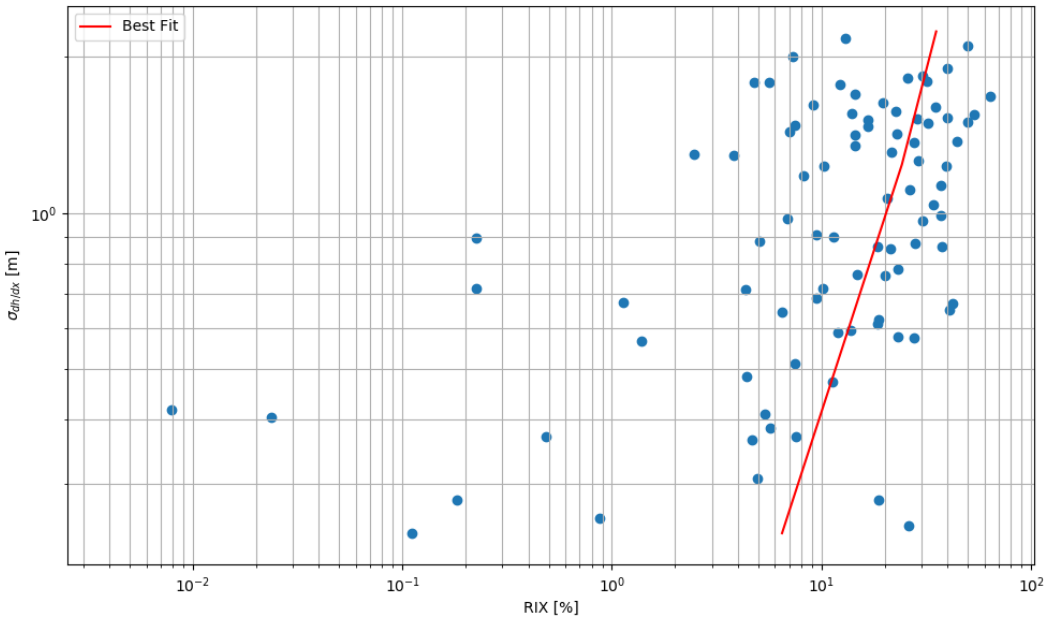

Figure 3.19: Site-averaged $\sigma_{dh/dx}$ vs. RIX with filtered data set in logarithmic scale. Also plotted is the RIX relation formulated in Equation (3.4).

As has been discussed the method of calculating the terrain-slope spectra using finite differencing results in a loss of variance. Similarly, the RIX method also uses finite difference schemes to calculate the slopes. It is therefore not too surprising that Figure 3.20 appears to show a strong non-linear correlation between the two metrics. The data points keep a tight spread up till a RIX value of roughly 10%, past which the spread increases. It is also past this point that the two metrics take on a linear relationship.

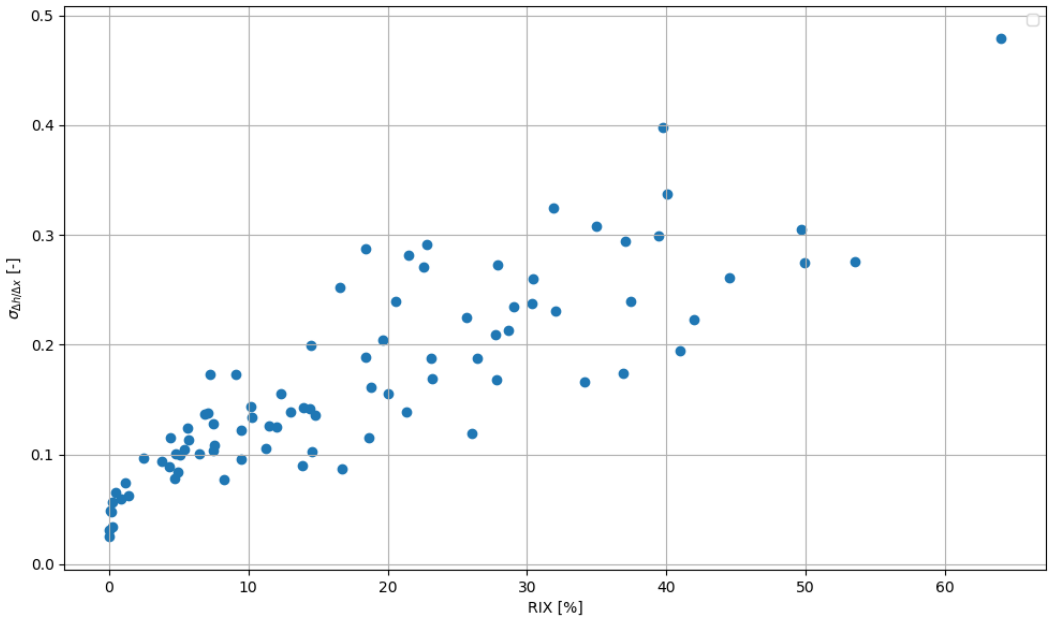

Figure 3.20: Site-averaged $\sigma_{\Delta h/\Delta x}$ vs. RIX with filtered data set.

The relation itself appears to be a form of exponential function and so the linearity assumption required to use PCC does not hold up. Instead, Spearman's rank correlation coefficient is used. Also known as Spearman's ρ, it differs from PCC by instead assessing monotonic relationships regardless of linearity. Spearman's ρ is described by:

$$r_s = \frac{\mathrm{cov}\left(\mathrm{rg}_X, \mathrm{rg}_Y\right)}{\sigma_{\mathrm{rg}_X}\sigma_{\mathrm{rg}}} \tag{3.5}$$

where $rg_{x,y}$ are the rank variables converted from X & Y. Using Spearman's ρ the correlation coefficient of $\sigma_{\Delta h/\Delta x}$ and RIX is 0.88, indicating a strong positive correlation. Based on the shape formed by the data points compared with basic function shapes the line of best fit was found as a composite function consisting of a linear component and a exponential component:

$$f(x) \approx C_0 + C_1 x - C_2 e^{-C_3 x} \tag{3.6}$$

where the constants $C_0 = 0.0854$, $C_1 = 0.0048$, $C_2 = 0.0462$, and $C_3 = 0.5$. The line of best fit is plotted with the data in Figures 3.21 and 3.22, the latter being in logarithmic scale. From these it is clear that Equation (3.6) provides strong representative mean value.

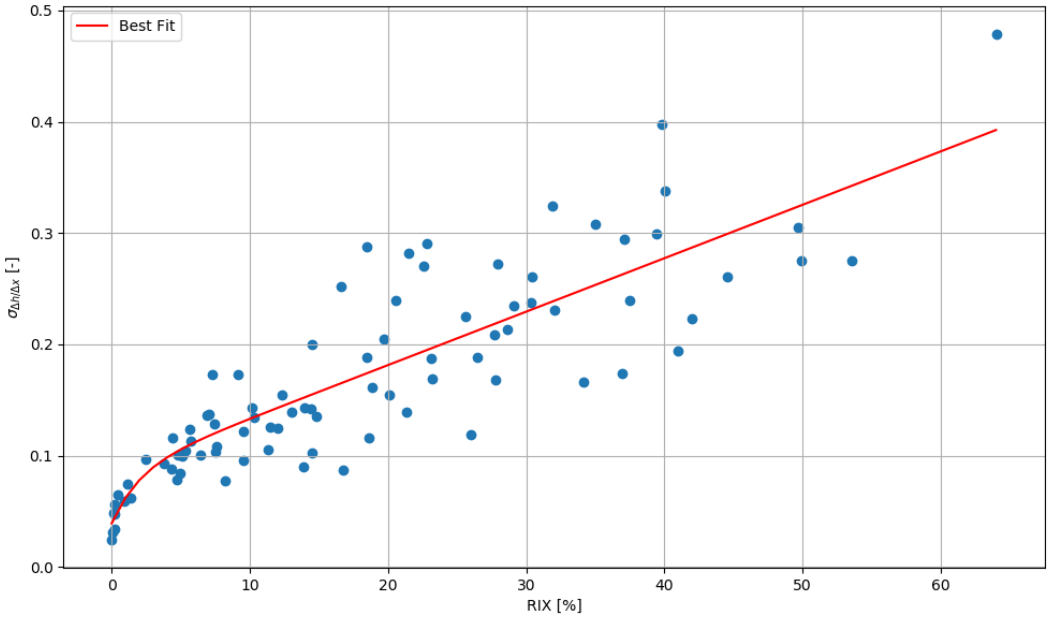

Figure 3.21: Site-averaged $\sigma_{\Delta h/\Delta x}$ vs. RIX with filtered data set.

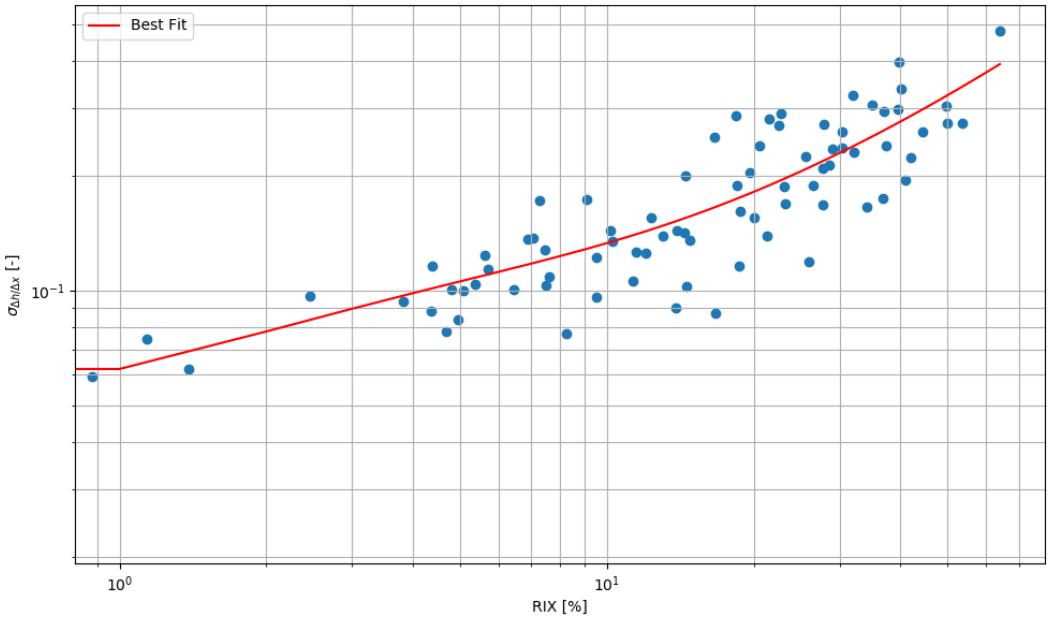

Figure 3.22: Site-averaged $\sigma_{\Delta h/\Delta x}$ vs. RIX with filtered data set in logarithmic scale.

The importance of bridging the low-order statistics derived from the spectrum of the terrain with the RIX method lies in the furtherment of the method for use in wind energy and ultimately providing an improvement to the current standard. The loss of variance that is inherent to the finite differencing method provides what is seemingly an

important point of commonality to the RIX method. Based on the presented correlation coefficients and the formulated functions there is a strong argument in favor of using this method when attempting to relate to RIX and to further develop the formulation given in Equation (3.6).

3.3 A Directional Metric

As shown the low-order statistics provide a promising avenue in which to circumvent RIX's sensitivity to the input map resolution. However, they were calculated as site-averaged omnidirectional values to allow for comparison with RIX, but from the discussion in Section 1.1.2.2 it is expected that wind direction should heavily influence the measurements. And indeed if it is assumed that the low-order statistics such as σ_h can be related to the wind speed then it is also assumed that wind direction must be accounted for. By simply adding error bars to the σ_h vs. RIX plot it is apparent that the variability of σ_h is of the same magnitude as the value itself.

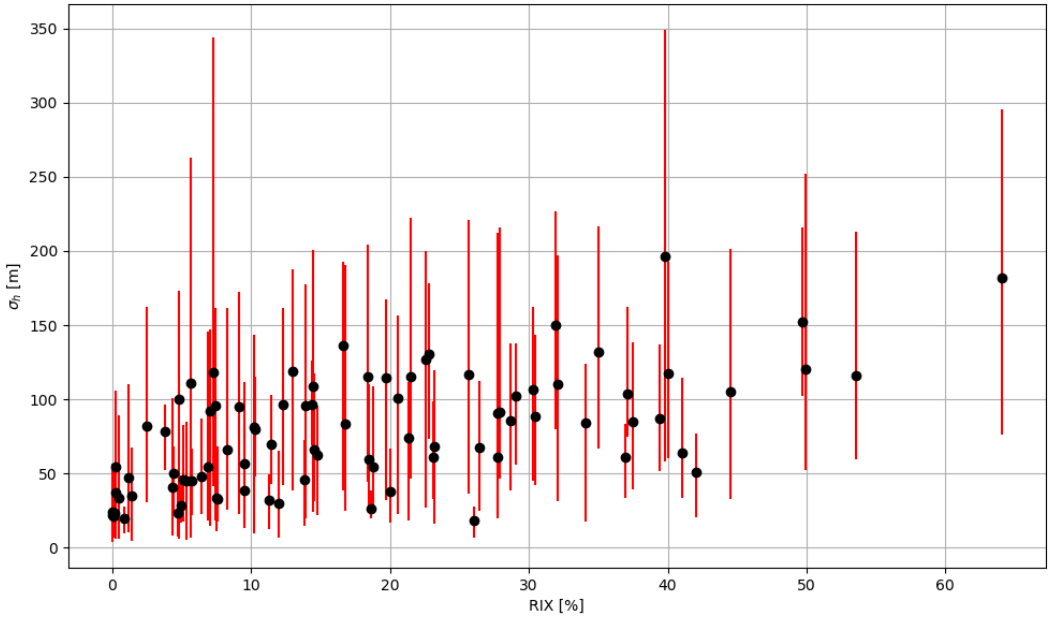

Figure 3.23: Site-averaged σ_h with error bars vs. RIX using filtered data set. Red ('error') bars indicate the maximum and minimum σ_h value calculated at a site.

This section will investigate the potential for including the directionality of the wind by using sector-averaged values of the low-order statistics. To do this the speed-up factor calculated by the IBZ model of WAsP will be compared to that of WAsP-CFD which are Reynolds number independent. For further information on WAsP-CFD the reader is directed to Bechmann; Cavar et al. (2017, 2016) . The reader is reminded that the speed-up ratio was previously defined in Equation (1.4). Comparisons using the difference

between these two parameters should be equal to the prediction error between the IBZ model and the RANS model.

For the analysis 7 sites in Area 56 were selected due to their relatively close proximity to each other. The sites in question are sites 5 through 11 as defined by Table A.2 and presented below. The input map is obtained from the GeoTIFF files previously used with a single uniform roughness applied to the entire region with a value of 0.03 m.

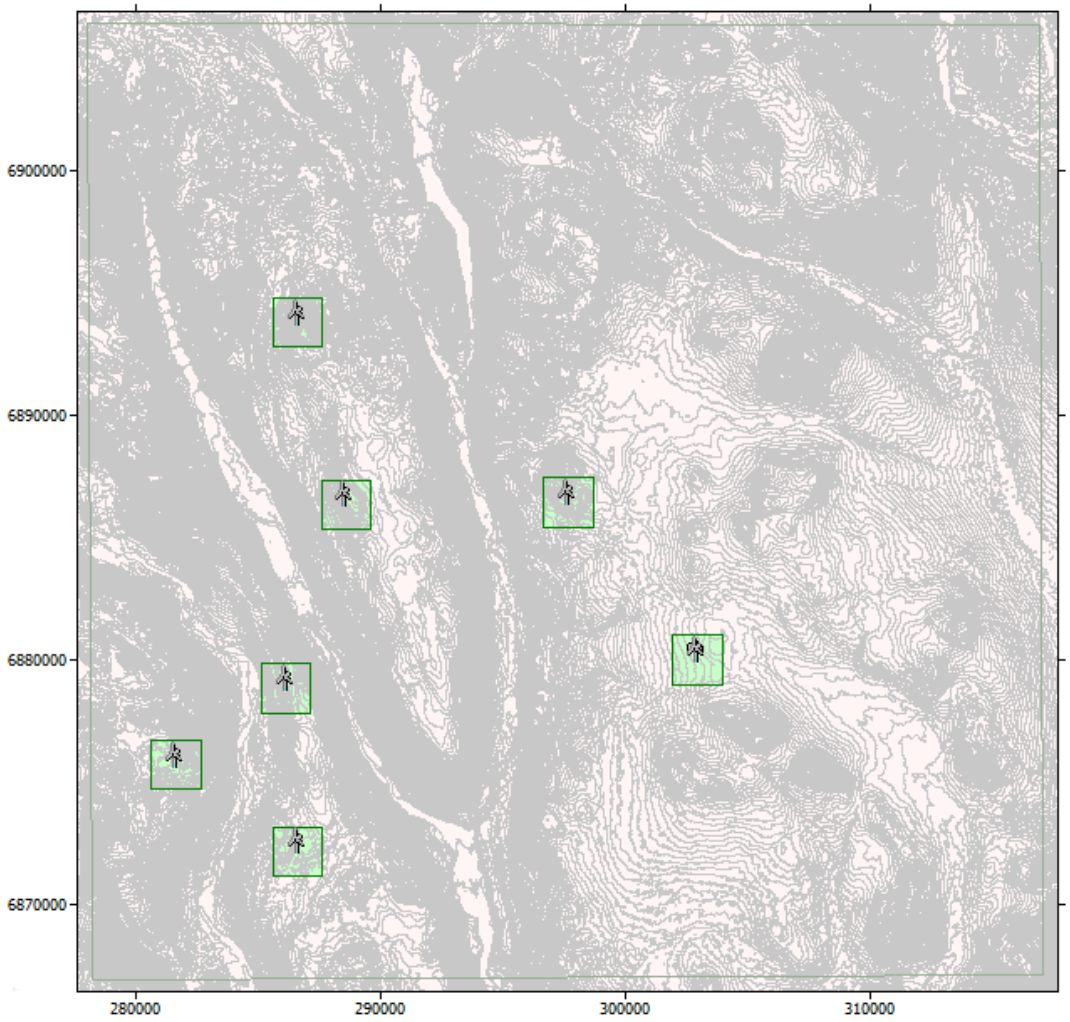

Figure 3.24: WAsP-CFD map of Area 56 and sites 5 through 11 with RANS tiles centered about the site location.

3.3.1 Relation to Speed-up Factor

This subsection will investigate multiple statistics and their relation to ΔS calculated from WAsP and WAsP-CFD. This is done at altitudes of 50, 100, and 200 m above ground level (AGL). The reason for this is that different scales of topographic features affect, with changing strength, different regions of the ABL. That is not to say changes in the effective surface roughness do not propagate through the entire ABL, but instead

that the 'noise' from small scale features is less noticeable at higher altitudes, potentially allowing relations to form. All plots at all altitudes pertaining to this analysis can be found in Appendix B.

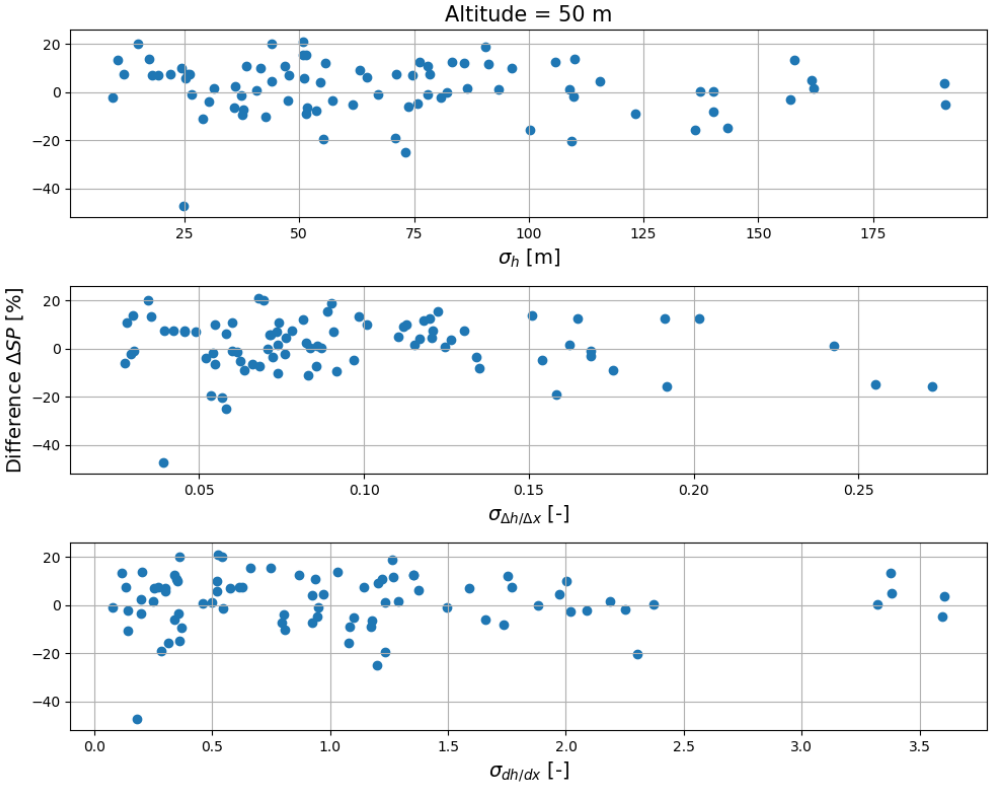

Figure 3.25: Difference between the WAsP-IBZ and WAsP-CFD calculated ΔS values plotted against multiple low-order statistics at an altitude of 50 m. Difference computed as IBZ minus CFD value.

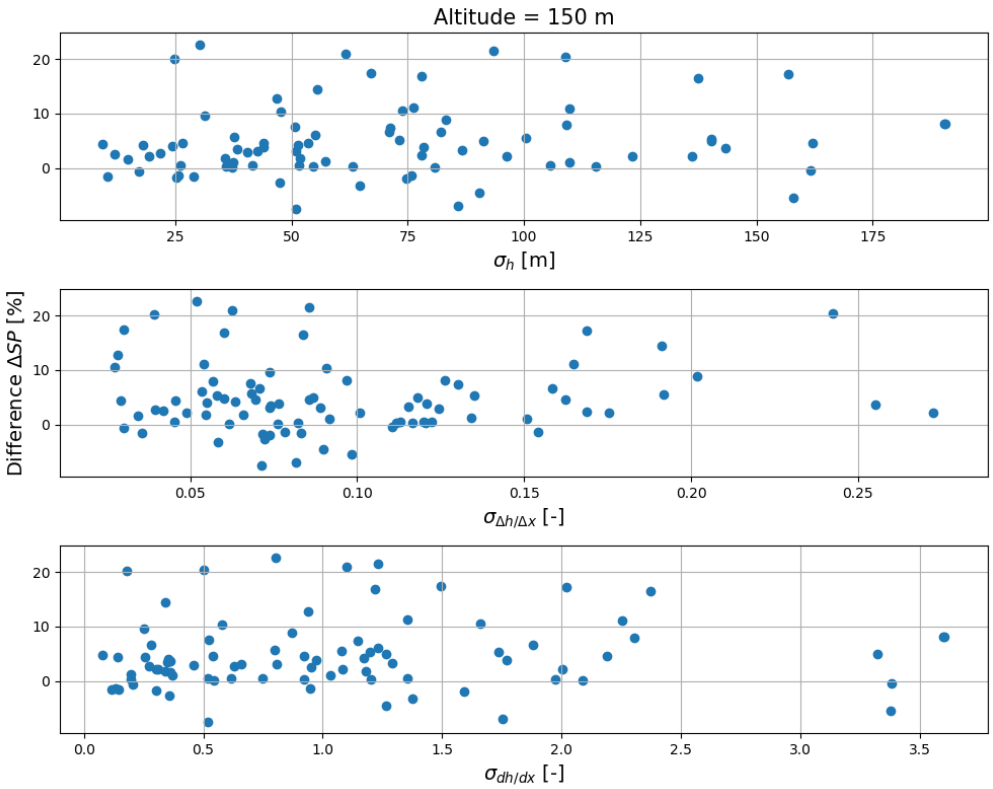

Figure 3.26: Difference between the WAsP-IBZ and WAsP-CFD calculated ΔS values plotted against multiple low-order statistics at an altitude of 150 m. Difference computed as IBZ minus CFD value.

First, the previously used low-order statistics are shown in Figures 3.25 and 3.26. Through visual inspection there are no apparent relations to the difference in speed-up factor and calculations of the PCC indeed show a negligible value for all three statistics ranging from roughly 0.0–0.15. Expanding the investigation further the same statistics are calculated using only the portions of the terrain with a positive slope moving towards the site, henceforth referred to as the upslope. The reason for looking at the upslope version of the parameters comes from Beljaars et al. (2004) using the parameterization developed by Wood and Mason (1993) for the effective roughness length. Inherent in the formulation is the frontal area silhouette, or apparent area, which was interpreted by Kelly et al. (2019) as the upslopes. In terms of data manipulation the upslopes are found using finite differencing and zeroing out all other values.

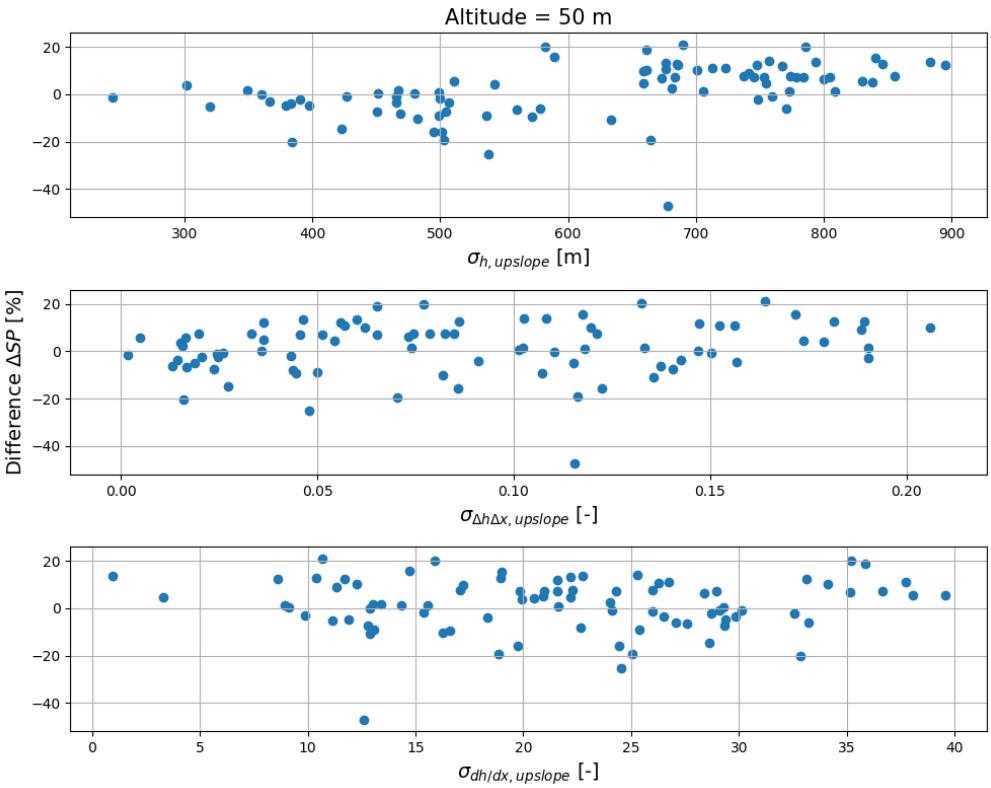

Figure 3.27: Difference between the WAsP-IBZ and WAsP-CFD calculated ΔS ('fractional speed-up') values plotted against the upslope only low-order statistics at an altitude of 50 m.

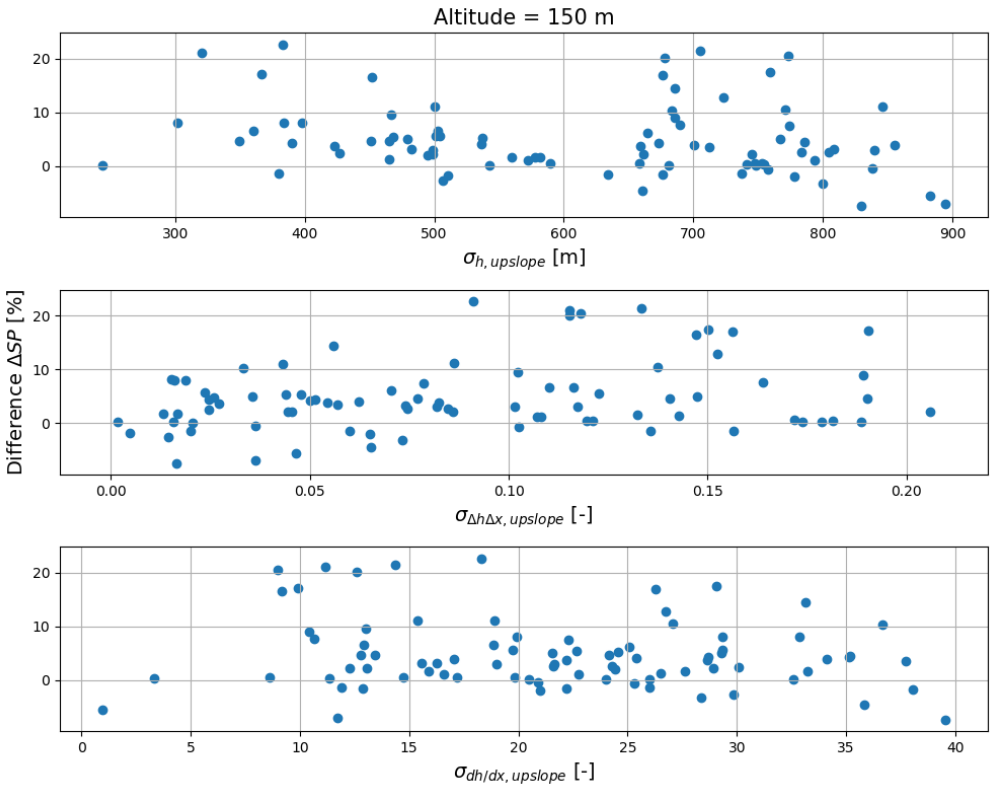

Figure 3.28: Difference between the WAsP-IBZ and WAsP-CFD calculated ΔS ('fractional speed-up') values plotted against the upslope only low-order statistics at an altitude of 150 m.

Figures 3.27 and 3.28 plot the relations found at 50 and 150 m altitude whilst the remaining altitudes can be viewed in Figures B.5 to B.8. Similar to the standard statistics the upslope versions do not indicate any correlation with the largest PCC value being 0.29 for $\sigma_{\Delta h/\Delta x,upslope}$ at 50 m altitude. The same analysis is performed on the mean slope and the skewness of the slopes and are shown in Figures B.9 to B.12. The mean upslope is also included in these figures. Again there is little to no correlation at any altitude between these statistics and the difference in ΔS. As with the previous statistics looked at in this section the different altitudes do not yield any statistically improved correlation coefficients.

The same investigation was completed for other variations of the y-axis including; ΔS of the RANS and IBZ model separately as well as their ratio. The figures pertaining to this are not included in this report, however, of all the iterations it was ΔS vs. $\sigma_{h,upslope}$ that returned the highest correlation coefficient indicating a moderate positive correlation to the RANS speed-up. However, further research is required to see if $\sigma_{h,upslope}$ can be useful as a sector-wise metric. Interestingly, the largest PCC was found at an altitude of 200 m and the lowest at 50 m. Expanding on this it is known that at higher altitudes a site 'sees' more of the terrain whilst at lower altitudes the local terrain is emphasized. It may therefore be possible to use these two metrics to determine, for the standard

altitudes in wind power meteorology, the optimal radius to calculate $\sigma_{h,upslope}$ at.

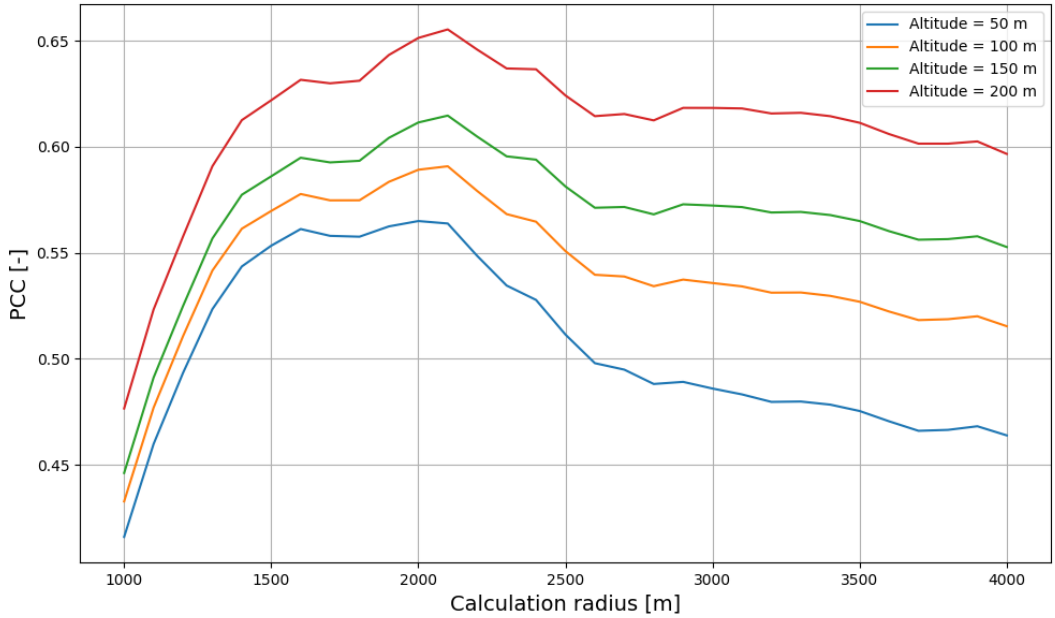

Figure 3.29: Pearson's correlation coefficient ('PCC') of ΔS ('fractional speed-up') and $\sigma_{h,upslope}$ at a range of calculation radii and multiple altitudes.

Using a radius of 1000–4000 m the sector-averaged $\sigma_{h,upslope}$ is calculated using the filtered sites and used to calculate the Pearson's correlation coefficient with ΔS. The reader is reminded that the site is located at the center of the WAsP-CFD tile and that a 1000 m calculation radius corresponds to the length upwind within the tile. Interestingly there appears to be a very similar shape and shape distribution across the four altitudes the peak PCC occurring at roughly the same calculation radius of roughly 2100 m. Post-peak all four curves decrease in a similar manner. Disregarding the peak and focusing on the curve; if the curve was smoothed out the resulting peak would indicate that there is a slight shift towards larger calculation radii at higher altitudes. This shift would at best in the order of 100–200 m and is unexpectedly small. Considering the method of calculation it should be noted that WAsP-CFD calculates in 2x2 km tiles, as shown by the green squares in Figure 3.24, which may be insufficient when comparing to a $\sigma_{h,upslope}$ calculated using 3500 m radius. A workaround for this limitation could be using the 'Ellypsis' RANS solver seperate from WAsP-CFD giving the freedom to alter the calculation domain. However, due to time constraints the further investigation this potential correlation remains incomplete.

CHAPTER 4

Conclusions and Recommendations

As onshore wind energy continues to develop and more countries invest, an increasing amount of developments will be at sites outside the operational envelope of the commonly used linearized models. The ΔRIX correction factor and WAsP-CFD were developed in response to this trend where the RANS solver offers the most physically 'correct' modelling path. However, due to its large computational cost there is a clear motivation to continuously improve the linearized models such that only the most complex sites require a RANS simulation. As discussed in the literature review there is a lack of physicality behind RIX and that the use of low-order statistics derived from the terrain may offer viable alternative. Additionally, the terrain statistics can potentially be further developed towards a directional metric as opposed to the current omnidirectional one.

Section 4.1 will summarize and offer a conclusion to the work presented in this report. Section 4.2 will then critically look at the method used and offer recommendations for future work and possible avenues to be pursued to improve the correlations presented.

4.1 Conclusions

In this project low-order statistics derived from the surrounding terrain of specific sites were used to develop a correlation to the sites RIX value. This was done exclusively at Norwegian sites partly because of the large amount of easily accessible data from Kartverket at 50, 10, and 1 m resolutions. Additionally, the chosen sites were in regions recommended by Jakobsen et al. (2019) to be most suitable for onshore wind developments in Norway and offered regions ranging from flat to highly complex mountainous terrain. The statistics were calculated according to the method described in Jacobs et al. (2017) using 1-D signals averaged radially in a wedge shaped area to return a pseudo 2-D signal. The dimensions of the wedge were chosen to fit with previous standards in wind power meteorology where a sector covers 30°, for a total of 12 sectors. The radius was chosen as the default radius used by WAsP when calculating the local RIX value. In the analyses relating to RIX the sector-averaged statistics were further averaged such that the site mean was obtained. This was done because RIX is a omnidirectional metric and so sector-averaged comparisons would be nonsensical.

Using PSD to calculate the low-order statistics is the only method to directly calculate the standard deviation of the derivatives (slope) without the use of finite differencing and the associated truncation errors. Furthermore, spectral analyses make other statistics easily calculable, such as the spectral slopes, and give an informative visualisation of the

differences between sites and sectors as well as across map resolutions.

The verification of the RIX algorithm showed that, in both the self-made algorithm and WAsP, the metric was seemingly sensitive to the map resolution. These results were further expanded using the self-made RIX algorithm finding that the local RIX value increases with finer map resolutions. However, an increased RIX value is not an issue in itself since the ΔRIX correction factor uses the difference between two sites. The main issue is that the standard deviation of these differences is roughly the same magnitude of the calculated differences and also increases with finer map resolution which means that both the site orography and the map resolution would strongly influence the correction factor. Based on this there may be a need to specify requirements to the input map to ensure consistency when using ΔRIX. In contrast σ_h and $\sigma_{\Delta h/\Delta x}$ were shown to be largely independent of the map resolution whilst $\sigma_{dh/dx}$ had a little bit more variance.

Investigations of a RIX relation was done by attempting to correlate the low-order statistics and RIX at a resolution of 10 m. Previous work done by Kelly (2016) where a crude relation was formulated between σ_h and RIX was corroborated showing a moderate ability to represent the mean for RIX values above 4%. However, a much stronger correlation was achieved using $\sigma_{\Delta h/\Delta x}$ with a Spearman's ρ of 0.88. This metric provides a further commonality to RIX in the use of the same finite difference scheme to compute the slopes and thus suffering the same loss of variance inherent to finite differencing. The new function created to describe this correlation, Equation (3.6), shows a much higher skill of representing the mean RIX values across a wider range as compared to the earlier formulation by Kelly (2016) and can be used as a method to circumvent RIX's sensitivity to the map resolution. In terms of its applicability to industry this new correlation expands the usefulness of ΔRIX as a correction factor by allowing developers to use modern fine resolution maps without issue. Additionally, the correlation to RIX also proves a correlation to the speed-up factor RIX was validated against which is often used by developers in the wind prospecting phase to find regions of interest.

Further attempts to expand the use of the terrain statistics towards a directional metric by correlating with sector-wise values of the speed-up, calculated using WAsP and WAsP-CFD, yielded no correlations strong enough to pursue with the exception of $\sigma_{h,upslope}$ with a correlation of roughly 0.65 at the highest point. The strength of this metric is due to its asymmetry, seeing only the upslope, and is entirely different than the method behind RIX which considers all slopes larger than the critical slope value. It shows that, for a given wind direction, the terrain 'seen' by the site in terms of the wind speed requires different new approaches and that asymmetrical metrics, such as $\sigma_{h,upslope}$, are an important step towards sector-wise correlations. Unfortunately, due to time limitations further investigations of this could not be explored.

Remembering the research objective it is concluded that low-order statistics can be strongly correlated to RIX and that terrain complexity characterization using these metrics provide a strong alternative, independent of map resolution, to be used by the wind power industry as the next orographic performance indicator and correction factor. Their skill as a directional metric using sector-wise values is yet to be determined though preliminary results indicate that $\sigma_{h,upslope}$ may be the strongest alternative. Beyond its use in terrain ruggedness characterization, the work done by Anderson and Meneveau

(2011) and Kelly et al. (2019) indicate that the metrics obtained from the terrain spectrum hold promise towards estimating important parameters, such as the effective roughness length, and familiarization with these statistics would mean a step in the right direction for the wind energy industry.

4.2 Recommendations

The results presented in this report are not infallible and therefore this section will address the identified shortcomings and recommendations for further research.

First, the findings related to RIX were obtained using a self-made RIX routine. Though this routine follows the same method as the RIX calculator in WAsP, it is not an exact replica and yields different values for the same area. As previously stated it is a result of the difference in the map format where WAsP uses vector maps whilst the results of this report are based on raster maps. Additionally, the slopes in WAsP are calculated using both a cubic spline and first-order forward differencing scheme whilst the self-made routine only uses first-order forward differencing with backward differencing at the last point. In total the relations that were found between RIX and the low-order statistics should be verified using a large sample of RIX values calculated in WAsP.

Second, the calculation parameters used when comparing RIX and the low-order statistics were set as the default values used in WAsP. This was done to limit the degrees of freedom in the analyses while using the values most likely to be used by the average user, but these values are likely not the optimal values. An example of this is that Mortensen et al. (2006) found that a critical slope of 0.45 gave the maximum coefficient of determination R^2. Therefore it is recommended to further improve the relations presented in this report by tuning the calculation parameters.

Third, the new correlation using $\sigma_{\Delta h/\Delta x}$ can be used extend the usefulness of RIX. However, it is recommended that research is put into validating this new terrain metric as a ruggedness characterization method directly as was previously done with RIX. Further research could offer improvements to resource assessment modelling, thereby improving AEP estimations for new wind developments.

Fourth, the investigation into the potential of the terrain statistics potential to be developed into a sector-wise metric was stunted due to time constraints. However, one of the metrics showed moderate potential and it is recommended that further research be done on asymmetric stats such as $\sigma_{h,upslope}$.

And last, all the analyses made in this report was done using DEM's obtained from Kartverket. Such maps contain only the terrain itself, excluding all surface features such as trees, boulders, and buildings. In addition to this data Kartverket also offers DSM's at the same resolutions for the same sites used in this report. These maps would include all surface features which presents a unique opportunity to investigate how the use of DEM's or DSM's affect the terrain statistics and whether the inclusion of surface features might be better for ruggedness characterization.

APPENDIX A

Areas-of-Interest

Below are tables containing the coordinates of all sites used in the data analysis as well as annotated figures showing the each area and the corresponding sites.

	Area 44		**Area 45**		**Area 49**		**Area 50**	
Site	X	Y	X	Y	X	Y	X	Y
1	861,445	7,887,003	377,825	7,209,525	-15,510	6,830,740	-22,636	6,795,603
2	870,471	7,874,895	387,272	7,195,960	3,803	6,832,081	-29,008	6,793,020
3	849,825	7,855,310	349,281	7,175,635	18,175	6,826,842	-15,700	6,794,873
4	867,227	7,843,745	332,237	7,131,696			-6,828	6,801,731
5			387,066	7,137,234			-5,456	6,795,840
6			381,932	7,124,700			7,602	6,796,582
7							1,228	6,788,363
8							-12,120	6,777,890
9							13,658	6,794,716
10							13,901	6,789,632
11							7,932	6,787,050
12							13,739	6,782,530
13							6,158	6,783,171
14							3,496	6,780,437
15							9,303	6,776,641
16							-5,456	6,777,291
17							-19,088	6,778,015

Table A.1: Areas 44-50 used in this report. The coordinates are presented in WGS 84 / UTM zone 33N. Red cells indicate that there is missing data at these locations in the 1 m resolution map. Yellow cells indicate that there is inconsistent elevation data between map resolutions at these locations. Orange cells are a combination of these two.

	Area 51		Area 52		Area 53		Area 54		Area 56	
Site	X	Y	X	Y	X	Y	X	Y	X	Y
1	-36,072	6,676,501	8,004	6,561,880	141,422	6,539,859	186,556	6,614,390	324,862	6,875,493
2	-9,959	6,672,063	-4,522	6,545,665	119,197	6,580,193	203,253	6,613,906	231,540	6,887,417
3	9,419	6,687,501	12,317	6,540,733	109,594	6,556,862	216,561	6,611,733	313,723	6,875,585
4	25,514	6,684,702	20,736	6,528,206	106,027	6,520,376	194,864	6,607,051	302,780	6,866,988
5	20,094	6,672,726	31,620	6,523,690	95,600	6,505,284	183,008	6,597,694	302,975	6,879,981
6	5,393	6,672,883	26,281	6,495,351	112,338	6,492,112	200,510	6,596,568	297,699	6,886,430
7	18,012	6,653,497	71,664	6,487,754	103,832	6,477,576	208,495	6,594,552	286,657	6,872,166
8	25,350	6,665,661	66,530	6,524,922			204,866	6,591,320	286,169	6,878,815
9	17,631	6,684,545					218,819	6,596,241	281,674	6,875,683
10	30,015	6,609,790					176,908	6,603,591	288,612	6,886,335
11	13,197	6,655,152					195,181	6,587,600	286,657	6,893,761
12	-24,083	6,638,722					184,459	6,585,039	313,780	6,917,292
13	-1,091	6,635,930					210,843	6,607,531	291,445	6,907,530
14	10,405	6,615,734					193,251	6,583,503	309,913	6,910,471
15							211,963	6,587,618	324,667	6,895,520
16									321,052	6,888,480
17									327,891	6,885,264

Table A.2: Areas 51-56 used in this report. The coordinates are presented in WGS 84 / UTM zone 33N. Red cells indicate that there is missing data at these locations in the 1 m resolution map. Yellow cells indicate that there is inconsistent elevation data between map resolutions at these locations. Orange cells are a combination of these two.

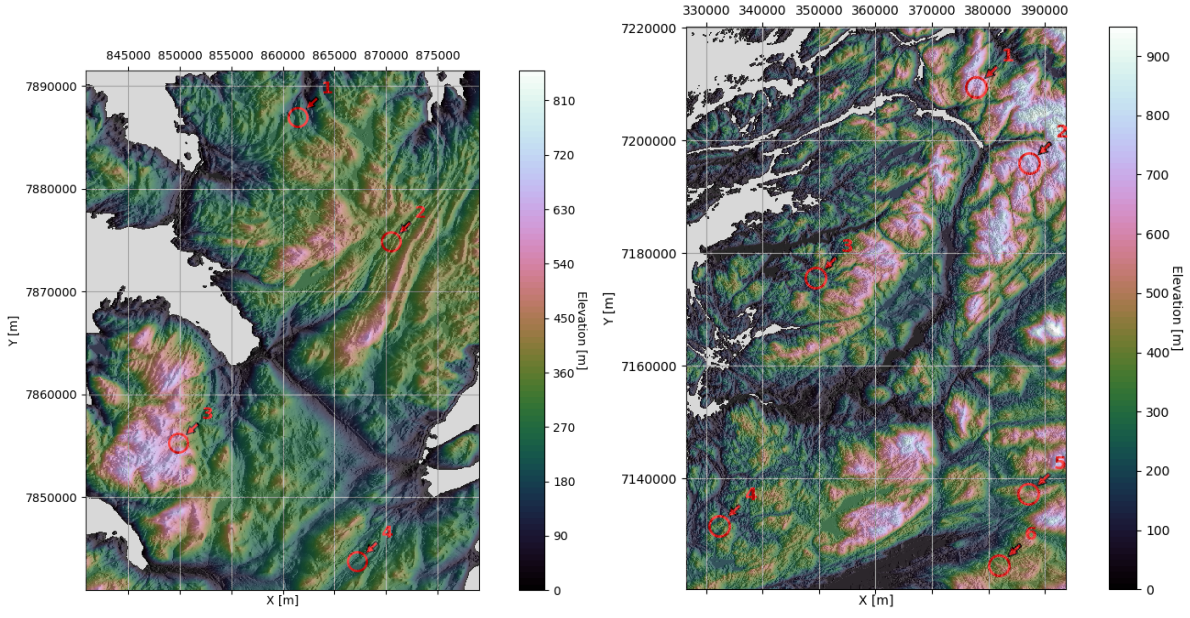

(a) (b)

Figure A.1: Sites-of-interest in (a) area 44 and (b) area 45.

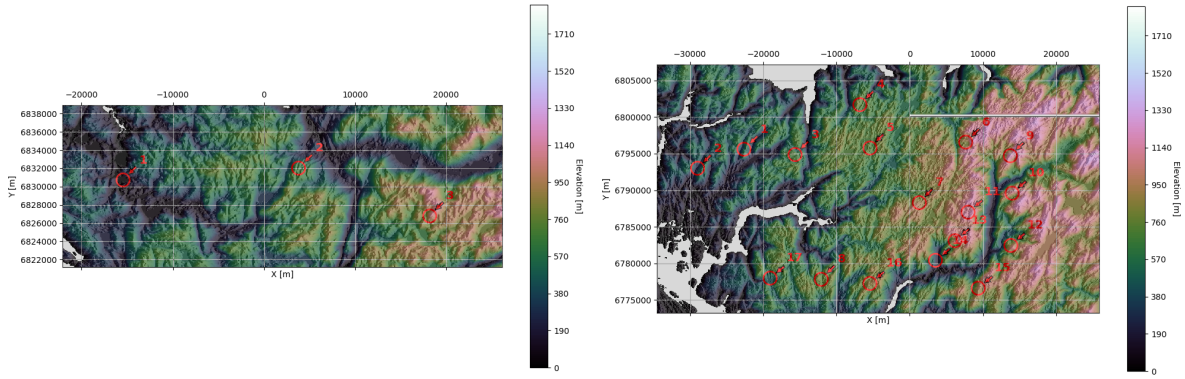

(a) (b)

Figure A.2: Sites-of-interest in (a) area 49 and (b) area 50.

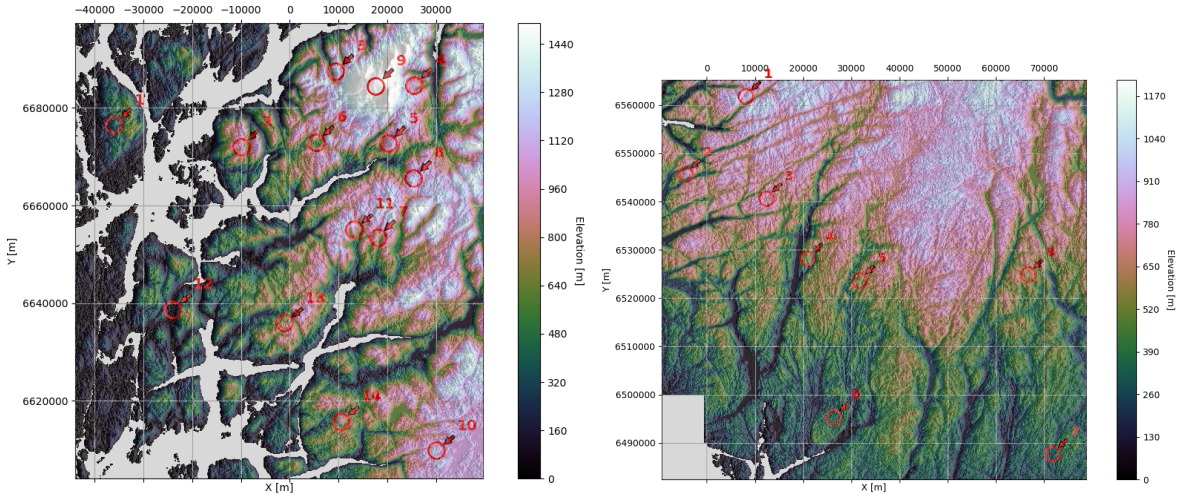

(a) (b)

Figure A.3: Sites-of-interest in (a) area 51 and (b) area 52.

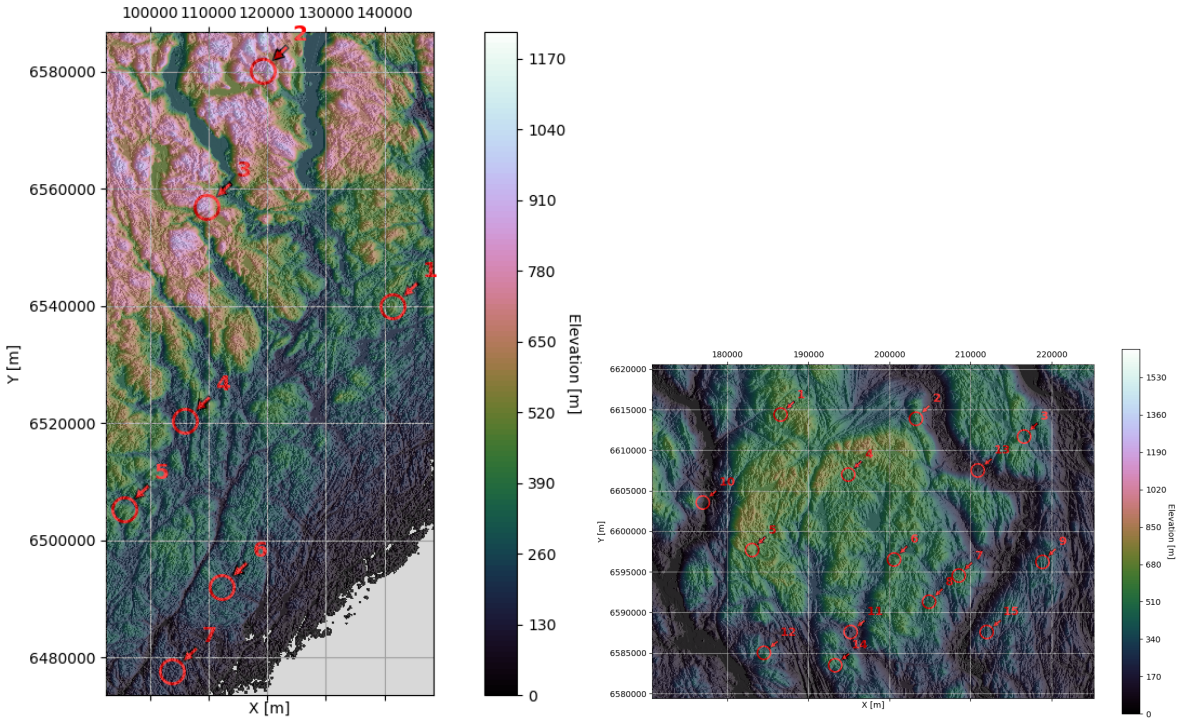

(a) (b)

Figure A.4: Sites-of-interest in (a) area 53 and (b) area 54.

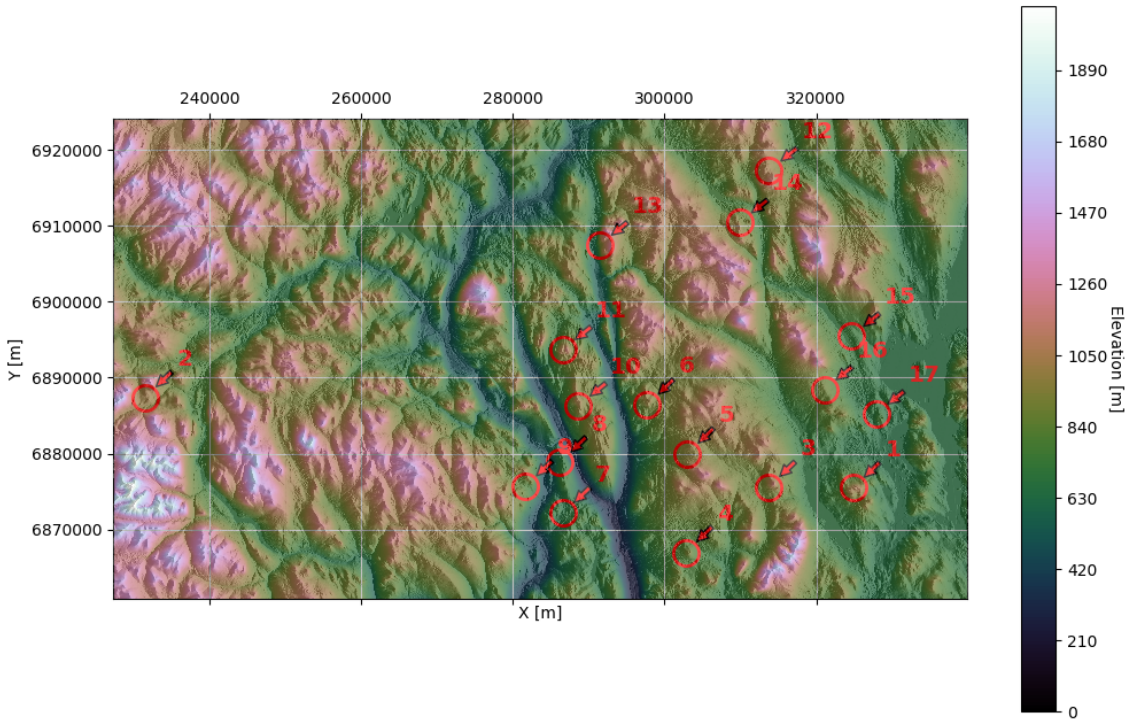

Figure A.5: Sites-of-interest in area 56.

APPENDIX B
Sector-wise Comparison

Below are figures of sector-wise relations of the fractional speed-up ratio ΔS and multiple low-order statistics.

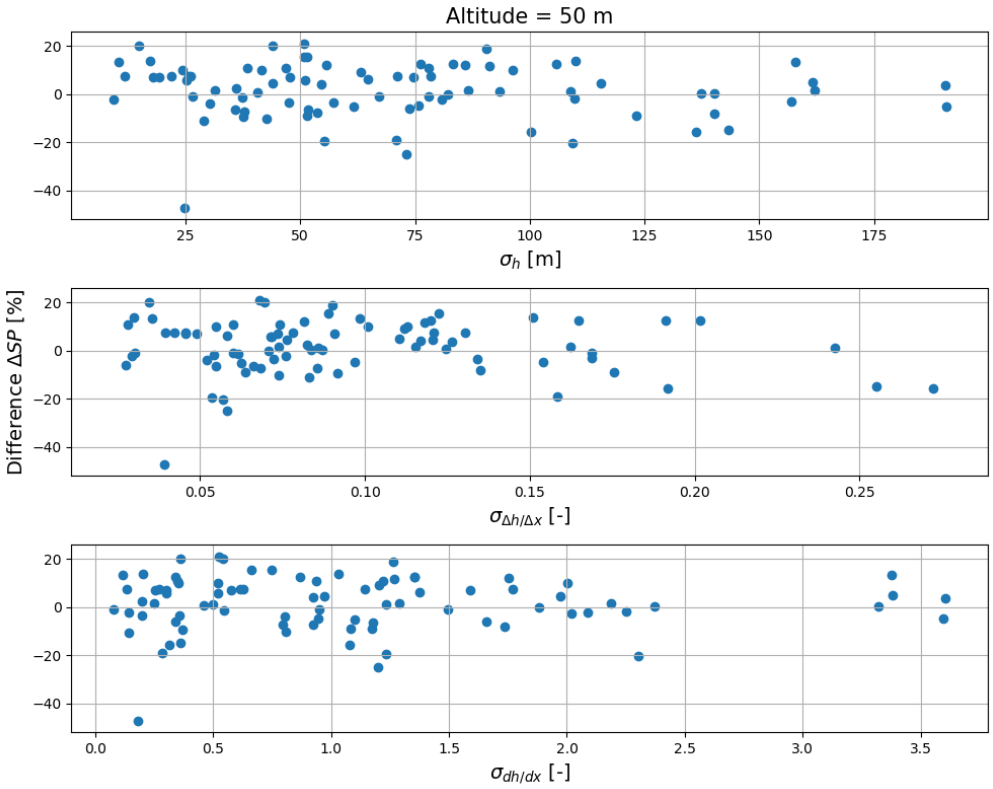

Figure B.1: Difference between the WAsP-IBZ and WAsP-CFD calculated ΔS ('fractional speed-up') values plotted against multiple low-order statistics at an altitude of 50 m. Difference computed as IBZ minus CFD value.

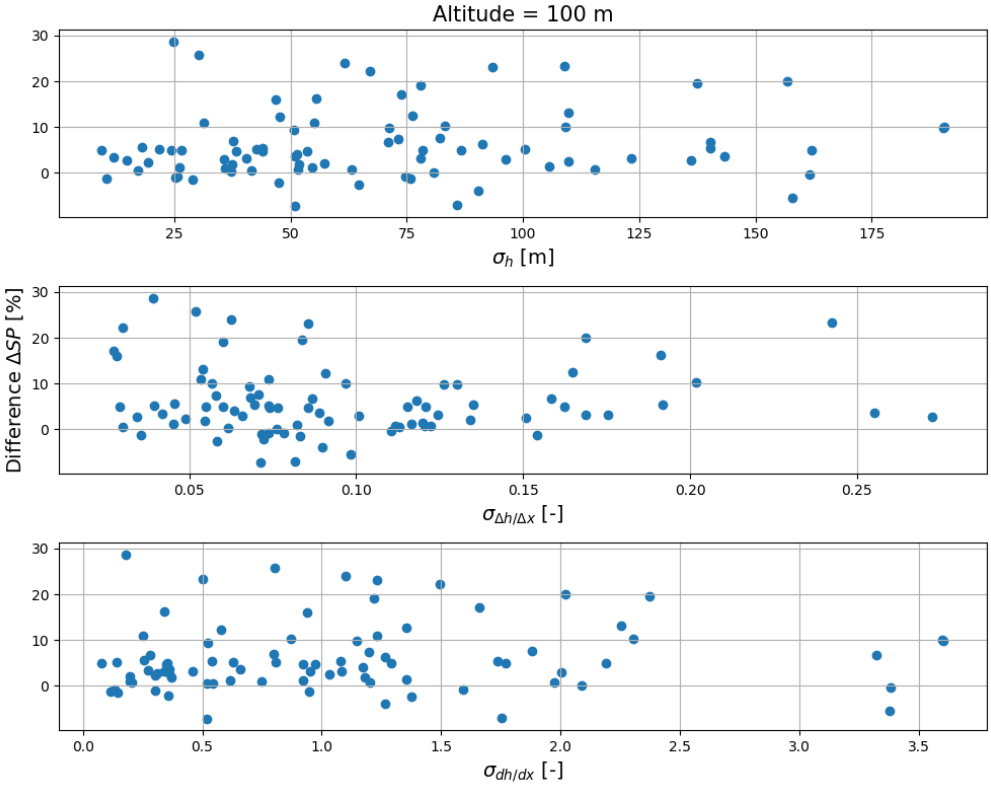

Figure B.2: Difference between the WAsP-IBZ and WAsP-CFD calculated ΔS ('fractional speed-up') values plotted against multiple low-order statistics at an altitude of 100 m. Difference computed as IBZ minus CFD value.

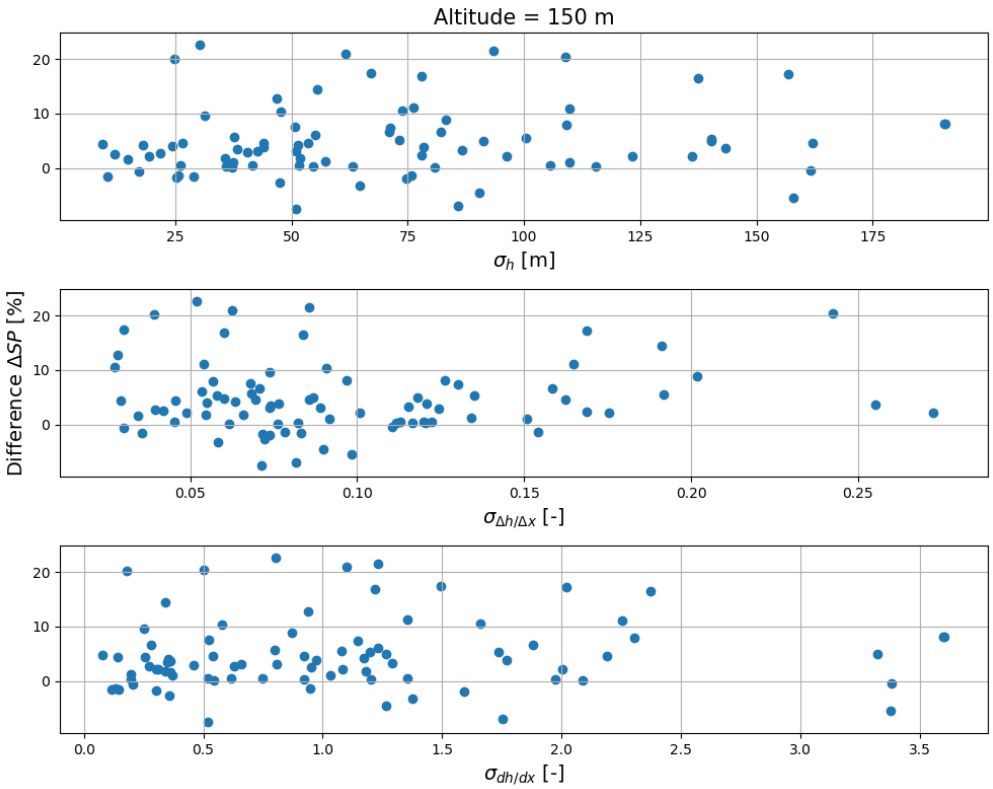

Figure B.3: Difference between the WAsP-IBZ and WAsP-CFD calculated ΔS ('fractional speed-up') values plotted against multiple low-order statistics at an altitude of 150 m. Difference computed as IBZ minus CFD value.

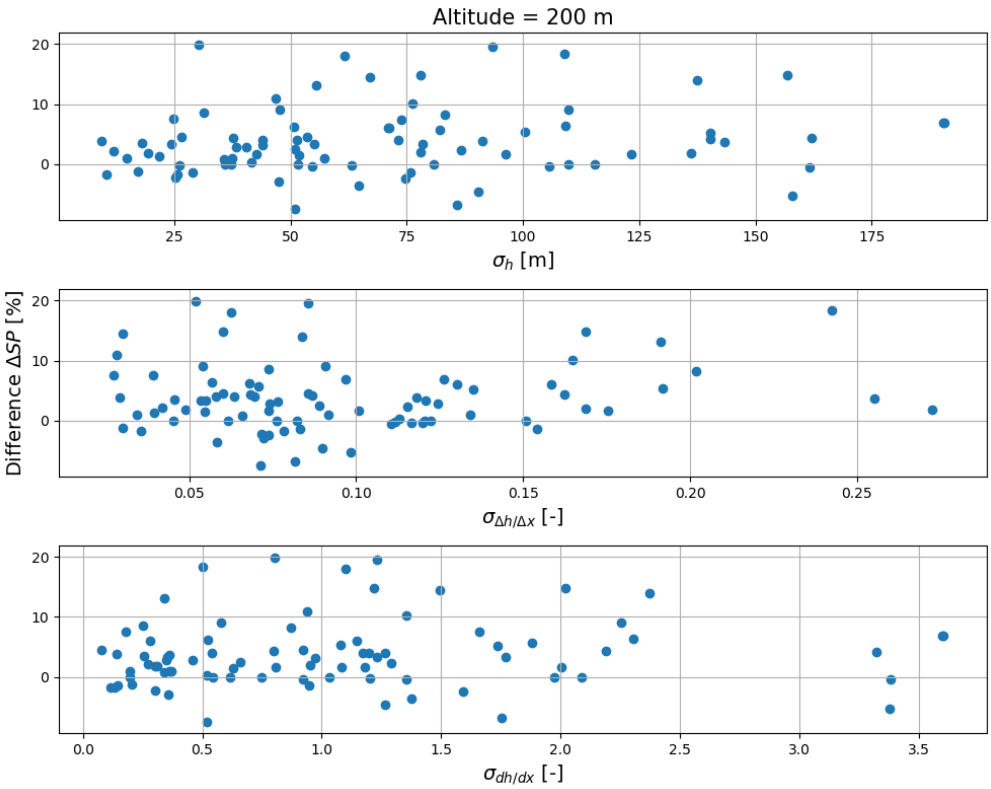

Figure B.4: Difference between the WAsP-IBZ and WAsP-CFD calculated ΔS ('fractional speed-up') values plotted against multiple low-order statistics at an altitude of 200 m. Difference computed as IBZ minus CFD value.

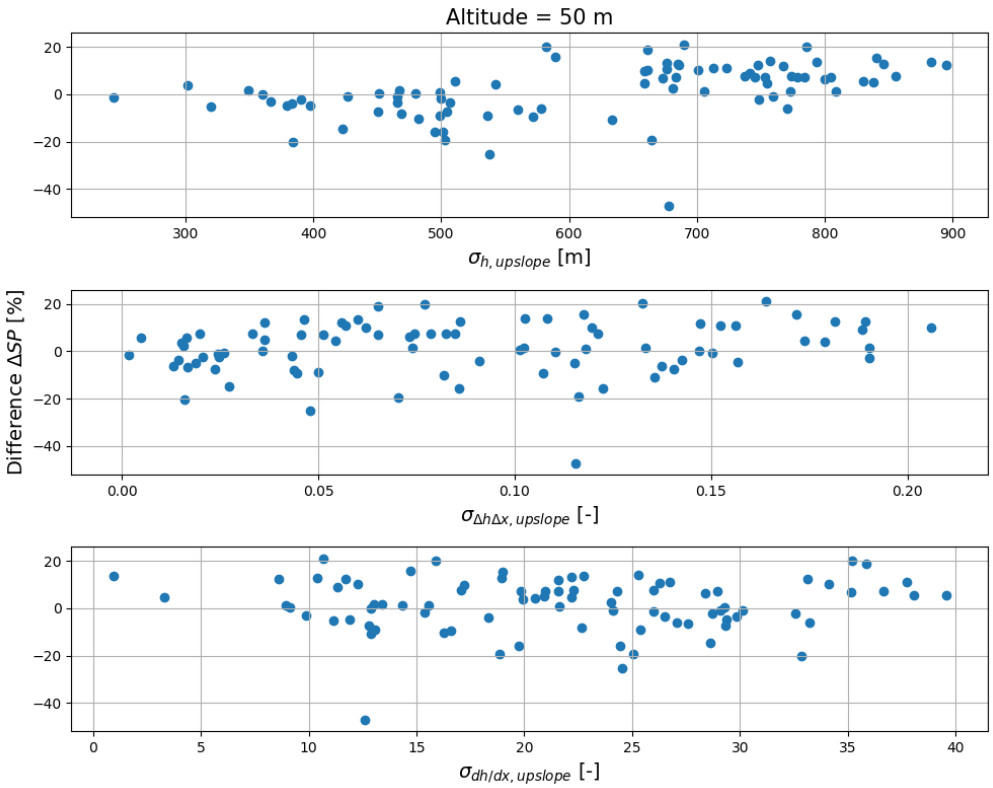

Figure B.5: Difference between the WAsP-IBZ and WAsP-CFD calculated ΔS ('fractional speed-up') values plotted against the upslope only low-order statistics at an altitude of 50 m.

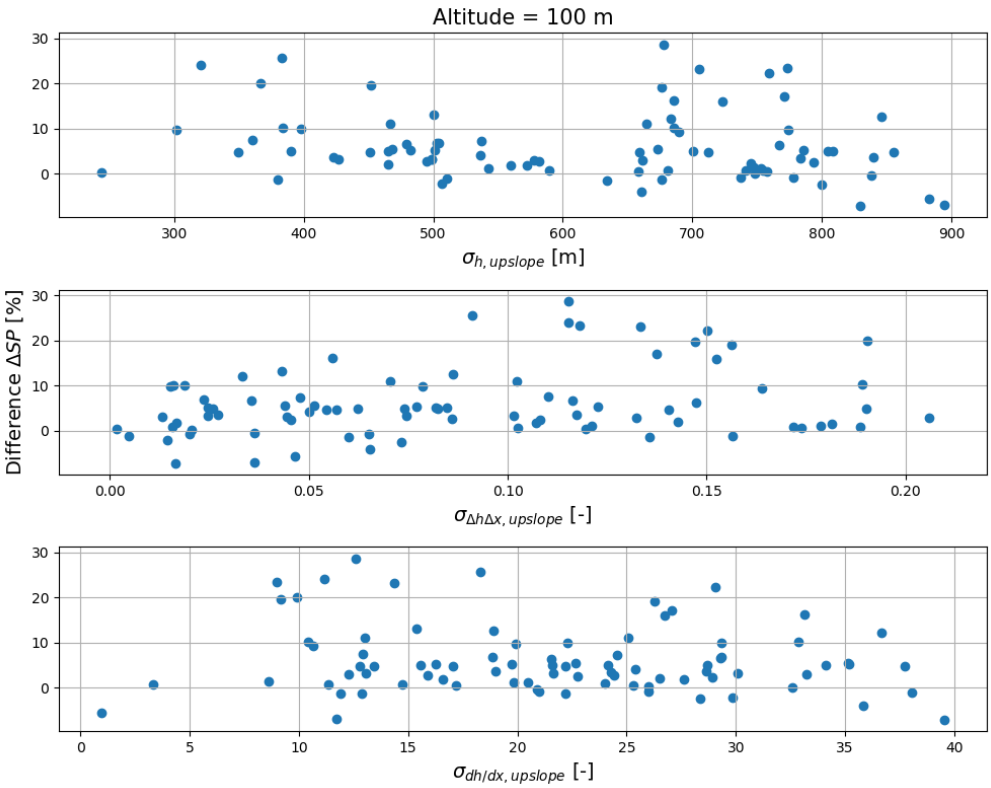

Figure B.6: Difference between the WAsP-IBZ and WAsP-CFD calculated ΔS ('fractional speed-up') values plotted against the upslope only low-order statistics at an altitude of 100 m.

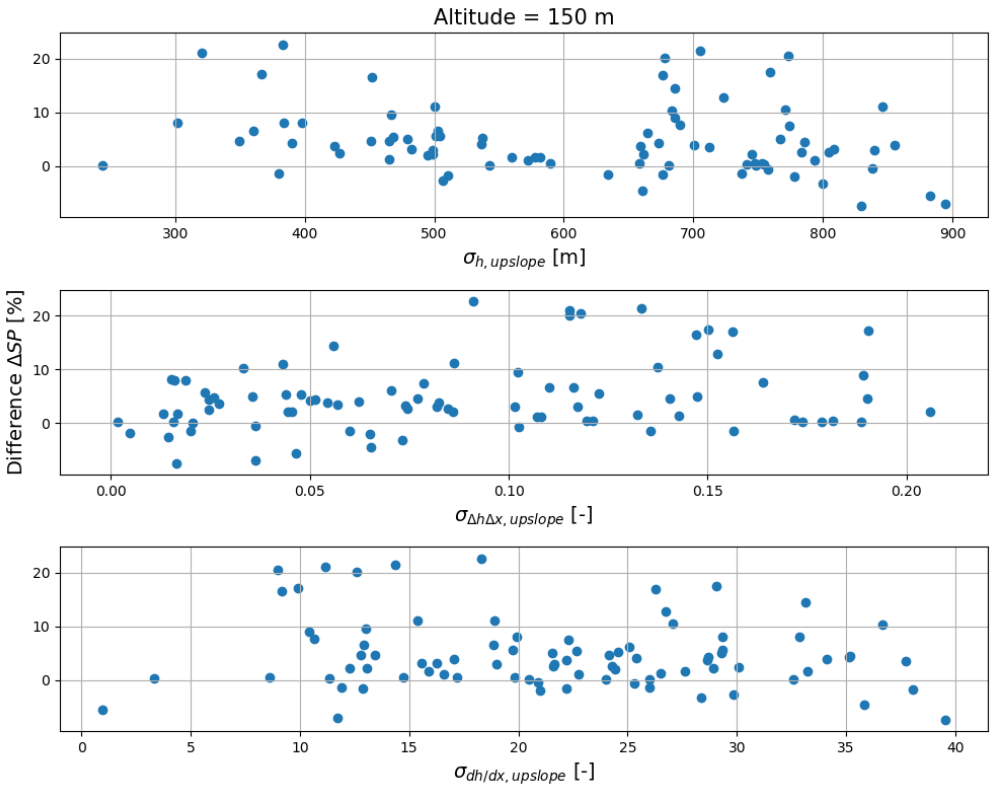

Figure B.7: Difference between the WAsP-IBZ and WAsP-CFD calculated ΔS ('fractional speed-up') values plotted against the upslope only low-order statistics at an altitude of 150 m.

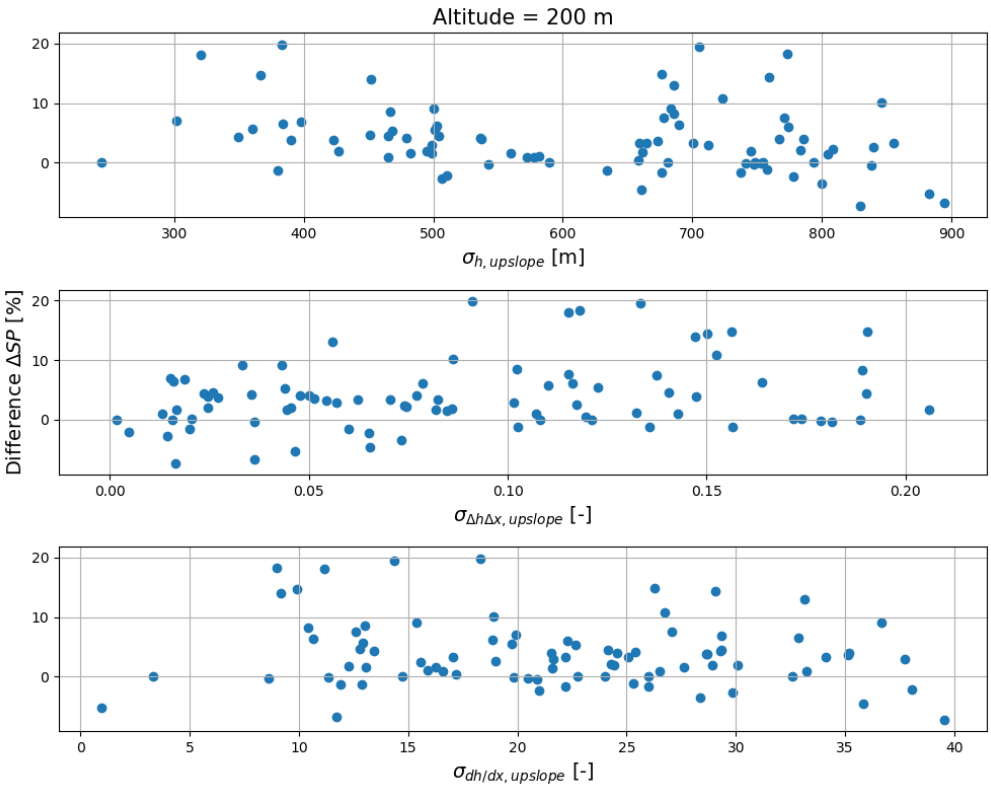

Figure B.8: Difference between the WAsP-IBZ and WAsP-CFD calculated ΔS ('fractional speed-up') values plotted against the upslope only low-order statistics at an altitude of 200 m.

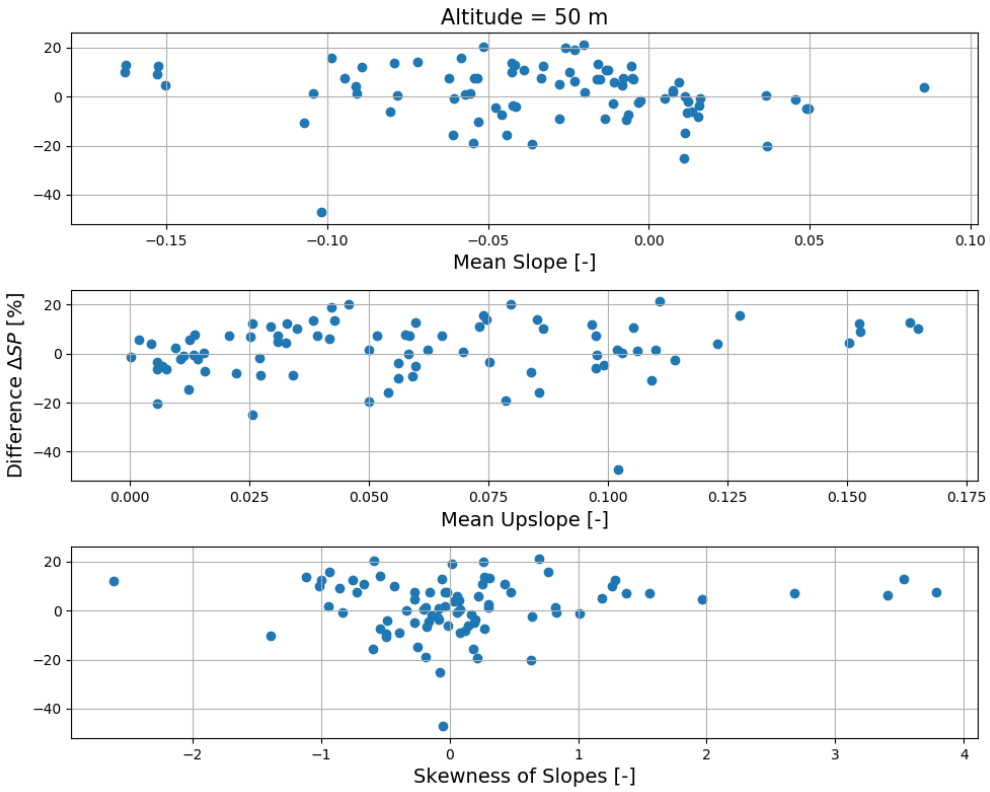

Figure B.9: Difference between the WAsP-IBZ and WAsP-CFD calculated ΔS ('fractional speed-up') values plotted against slope statistics at an altitude of 50 m.

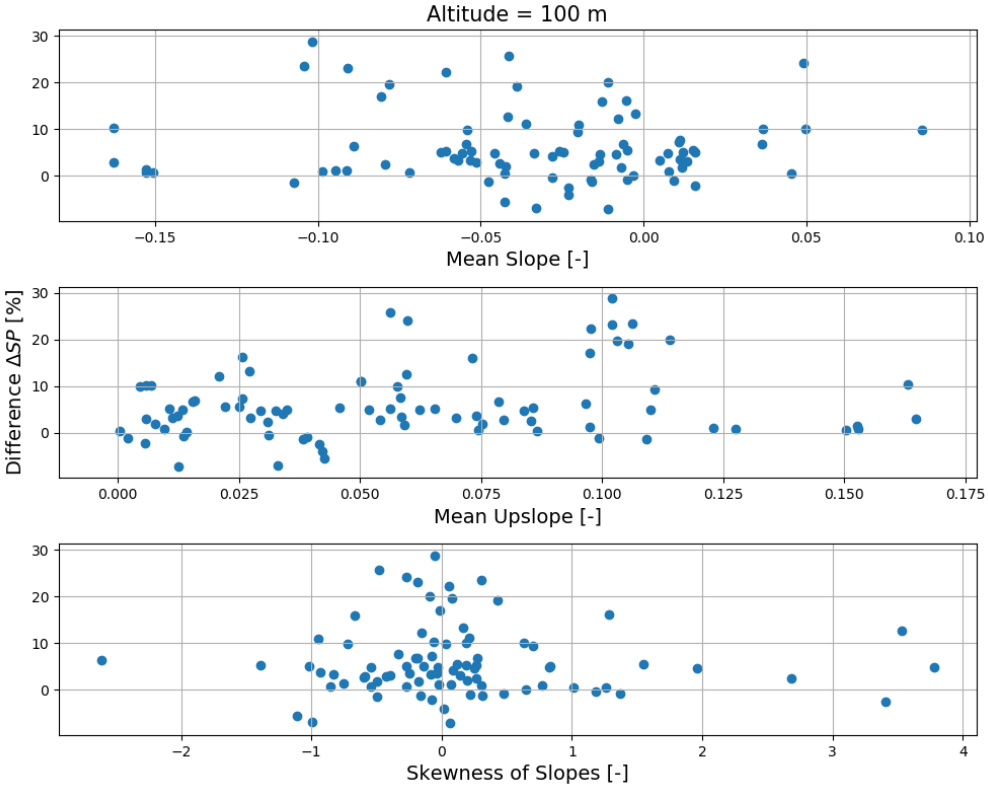

Figure B.10: Difference between the WAsP-IBZ and WAsP-CFD calculated ΔS ('fractional speed-up') values plotted against slope statistics at an altitude of 100 m.

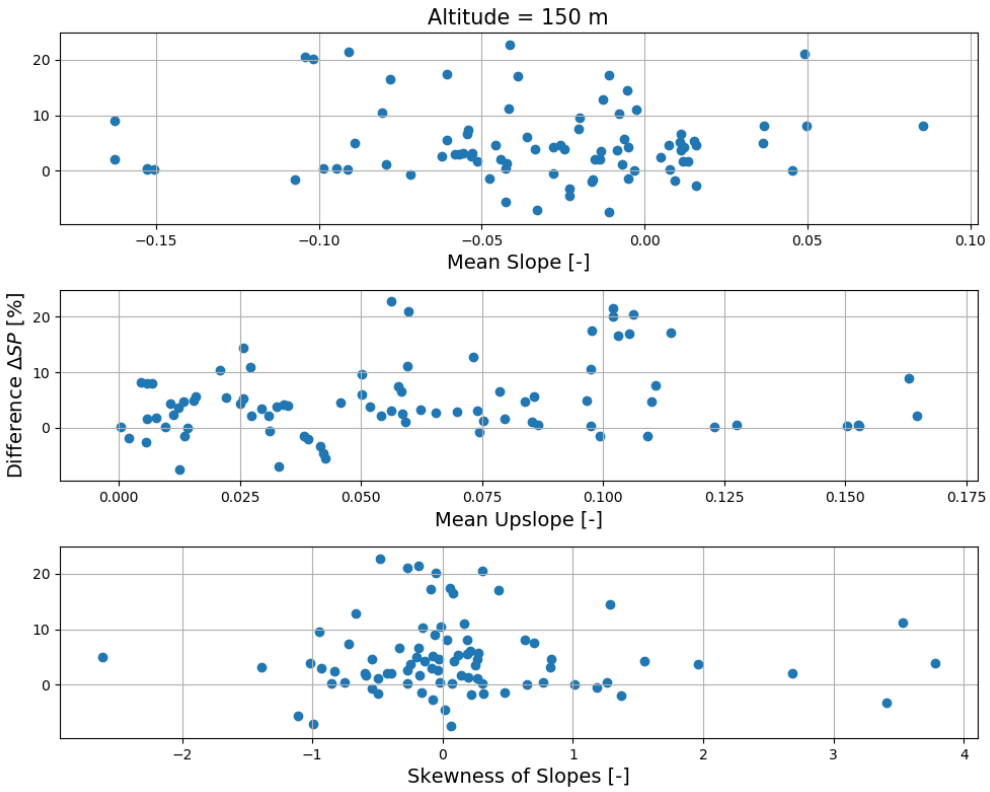

Figure B.11: Difference between the WAsP-IBZ and WAsP-CFD calculated ΔS ('fractional speed-up') values plotted against slope statistics at an altitude of 150 m.

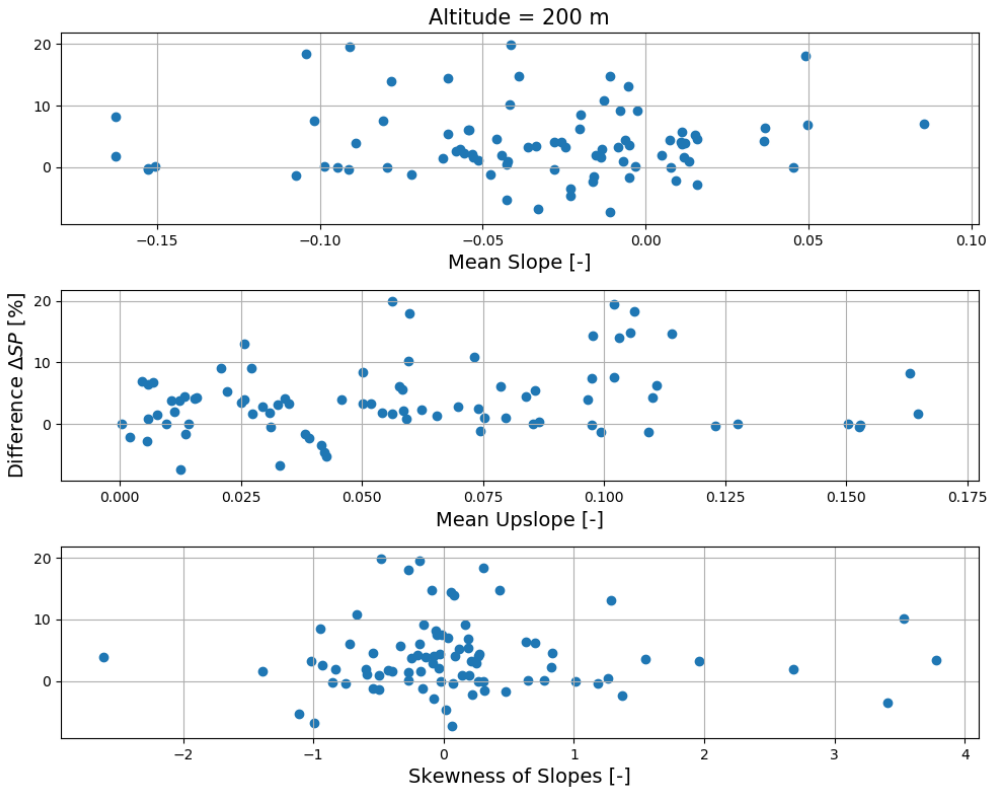

Figure B.12: Difference between the WAsP-IBZ and WAsP-CFD calculated ΔS ('fractional speed-up') values plotted against slope statistics at an altitude of 200 m.

APPENDIX C

Python Code

The following sections contain the main python scripts used for the data acquisition described in Chapter 2.

Main Script

```
# -*- coding: utf-8 -*-
"""
Institution : DTU
Course : Master Thesis Project
Date : 21-Feb-2020
Author : H kon Sletsj e - S183185
Email : hsletsjoe@gmail.com
Description : The main python script used in map creation
and data acquisition.
"""

from pathlib import Path
import h5py
# Self-defined functions
from create_map import create_map
from visualize_map import visualize_map
from get_RIX import get_RIX
from areas_of_interest import areas_of_interest
from puzzle_counter import puzzle_counter
from Spectra import Spectra
#%% Map creation
# What areas do you wanna look at?
area = 'area_56'
# Load data
data_folder = Path('Areas/'+area+'_NordreHedmark/dtm10/data')
# Create dictionary with file names and reference coordinates (top left
    corners)
coord_array, reference, file_dict_tif = puzzle_counter(data_folder)
# Create the combined map
source, extent, resolution = create_map(data_folder,coord_array,
   reference,file_dict_tif)
#%% WHAT DO YOU WANNA DO WITH THIS BEAUTIFUL MAP?
# Do you want to visualize the map?
plot = False
# Do you want to take the spectra?
spectr = True
range_loop = True
# Do you want to get the RIX value?
```

```
rix = True

interest_coord = areas_of_interest(area)
#%% MAP VISUALIZATION
if plot == True:
    # Do you want to annotate it?
    annotate = True
    # Let's make a nice map.
    visualize_map(source,extent,annotate,interest_coord)
#%% LOOP OVER AREAS OF INTEREST
# If so, what finite differencing scheme do you wanna use to get the slopes?
# The following ones are available: 1FD, 1BD, 2CD, 2FD, 2BD
scheme = '1FD'
# Critical slope
critical_slope = 0.3
# Number of radial lines for RIX
N_rix = 72
# Radial length
R_rix = 3500
# Number of radial lines per sector for the spectrum
N_radial = 10
# The radius of the radial lines. In RIX this is 3-4 km.
R_spect = 3500
# Sector width. Set default as 30 degrees as commonly done in wind energy.
phi = 30
# Number of sectors
N_sectors = 12
# RUGGEDNESS INDEX
if rix == True:
    RIX = get_RIX(interest_coord,source,resolution,reference,scheme,N_rix,R_rix,critical_slope)
# SPECTRUM
if spectr == True:
    # [Array, freq/psd, location]
    if range_loop == True:
        for R_spect in range(1000,4100,100):
            PSD_lines, PSD_slopes, sector_signals, sector_slopes, spectrum_line, spectrum_slope = Spectra(interest_coord, source, resolution,reference
                                    ,N_radial,R_spect,phi,N_sectors, scheme)
            with h5py.File('SavedData_raw/'+area+'_'+str(R_spect)+'.hdf5', 'w') as f:
                f.create_dataset('PSD_lines_'+str(R_spect), data=PSD_lines)
                f.create_dataset('PSD_slopes_'+str(R_spect), data=PSD_slopes)
                f.create_dataset(area+'_sector_signals', data=sector_signals)
```

```
78                  f.create_dataset(area+'_sector_slopes', data=
                        sector_slopes)
79      else:
80          PSD_lines, PSD_slopes, sector_signals, sector_slopes,
                spectrum_line, spectrum_slope = Spectra(interest_coord,
                source, resolution,reference
81                                      ,N_radial,R_spect,phi,N_sectors,
                                            scheme)
82  #%% Save Data
83  # Data for data analysis
84  with h5py.File('SavedData_raw/'+area+'_'+str(int(resolution))+'_'+
        scheme+'.hdf5', 'w') as f:
85      f.create_dataset(area+'_extent', data=extent)
86      if spectr == True:
87          f.create_dataset(area+'_spectrum_line', data=spectrum_line)
88          f.create_dataset(area+'_spectrum_slope', data=spectrum_slope)
89          f.create_dataset(area+'_sector_signals', data=sector_signals)
90          f.create_dataset(area+'_sector_slopes', data=sector_slopes)
91          f.create_dataset(area+'_PSD_lines', data=PSD_lines)
92          f.create_dataset(area+'_PSD_slopes', data=PSD_slopes)
93      if rix == True:
94          f.create_dataset(area+'_RIX', data=RIX)
95  #%% Save source map for use in mini maps for WAsP CFD
96  if area == 'area_55':
97      with h5py.File('WAsP_CFD/combined_map_'+area+'.hdf5', 'w') as f:
98          f.create_dataset('combined_map', data=source)
99          f.create_dataset('resolution', data=resolution)
100         f.create_dataset('reference', data=reference[1])
101         f.create_dataset('sites', data=interest_coord)
```

Listing C.1: Main script

Puzzle Counter

```
1   # -*- coding: utf-8 -*-
2   """
3   Institution : DTU
4   Course : Master Thesis Project
5   Date : 21-Feb-2020
6   Author : Hakon Sletsjoe - S183185
7   Email : hsletsjoe@gmail.com
8   Description : Looks through the data folder to count all .tif files
9   and find the true reference piece.
10  """
11  import numpy as np
12  import os
13  # Find the name of all .tfw files
14  def puzzle_counter(data_folder):
15      file_dict = {}
16      for filename in os.listdir(data_folder):
17          if filename.endswith('.tfw'):
```

```
18              tfw_file = open(data_folder/filename, 'r')
19              tfw_raw_data = tfw_file.read()
20              tfw_file.close()
21              file_dict.update({filename: [float(tfw_raw_data.split('\n')
                    [4]),float(tfw_raw_data.split('\n')[5])]})
22      # Loop over file_dict to find the true top left map piece.
23      file_dict_tif = {}
24      for file, coord in file_dict.items():
25          coord_var = np.asarray(coord)
26          # Put coords into columns
27          if 'coord_array' not in locals():
28              coord_array = np.reshape(coord_var, (1,2))
29          else:
30              coord_array = np.append(coord_array,np.reshape(coord_var,
                    (1,2)),axis=0)
31          # Create the reference map piece (top left corner)
32          if 'coord_ref' not in locals():
33              coord_ref = coord_var
34          # Replace .tfw extension with .tif and create new dictionary
35          file_dict_tif.update({file.replace('.tfw','.tif'): coord})
36          if coord_var[0] <= coord_ref[0] and coord_var[1] >= coord_ref
                [1]:
37              coord_ref = coord_var
38              reference = [file.replace('.tfw','.tif') , coord]
39      return coord_array, reference, file_dict_tif
```

Listing C.2: Puzzle Counter

Create Map

```
1  # -*- coding: utf-8 -*-
2  """
3  Institution : DTU
4  Course : Master Thesis Project
5  Date : 24-Feb-2020
6  Author : Hakon Sletsjoe - S183185
7  Email : hsletsjoe@gmail.com
8  Description : This function creates the combined map
9  based on a given data folder.
10 """
11 import rasterio
12 import xarray as xr
13 import numpy as np
14 import os
15 from affine import Affine
16 from rasterio.transform import from_bounds, from_origin
17 from rasterio.warp import reproject, Resampling
18 #%%
19 def create_map(data_folder,coord_array,reference,file_dict_tif):
20     # Preallocate array with correct size
21     lengthX = len(np.unique(coord_array[:,0]))
```

```
22      lengthY = len(np.unique(coord_array[:,1]))
23      # Loop over file_dict_tif and place map pieces
24      i = 0 # Just need a incrementing object
25      for file, coords in file_dict_tif.items():
26          # Load files
27          da = xr.open_rasterio(data_folder/file)
28          raster = rasterio.open(data_folder/file)
29          src_transform = Affine.from_gdal(*da.attrs['transform'])
30          # Calculate map bounds (for visualization)
31          if 'xmin' and 'xmax' and 'ymin' and 'ymax' not in locals():
32              xmin, xmax, ymin, ymax = (0,0,0,0)
33              # Use tfw files to speed this up a bit
34              xmin = coords[0]
35              ymax = coords[0]
36              # Cant help it on these two
37              ymin = int(da.y[-1])
38              xmax = int(da.x[-1])
39          else:
40              if coords[0] < xmin:
41                  xmin = coords[0]
42              if coords[1] > ymax:
43                  ymax = coords[1]
44              if int(da.y[0]) < ymin:
45                  ymin = int(da.y[-1])
46              if int(da.x[-1]) > xmax:
47                  xmax = int(da.x[-1])
48          # Get map attributes
49          resolution = da.res[0]
50          # Set the coordinates as a np.array
51          coord_var = np.asarray(coords, dtype='int32')
52          # Create map array
53          raster_map = raster.read(1)
54          raster_map = raster_map.astype(np.float32)
55          if i == 0:
56              # Pre-allocate memory for the source map.
57              source = np.empty([raster_map.shape[0]*lengthY, raster_map.
                    shape[1]*lengthX], dtype='float32')
58          i += 1
59         # raster_map = raster_map[]
60          raster_map = np.array(raster_map)
61          # Place map pieces.
62          startX = int(np.absolute((reference[1][0] - coord_var[0])/
                resolution))
63          startY = int(np.absolute((reference[1][1] - coord_var[1])/
                resolution))
64          source[startY : startY + raster_map.shape[0],
65                       startX : startX + raster_map.shape[1]] =
                          raster_map
66      source[source==-32767.0] = 0
67      # Put map bounds into extent
68      extent = xmin, xmax, ymin, ymax
69      return source, extent, resolution
```

Listing C.3: Create Map

Visualize Map

```
# -*- coding: utf-8 -*-
"""
Institution : DTU
Course : Master Thesis Project
Date : 24-Feb-2020
Author : Hakon Sletsjoe - S183185
Email : hsletsjoe@gmail.com
Description : Visualizes the map array..
"""
import numpy as np
import matplotlib.pyplot as plt
# Self-made functions
from hillshade import hillshade
#%%
def visualize_map(source,extent,annotate,interest_coord):
    # Set max and min values for the colormap
    #vmean = int(np.mean(source))
    vmin = 0
    vmax = int(np.max(source)) - 200
    # Plot
    fig = plt.figure(figsize=(12, 8))
    ax = fig.add_subplot(111)
    # Hillshader to make the map easier to interpret.
    ax.matshow(hillshade(source,0,10), extent=extent, cmap='Greys',
        alpha=0.3, zorder=10)
    # The colormap.
    cax = ax.contourf(np.flip(source,0), np.arange(vmin, vmax, 10),
        extent=extent,
                      cmap='cubehelix', vmin=vmin, vmax=vmax,zorder=0)
    plt.xlabel('X [m]')
    plt.ylabel('Y [m]')
    plt.grid()
    cbar = fig.colorbar(cax, ax=ax)
    cbar.set_label('Elevation [m]', rotation=270, labelpad = 10)
    #%% Annotate the plot with the points of interest
    if annotate == True:
        circle_rad = 8
        for i in range(len(interest_coord)):
            interest = interest_coord[i]
            ax.plot(interest[0], interest[1], 'o',
                    ms=circle_rad * 2, mec='r', mfc='none', mew=2)
            ax.annotate(str(i+1), xy=interest, xytext=(20,20),
                        textcoords='offset points', color='r', size='x-
                            large',
                        weight='bold', arrowprops=dict(
```

```
43                                      arrowstyle='simple,tail_width=0.2,
                                            head_width=0.5,head_length=0.5',
44                                      facecolor='r', shrinkB=circle_rad *
                                            1.2))
```

Listing C.4: Visualize Map

Get RIX

```
1  # -*- coding: utf-8 -*-
2  """
3  Institution : DTU
4  Course : Master Thesis Project
5  Date : 25-Feb-2020
6  Author : Hakon Sletsjoe - S183185
7  Email : hsletsjoe@gmail.com
8  Description : Calculates the local RIX value based on the areas-of-
       interest.
9  """
10
11 import numpy as np
12 from pol2cart import pol2cart
13 # Self-defined function
14 from FD_scheme import FD_scheme
15 from bilinear_interp import bilinear_interp
16 #%% Obtain line signals
17 def get_RIX(interest_coord,array,resolution,reference,scheme,N_rix=72,R
       =3500,critical_slope=0.3):
18     # Pre-allocate array for RIX.
19     RIX = np.zeros(len(interest_coord))
20     # Set the range of R as an array to look through the matrix using
           polar coordinates
21     # Geometric spacing to emulate what is done in WAsP.
22     R_range = np.geomspace(1, int(R/resolution), int(R/(resolution)),
           endpoint=True, dtype='float64')
23     # Loop over the areas of interest
24     for site in range(len(interest_coord)):
25         area = interest_coord[site]
26         # Calculate location indices in the matrix (X,Y)
27         location_ind = np.around(np.absolute(list((np.array(area) - np.
               array(reference[1]))/resolution)))
28         # Angle within swept sector
29         delta_psi = 360/N_rix
30         # Loop over angles
31         line_signals = np.zeros((int(R/(resolution)),N_rix))
32         for i in range(N_rix):
33             theta = i*delta_psi
34             # Obtain a cartesian line based on the radial line.
35             line_radial = pol2cart(R_range,theta)
36             # Combine the radial line with the location indices.
```

```
37              line_X = np.array(location_ind[0] + line_radial[0], dtype='
                    float32')
38              line_Y = np.array(location_ind[1] + line_radial[1], dtype='
                    float32')
39              # Use indices to get the signal
40              for j in range(len(line_Y)):
41                  line_signals[j,i] = bilinear_interp(line_X[j], line_Y[j
                        ], array)
42          # Calculate the slopes of the radial signals.
43          dX = np.diff(R_range)*resolution
44          slopes = FD_scheme(line_signals,dX,scheme)
45          # Calculate the RIX value
46          rix_radii = np.zeros(N_rix)
47          for column in range(slopes.shape[1]):
48              rix_radii[column] = (np.absolute(slopes[:,column]) >
                    critical_slope).sum()/slopes.shape[0]
49          # As percentage
50          RIX[site] = np.mean(rix_radii)*100
51      return RIX
```

Listing C.5: Get RIX

Finite Difference Schemes

```
1  # -*- coding: utf-8 -*-
2  """
3  Institution : DTU
4  Course : Master Thesis Project
5  Date : 26-Feb-2020
6  Author : Hakon Sletsjoe - S183185
7  Email : hsletsjoe@gmail.com
8  Description : This function calculates the slopes along one
9  direction of an array using a FD scheme of choice.
10 """
11 import numpy as np
12 #%% First-Order Schemes - Only these work right now
13 def FD_scheme(array,dX,scheme):
14     # First-Order Schemes
15     if scheme == '1FD':
16         # Calculate the slopes with first-order forward differencing.
17         slopes = np.zeros((array.shape[0], array.shape[1]))
18         for column in range(array.shape[1]):
19             for row in range(array.shape[0]):
20                 # Use first-order backward differencing for the last
                        point.
21                 if row == array.shape[0]-1:
22                     slopes[row, column] = (array[row, column]
23                     - array[row-1, column])/dX[row-1]
24                 else:
25                     slopes[row, column] = (array[row+1, column] -
26                           array[row, column])/dX[row]
```

```
27      elif scheme == '1BD':
28          # Calculate the slopes with first-order backward differencing.
29          slopes = np.zeros((array.shape[0], array.shape[1]))
30          for column in range(array.shape[1]):
31              for row in range(array.shape[0]):
32                  # Use first-order forward differencing for the first
                        point.
33                  if row == 0:
34                      slopes[row, column] = (array[row+1, column] -
35                            array[row, column])/dX[row]
36                  else:
37                      slopes[row, column] = (array[row, column]
38                      - array[row-1, column])/dX[row-1]
39      #%% Second-Order Schemes - dX not yet fixed for these
40      elif scheme == '2CD':
41          # Calculate the slopes with second-order central differencing.
42          slopes = np.zeros((array.shape[0], array.shape[1]))
43          for column in range(array.shape[1]):
44              for row in range(array.shape[0]):
45                  # Use second-order forward differencing for first point
46                  if row == 0:
47                      slopes[row, column] = (-3*array[row, column] + 4*
                            array[row+1, column]
48                      - array[row+2, column])/(2*dX)
49                  # Use second-order backward differencing for the last
                        point
50                  elif row == array.shape[0]-1:
51                      slopes[row, column] = (array[row-2, column] - 4*
                            array[row-1, column]
52                      + 3*array[row, column])/(2*dX)
53                  else:
54                      slopes[row, column] = (array[row+1, column]
55                      - array[row-1, column])/(2*dX)
56      if scheme == '2FD':
57          # Calculate the slopes with second-order forward differencing.
58          slopes = np.zeros((array.shape[0], array.shape[1]))
59          for column in range(array.shape[1]):
60              for row in range(array.shape[0]):
61                  # Use second-order backward differencing for the last
                        two point.
62                  if row >= array.shape[0]-2:
63                      slopes[row, column] = (array[row-2, column] - 4*
                            array[row-1, column]
64                      + 3*array[row, column])/(2*dX)
65                  else:
66                      slopes[row, column] = (-3*array[row, column] + 4*
                            array[row+1, column]
67                      - array[row+2, column])/(2*dX)
68      if scheme == '2BD':
69          # Calculate the slopes with second-order backward differencing.
70          slopes = np.zeros((array.shape[0], array.shape[1]))
71          for column in range(array.shape[1]):
```

```
72            for row in range(array.shape[0]):
73                # Use second-order forward differencing for the first
                      two point.
74                if row <= 1:
75                    slopes[row, column] = (-3*array[row, column] + 4*
                          array[row+1, column]
76                    - array[row+2, column])/(2*dX)
77                else:
78                    slopes[row, column] = (array[row-2, column] - 4*
                          array[row-1, column]
79                    + 3*array[row, column])/(2*dX)
80    return slopes
```

Listing C.6: FD Schemes

Spectra

```
1  # -*- coding: utf-8 -*-
2  """
3  Institution : DTU
4  Course : Master Thesis Project
5  Date : 9-Mar-2020
6  Author : Hakon Sletsjoe - S183185
7  Email : hsletsjoe@gmail.com
8  Description : The main script to calculate the spectra at the
9  areas-of-interest.
10 """
11 import numpy as np
12 # Self-made functions
13 from get_signal import get_signal
14 from get_spectra import get_spectra
15 from FD_scheme import FD_scheme
16 #%%
17 def Spectra(interest_coord,source,resolution,reference,N_radial,R_spect
       ,
18              phi,N_sectors,scheme):
19     for site in range(len(interest_coord)):
20         area = interest_coord[site]
21         # Obtain the sector wide line signals
22         sector_signal = get_signal(area,source,resolution,reference,
               site,N_radial,R_spect,phi,N_sectors)
23         # Take spectra
24         PSD_line, sector_line_spectra = get_spectra(sector_signal,
               resolution,R_spect,N_sectors)
25         # Pre-allocate the arrays for the spectra
26         if site == 0:
27             spectrum_line = np.zeros((sector_line_spectra.shape[0],
28                                       sector_line_spectra.shape[1],len(
                                             interest_coord)))
29             spectrum_slope = np.zeros_like(spectrum_line)
30             sector_signals = np.zeros((sector_signal.shape[0],
```

```
                                        sector_signal.shape[1],len(
                                            interest_coord)))
            sector_slopes = np.zeros_like(sector_signals)
            PSD_lines = np.zeros((PSD_line.shape[0],
                                  PSD_line.shape[1],len(interest_coord)
                                      ))
            PSD_slopes = np.zeros_like(PSD_lines)
        # Make array of uniform dX values to work with the FD scheme
        dX = np.full(sector_signal.shape[0]-1,resolution)
        # Get sector wide slope signals using a FD scheme.
        sector_slope = FD_scheme(sector_signal,dX,scheme)
        # Take spectra
        PSD_slope, sector_slope_spectra = get_spectra(sector_slope,
            resolution,R_spect,N_sectors)

        # Store in 3D array
        spectrum_line[:,:,site] = sector_line_spectra
        spectrum_slope[:,:,site] = sector_slope_spectra
        sector_signals[:,:,site] = sector_signal
        sector_slopes[:,:,site] = sector_slope
        PSD_lines[:,:,site] = PSD_line
        PSD_slopes[:,:,site] = PSD_slope
    return PSD_lines, PSD_slopes, sector_signals, sector_slopes,
        spectrum_line, spectrum_slope
```

Listing C.7: Spectra

Get Signal

```
# -*- coding: utf-8 -*-
"""
Institution : DTU
Course : Master Thesis Project
Date : 20-Mar-2020
Author : Hakon Sletsjoe - S183185
Email : hsletsjoe@gmail.com
Description : Function to calculate the radial line signals.
"""
import numpy as np

# Self-defined functions
from bilinear_interp import bilinear_interp
from pol2cart import pol2cart
from my_lin import my_lin
#%% Obtain sector wide line signal
def get_signal(location_coord,array,resolution,reference,site,N_radial
    =10,R=3500,phi=30,N_sectors=12):
    # Calculate location indices in the matrix
    location_ind = np.around(np.absolute(list((np.array(location_coord)
        - np.array(reference[1]))/resolution)))
```

```
20      # Set the range of R as an array to look through the matrix using
            polar coordinates
21      #R_range = np.arange(0,R/resolution)
22      # Spacing
23  #    R_range = np.geomspace(1, int(R/resolution), int(R/resolution),
        endpoint=True, dtype='float16')
24  #    R_range = np.array(my_lin(0,int(R/resolution),int(R/resolution)
        ,1.1), dtype='float16')
25      R_range = np.arange(0,int(R/resolution))
26      # Define the sectors
27      sectors = np.arange(-15,345,360/N_sectors)
28      # Angle within swept sector
29      delta_psi = phi/N_radial
30      # Pre-allocate arrays
31      sector_signals = np.zeros((int(R/resolution),N_sectors))
32      line_signals = np.zeros((int(R/resolution),N_radial))
33      # Loop over all sectors (clockwise in Cartesian coordinates)
34      for k in range(N_sectors):
35          sector = sectors[k]
36          # Loop over angles within sector
37          for i in range(N_radial):
38              theta = sector + i*delta_psi
39              # Obtain a cartesian line based on the radial line. [X,Y]
40              line_radial = pol2cart(R_range,theta)
41              # Combine the radial line with the location indices.
42              line_X = np.array(location_ind[0] + line_radial[0], dtype='
                    float32')
43              line_Y = np.array(location_ind[1] + line_radial[1], dtype='
                    float32')
44              for j in range(len(line_Y)):
45                  line_signals[j,i] = bilinear_interp(line_X[j], line_Y[j
                        ], array)
46
47  #            line_X = np.array(np.round(list(map(lambda x : x +
        location_ind[0],line_radial[0]))), dtype='int16')
48  #            line_Y = np.array(np.round(list(map(lambda x : x +
        location_ind[1],line_radial[1]))), dtype='int16')
49              # Use indices to acquire signal
50  #            for j in range(len(line_Y)):
51  #                line_signals[j,i] = array[line_Y[j]][line_X[j]]
52          # Input line signal into the sector array
53          sector_signals[:,k] = np.mean(line_signals,axis=1)
54      return sector_signals
```

Listing C.8: Get Signal

Get Spectra

```
1  # -*- coding: utf-8 -*-
2  """
3  Institution : DTU
```

```
Course : Master Thesis Project
Date : 20-Feb-2020
Author : Hakon Sletsjoe - S183185
Email : hsletsjoe@gmail.com
Description : This function calculates the actual spectra from the
radial signals. Done both using FFT and via Welch's method.
"""
import numpy as np
from scipy.signal import welch
from spectrum import spectrum
#%% Calculate the sector wide spectra with the line_signal input
def get_spectra(sector_signals,resolution,R,N_sectors=12):
    # Intialize array
    sig = np.zeros((len(sector_signals),N_sectors))
    for i in range(N_sectors):
        # Remove the mean from the signal
        sig = sector_signals[:,i] - np.mean(sector_signals[:,i])
        # Take the FFT of the signal
        spec = spectrum(sig,resolution,2)
        # Use Welch method
        fs = 1/resolution
        # Window length
        nw = 1
        nw_l = int(len(sig)/nw)
        freqs, psd = welch(sig, fs, window='boxcar', nperseg=nw_l,
            detrend=False)
#         freqs = freqs*f_N/np.pi
#         psd = psd*np.pi/f_N

        if i == 0:
            spectra = np.zeros((len(freqs),2*N_sectors))
            PSD = np.zeros((len(spec),N_sectors))
        # Store in an array
        PSD[:,i] = spec
        spectra[:,2*i] = freqs
        spectra[:,2*i+1] = psd
    return PSD, spectra
```

Listing C.9: Get Spectra

Spectrum

```
# -*- coding: utf-8 -*-
"""
Institution : DTU
Course : Master Thesis Project
Date : 18-Mar-2020
Author : Hakon Sletsjoe - S183185
Email : hsletsjoe@gmail.com
Description : Function to calculate the PSD of a signal using FFT.
"""
```

```
10 import numpy as np
11 #%%
12 def spectrum(data, resolution, num_of_subseries):
13     # Sample rate
14     fs = 1/resolution
15     N_tot = len(data)
16 
17     # Divide data into subseries
18     K = num_of_subseries
19     N = int(N_tot/K)
20 
21     # Frequencies
22 #     f_min = fs/N            # Lowest calculated frequency
23 #     f_max = fs/2            # Highest calculated frequency -> Nyquist
       frenquency
24 
25     # Pre-allocate array for spectrum
26     Sx = np.zeros(N)
27     Sx = (1/(N_tot*fs))*(np.absolute(np.fft.fft(data)))**2
28 
29     return Sx
```

Listing C.10: Spectrum

Bibliography

Aarseth, I., Nesje, A., & Fredin, O. (2014). West norwegian fjords. UNESCO World Heritage. Guide to geological excursion to Geirangerfjord and ...

Alfieri, J. G., Kustas, W. P., Nieto, H., Prueger, J. H., Hipps, L. E., McKee, L. G., Gao, F., & Los, S. (2019). Influence of wind direction on the surface roughness of vineyards. *Irrigation Science*, *37*(3), 359–373.

Anderson, W., & Meneveau, C. (2011). Dynamic roughness model for large-eddy simulation of turbulent flow over multiscale, fractal-like rough surfaces. *Journal of fluid mechanics*, *679*, 288–314.

Bechmann, A. (2017). Data requirements for wasp, cfd & wrf.

Beljaars, A. C., Brown, A. R., & Wood, N. (2004). A new parametrization of turbulent orographic form drag. *Quarterly Journal of the Royal Meteorological Society*, *130*(599), 1327–1347.

Bowen, A. J., & Mortensen, N. G. (1996). Exploring the limits of wasp the wind atlas analysis and application program, In *1996 european wind energy conference and exhibition*. HS Stephens & Associates.

Bowen, A. J., & Mortensen, N. G. (2004). Wasp prediction errors due to site orography.

Businger, J. A. (1973). Turbulence transfer in the atmospheric surface layer, In *Workshop on micrometeorology*. Amer. Meteor. Soc.

Cavar, D., Réthoré, P.-E., Bechmann, A., Sørensen, N. N., Martinez, B., Zahle, F., Berg, J., & Kelly, M. C. (2016). Comparison of openfoam and ellipsys3d for neutral atmospheric flow over complex terrain. *Wind Energy Science*, *1*, 55–70.

Dapp, W. B., Prodanov, N., & Müser, M. H. (2014). Systematic analysis of persson's contact mechanics theory of randomly rough elastic surfaces. *Journal of Physics: Condensed Matter*, *26*(35), 355002.

Dyer, A. (1974). A review of flux-profile relationships. *Boundary-Layer Meteorology*, *7*(3), 363–372.

Flack, K. A., & Schultz, M. P. (2010). Review of hydraulic roughness scales in the fully rough regime. *Journal of Fluids Engineering*, *132*(4).

Garratt, J. R. (1992). *The atmospheric boundary layer (cambridge atmospheric and space science series)*. Cambridge University Press. http://gen.lib.rus.ec/book/index.php?md5=BCAA6DFF8E91A278265C692F1DECC9E8

Garratt, J. R. (1994). The atmospheric boundary layer. *Earth-Science Reviews*, *37*(1-2), 89–134.

Hicks, B. (1973). Eddy fluxes over a vineyard. *Agricultural Meteorology*, *12*, 203–215.

Holtslag, M., Bierbooms, W., & Van Bussel, G. (2014). Estimating atmospheric stability from observations and correcting wind shear models accordingly, In *Journal of physics: Conference series*. IOP Publishing.

Jacobs, T. D., Junge, T., & Pastewka, L. (2017). Quantitative characterization of surface topography using spectral analysis. *Surface Topography: Metrology and Properties*, *5*(1), 013001.

Jakobsen, S. B., Mindeberg, S. K., Østenby, A. M., Dalen, E. V., Lundsbakken, M., Bjerkestrand, E., Haukeli, I. E., Berg, M., Johansen, F. B., Weir, D., Krogvold, J., Aabøe, A. M., Arnesen, F., Willumsen, V., Butt, B., Bølling, J. K., Solberg, K. G., Ramtvedt, A. N., Aass, H., ... Engebrigtsen, K. H. (2019). Forslag til nasjonal ramme for vindkraft.

Jensen, N. O., Petersen, E. L., & Troen, I. (1984). Extrapolation of mean wind statistics with special regard to wind energy applications. WMO. world climate programme report no. WCP-86.

Kelly, M. (2016). *Uncertainty in vertical extrapolation of wind statistics: Shear-exponent and WAsP/EWA methods* (Report no. E-0121, ISBN 978-87-93278-80-6). Risø Lab/Campus, Roskilde, Denmark, DTU Wind Energy. https://orbit.dtu.dk/en/publications/uncertainty-in-vertical-extrapolation-of-wind-statistics-shear-ex

Kelly, M., Cavar, D., & Sogachev, A. (2019). Complex terrain: From spectra and form drag to effective z_0 in flow simulation, In *19th annual meeting of the EMS*, DTU, Lyngby, Denmark. European Meteorological Society [EMS].

Kelly, M., & Troen, I. (2016). Probabilistic stability and 'tall' wind profiles: Theory and method for use in wind resource assessment. *Wind Energy*, *19*(2), 227–241.

Liu, Z., Hu, Y., & Wang, W. (2019). Large eddy simulations of the flow fields over simplified hills with different roughness conditions, slopes, and hill shapes: A systematical study. *Energies*, *12*(18), 3413.

Lundtang Petersen, E., Mortensen, N., Landberg, L., Højstrup, J., & Frank, H. (1997). *Wind power meteorology*. Risø National Laboratory.

Maurer, K., Bohrer, G., Kenny, W., & Ivanov, V. (2015). Large-eddy simulations of surface roughness parameter sensitivity to canopy-structure characteristics. *Biogeosciences*, *12*(8), 2533–2548.

Mortensen, N. G., Bowen, A. J., & Antoniou, I. (2006). Improving wasp predictions in (too) complex terrain, In *2006 european wind energy conference and exhibition*. European Wind Energy Association (EWEA).

Mortensen, N. G., Petersen, E. L., & Landberg, L. (1993). Wind resources part II: Calculational methods, In *1993 european community wind energy conference*. HS Stephens and Associates.

Mortensen, N. G., Tindal, A., & Landberg, L. (2008). Field validation of the deltarix performance indicator for flow in complex terrain, In *2008 european wind energy conference and exhibition*.

Oberhettinger, F. (2014). *Fourier expansions: A collection of formulas*. Elsevier.

Persson, B. N., Albohr, O., Tartaglino, U., Volokitin, A., & Tosatti, E. (2004). On the nature of surface roughness with application to contact mechanics, sealing, rubber friction and adhesion. *Journal of physics: Condensed matter*, *17*(1), R1.

Pohrt, R., & Popov, V. L. (2012). Normal contact stiffness of elastic solids with fractal rough surfaces. *Physical Review Letters*, *108*(10), 104301.

Raupach, M. R. (1992). Drag and drag partition on rough surfaces. *Boundary-Layer Meteorology*, *60*(4), 375–395.

Raupach, M. R. (1994). Simplified expressions for vegetation roughness length and zero-plane displacement as functions of canopy height and area index. *Boundary-Layer Meteorology*, *71*(1-2), 211–216.

Shaw, R. H., & Pereira, A. (1982). Aerodynamic roughness of a plant canopy: A numerical experiment. *Agricultural Meteorology*, *26*(1), 51–65.

Shuttleworth, W. J. (1991). The modellion concept. *Reviews of Geophysics*, *29*(4), 585–606.

Tennekes, H. (1973). The logarithmic wind profile. *Journal of the Atmospheric Sciences*, *30*(2), 234–238.

Troen, I., Bechmann, A., Kelly, M., Sørensen, N. N., Réthoré, P.-E., Cavar, D., & Jørgensen, H. E. (2014). Complex terrain wind resource estimation with the wind-atlas method: Prediction errors using linearized and nonlinear cfd micro-scale models, In *European wind energy conference & exhibition 2014*. European Wind Energy Association (EWEA).

Troen, I., & Petersen, E. L. (1989). *European wind atlas*. Risø National Laboratory.

Van Loan, C. (1992). *Computational frameworks for the fast fourier transform* (Volume 10). Siam.

Verhoef, A., McNaughton, K., & Jacobs, A. (1997). A parameterization of momentum roughness length and displacement height for a wide range of canopy densities. *Hydrology and Earth System Sciences Discussions*, *1*(1), 81–91.

Walmsley, J. L., Troen, I., Lalas, D. P., & Mason, P. J. (1990). Surface-layer flow in complex terrain: Comparison of models and full-scale observations. *Boundary-Layer Meteorology*, *52*(3), 259–281.

Welch, P. (1967). The use of fast fourier transform for the estimation of power spectra: A method based on time averaging over short, modified periodograms. *IEEE Transactions on audio and electroacoustics*, *15*(2), 70–73.

Wood, N. (1995). The onset of separation in neutral, turbulent flow over hills. *Boundary-Layer Meteorology*, *76*(1-2), 137–164.

Wood, N., & Mason, P. (1993). The pressure force induced by neutral, turbulent flow over hills. *Quarterly Journal of the Royal Meteorological Society*, *119*(514), 1233–1267.

Wyngaard, J. C. (2010). Cambridge University Press. https://app.knovel.com/hotlink/toc/id:kpTA000001/turbulence-in-atmosphere/turbulence-in-atmosphere

Zeng, X., & Wang, A. (2007). Consistent parameterization of roughness length and displacement height for sparse and dense canopies in land models. *Journal of hydrometeorology*, *8*(4), 730–737.

{2.7182818284}ϑωερτυθιοπσδφγηξκλ